SEISMO-MECHANICAL RESERVOIR CHARACTERIZATION FROM FLUID INDUCED SEISMICITY

DISSERTATION

Zur Erlangung des Grades eines

DOKTORS DER NATURWISSENSCHAFTEN

Am Fachbereich Geowissenschaften

der Freien Universität Berlin

vorgelegt von

MSc. Patricia Martínez Garzón

Berlin, May 2014

EHRENWÖRTLICHE ERKLÄRUNG:

Hiermit versichere ich, dass ich die vorliegende Dissertation selbstständig und nur mit den angegebenen Quellen bzw. Hilfsmitteln angefertigt und verfasst habe.

Berlin, den 28.05.2014

Referent:	Prof. Dr. Marco Bohnhoff
Korreferent:	Prof. Dr. Serge Shapiro
Datum der Disputation:	30 June 2014

Freie Universität Berlin

Fachbereich Geowissenschaften

Intitut für Geologische Wissenschaften

Malteserstr. 74 – 100

12249 Berlin

Summary

The importance of fluid-injection experiments has widely increased in the past decades mainly due to their link with energy production activities (e.g. enhanced oil recovery, hydraulic fracturing/wastewater disposal, geothermal energy production and CO_2 storage). These activities are frequently accompanied with the occurrence of induced micro-seismicity. While induced seismicity is mainly perceived as a problem for the public, it can also be used as a useful tool for efficient reservoir development and exploitation. For this reason, both seismological and geomechanical techniques can be combined to achieve a better understanding of the physical processes occurring in geological reservoirs.

In this dissertation, the main aim is to improve the characterization of geo-reservoirs undergoing fluid injection under different scenarios. To do this, the seismic responses to fluid injection from a CO_2 injection project (Penn West Pilot Project, Alberta, Canada) as well as from a geothermal field (The Geysers, California, USA) were analyzed and compared. Particular attention was given to the analysis of the stress field orientation by inverting focal mechanisms of induced seismicity, as well as investigating its relation with fluid injection/extraction processes. Also, a more general seismological and geomechanical (seismo-mechanical) reservoir analysis was performed to efficiently illuminate the processes that led to the occurrence of induced seismicity at The Geysers geothermal field.

First, seismic and leakage signals from a CO_2 injection – Enhanced Oil Recovery project in relation to a reported outflow of CO_2/brine along the monitoring well were investigated. Looking for CO_2 leakage signatures is important to ensure the safe storage of the CO_2 within the target formation. Here, continuous seismic recordings from a borehole array near the reservoir as well as pressure/temperature data were examined. The seismological techniques applied revealed no associated micro-seismicity down to $M_W > -1$, but remarkably elevated noise levels were observed in the seismic recordings framing the outflow time. Additionally, the pressure sensors located in-and above the reservoir reported leakage-related signals indicating the CO_2 movement towards the surface.

In the next step, the use of the stress tensor inversion as a tool for tracing the reservoir processes was explored. The understanding of the stress tensor inversion allowed developing an updated version of the linearized inversion scheme originally created by Hardebeck and Michael, (2006) and Michael, (1987). The software package was successfully designed together with corresponding extensive documentation system and it is now freely available to all users. To test the correct functioning of the software, it was applied to a natural seismicity catalog (North Anatolian Fault Zone), induced seismicity data (The Geysers geothermal field) as well as a synthetic catalog.

Once the software package was ready, the stress field orientation was analyzed in detail at The Geysers geothermal field. There, the reservoir-wide distribution of the stress field orientation with depth was investigated. Normal faulting stress regime was observed at reservoir depth, while strike-slip regime appeared above and below the geothermal reservoir.

Considering the long production history of The Geysers geothermal field, the changes in the stress regime were interpreted as an effect of the horizontal stresses reduction at reservoir depth due to reservoir depletion. Then, a specific cluster of seismicity at the northwestern part of the field was selected to look for potential temporal stress field orientation changes in response to fluid injection. For two injection cycles, the results reported significant changes of the stress field orientation at the time of high injection rates. These changes suggested that the stress field orientation might act as a proxy to detect changes in the in-situ reservoir stresses in response to fluid injection. Initially, the changes in the stress field were attributed either to the reactivation of a different set of fractures, or to the potential temporal opening of new tensile fractures.

Lastly, the previously observed micro-seismicity at The Geysers was extensively analyzed to attain a comprehensive understanding of the characteristics of each injection stage (i.e. before/during/after high injection rates). To obtain a high quality dataset, seismicity relocation was performed and fault plane solutions were re-calculated. Then the temporal evolution of a number of seismological properties over different injection cycles was traced. Many of these properties displayed changes in response to the peak injections and suggested to be originating from the pore fluid pressure increase. It was proposed that the changes displayed in the seismicity properties could be related to the varying influence of two physical mechanisms inducing the seismicity during each injection stage. More specifically, the thermal fracturing of the reservoir may play the most important role regardless of the injection stage, while poroelastic stress changes could be significant at the times of peak-fluid injections. To finalize, a first estimation of the complete stress tensor in this area was provided.

This dissertation contributes to the general understanding of the occurrence of induced seismicity associated to fluid-injection projects. In addition, many of the results obtained during this dissertation constitute a step forward with respect to previous knowledge on the state of stress associated to fluid injection projects.

Zusammenfassung

Die Bedeutung reservoir-geomechanischer Studien im Zusammenhang mit der Auffindung, Exploration und Produktion von Rohstoffen hat in den letzten Jahren stark an Bedeutung gewonnen. Dies betrifft sowohl die begleitende seismologische Überwachung von Fluid-Injektionen in den Untergrund zur Reservoir-Stimulation (Erhöhung der Permeabilität in der Zielformation, Hydraulic Fracturing) als auch die temporäre oder Langzeit-Speicherung von Fluiden oder Gasen im Untergrund (Brauchwasserverpressung, Kohlendioxid-Speicherung). Ziel derartiger Studien sind zumeist entweder die Optimierung von Förderraten (angewandter Aspekt) oder ein verbessertes Verständnis der im Reservoir ablaufenden Prozesse (Grundlagenforschung).

Sowohl bei der Langzeit-Injektion mit geringen Fliessraten als auch bei massiven Kurzzeit-Injektionen unter entsprechend hohen Überdrucken kommt es in vielen Fällen zum Auftreten induzierter Mikroseismizität im Reservoir. Die überwältigende Anzahl der auftretenden seismischen Ereignisse (>95%) sind allerdings meist von so geringer Magnitude, dass sie an der Erdoberfläche weder von Menschen wahrgenommen noch von Seismographen registriert werden. In Ausnahmefällen kann es zum Auftreten spürbarer Seismizität, sogenannter large-magnitude events (LME) kommen. Während induzierte Seismizität von der Bevölkerung meist als Problem angesehen wird, ist sie vor allem aber ein Nutzsignal für Betreiber und Wissenschaft, das die Abbildung der Fluidfront im Untergrund und deren Nachverfolgung durch rein passive Methoden und eine damit verbundene Charakterisierung der Geo-Reservoire erlaubt. Durch eine Kombination von hydraulischen, geomechanischen und seismologischen Daten und Auswerte-Techniken lässt sich dem Ziel der Entschlüsselung von Prozessen im Untergrund damit entscheidend näherkommen.

Im Rahmen dieser Dissertation wurden verschiedene derartige Ansätze eingesetzt und weiterentwickelt und in zwei verschiedenen Feldstudien zum Einsatz gebracht. In der ersten Feldstudie wurden kontinuierliche mikroseismische Registrierungen eines bohrlochgestützten Seismometer-Arrays im Rahmen des CO_2–Speicherprojektes Penn West (Alberta, Canada) ausgewertet. Während keine induzierte Seismizität im Speicherhorizont bis herab zu Magnituden größer als -1 beobachtet wurde, konnten Änderungen im Rauschpegel an den Geophonen in Zusammenhang mit einem an der Oberfläche beobachteten CO_2- und CH_4-Ausfluss (Leckage) gebracht werden. Dem gezielten Einsatz von Bohrlochseismometern kann damit in Ergänzung zur klassischen mikroseismischen Überwachung auch eine Rolle im Zusammenhang mit der Dichtigkeitsüberwachung von Altbohrungen zukommen.

In der zweiten Feldstudie wurden seismische Registrierungen aus dem weltweit größten Geothermiekraftwerk The Geysers (Kalifornien) verschiedenen Auswerteverfahren zugeführt und in Relation zu hydraulischen Reservoirdaten gesetzt. Besondere Aufmerksamkeit wurde dabei der Analyse der Orientierung des krustalen Spannungsfeldes in Reservoir-Tiefe gewidmet, dessen Änderung in direkten Zusammenhang mit den Fliessraten während der Reservoir-Stimulation gebracht werden konnte. Der hier verwendete Standard-Ansatz der Methode der Spannungstensorinversion wurde optimiert, weiterentwickelt und steht nun als frei verfügbarer Algorithmus der wissenschaftlichen Gemeinde zur Verfügung.

Die kontinuierlichen seismischen Registrierungen des lokalen Seismometernetzes in der Region des The Geysers Geothermiefeldes wurden zunächst einer Kreuzkorrekationsanalyse und anschliessenden relativen Relokalisierung zugeführt. Dies resultierte in einer um etwa den Faktor zehn verbesserten Lokalisierungsgenauigkeit und entsprechende detaillierterer Abbildung der Seismizität im Reservoir. Zudem wurden systematische Variationen in der räumlichen Verteilung charakteristischer Herdmechanismen festgestellt. Unter Anderem wurde daraufhin eine vorher nicht bekannte Blattverschiebung im zentralen Teil des Reservoirs postuliert, deren potenzielle Aktivierung durch die nahegelegene Fluidinjektion nun ergründet werden muss.

Die Anwendung der Inversion von Herdflächenlösungen induzierter seismischer Ereignisse zeigt signifikante Änderungen sowohl lokal und in kurzen Zeiträumen in Zusammenhang mit Fluidinjektion im Rahmen eines Enhanced Geothermal Systems im Nordwesten des Geothermiefeldes wie auch Langzeiteffekte durch jahrzehntelange Wärmeproduktion und damit verbundenen reduzierten Horizontalspannungen. Beide Beobachtungen liefern wichtige Aspekte für die geomechanische Antwortfunktion eines geothermischen Reservoirs auf Kurzzeit-Fluidinjektion und Langzeit-Wärmeextraktion.

Die im Rahmen dieser Dissertation vorgelegten Teilstudien zeigen, dass durch den gezielten Einsatz von seismologischen Auswertetechniken im reservoir-geomechanischen Kontext Zusammenhänge erfasst und studiert werden können, die einen Beitrag zum Ziel eines verbesserten Prozessverständnis in Geo-Reservoiren im Zuge von Stimulation, Produktion und Speicherung leisten können.

Contents

1. Introduction 1

1.1 Dissertation motivation and outline 2

1.2 Particular fluid-injection activities 5

1.2.1 Geothermal 5

1.2.2 CO_2 storage 6

1.3 Passive seismic monitoring 7

1.3.1 Detection of micro-seismicity 8

1.3.2 Analysis of micro-seismicity 9

1.4 Reservoir geomechanics 12

1.4.1 Stress field and faulting styles 12

1.4.2 Poroelasticity and the role of the pore pressure 14

1.4.3 Reservoir stress changes associated to pore pressure 16

1.5 Characteristics of fluid-induced seismicity 17

1.6 Description and comparison of case studies 22

2. Microseismic monitoring of CO_2 injection at the Penn West EOR Pilot: Implications for detection of wellbore leakage 24

2.1 Introduction 25

2.2 Input Data 26

2.3. Methods and Results 28

2.3.1. Spectrograms 28

2.3.2. Noise Level Analysis 30

2.3.3. STA/LTA Analysis 31

2.3.4. Analysis of Low-Frequency Signals 36

2.4. Discussion and Conclusions 38

3. MSATSI: A MATLAB© package for stress inversion combining solid classic methodology, a new simplified user-handling and a visualization tool 40

4. Stress tensor changes related to fluid injection at The Geysers Geothermal Field, California 60

4.1 Introduction 61

4.2 Data and Method 62

4.3 Results 64
4.3.1 Depth-dependent stress field changes 64
4.3.2 Time-dependent stress field changes 65
4.4 Discussion and conclusions 66
5. Spatiotemporal changes, faulting regimes and source-parameters of induced seismicity: A case study from The Geysers geothermal field 71
5.1 Introduction 72
5.2 The Geysers geothermal field 75
5.3 Data and methodology used 76
5.4 Results 79
5.5 Discussion 87
5.5.1 Thermoelastic vs poroelastic stress perturbations 87
5.5.2 Hypocenter distribution and faulting mechanism 89
5.5.3 Relative stress magnitude 91
5.5.4 b values and stress drop 91
5.5.5 Stress magnitudes and pore pressure 92
5.5.6 Superimposed effects of thermal fracturing and pore pressure increase 94
5.6 Conclusions 94
6. Synthesis and conclusions 97
6.1 Discussion of results and conclusions 97
6.2 Outlook for future related studies 102
A. High-resolution reservoir characterization using induced seismicity and state of the art waveform processing techniques 104
A.1 Introduction 105
A.2 Methods 106
A.2.1 Double-difference re-location 106
A.2.2 Spectral ratio method 107
A.2.3 Stress inversion 107
A.3 Data 108
A.4 Discussion 111
A.5 Conclusions 113
References 115
Curriculum vitae ..... Error! Bookmark not defined.
List of figures 132

List of tables **134**

Acknowledgments **135**

Chapter 1

Introduction

One of the challenges for the applied scientific community is to provide concepts for enhanced and sustainable use of geo-reservoirs while at the same time mitigating the undesirable environmental and socio-economic impacts. Many of the currently available energy resources involve the exploitation of underground shallow geological reservoirs. Among them, conventional hydrocarbon production has been performed during decades and unconventional production of tight and shale gas involving hydraulic fracturing of the reservoir has become increasingly relevant in recent years. At the same time, the waste-water disposal from the hydraulic fracturing into different formations raised the issue of possible fresh water pollution and increase in seismic hazard. Among the renewable energies, (constituting approximately 15% of the global energy production), the geothermal power production still has a juvenile status but may play a significant role in the future, especially in areas with a thermally hot crust. Finally, numerous geological carbon capture and storage projects have been introduced in recent years with the long-term goal being to reduce CO_2 emissions and greenhouse gas into the atmosphere.

All the mentioned activities involve the temporary or permanent injection of fluid into geological reservoirs at a large or small scale (Fig. 1.1). For example, fluid is commonly injected into oil reservoirs to enhance the production if the field is starting to decline. This practice is known as Enhanced Oil Recovery (EOR). Also, large volumes of fluid are used for hydraulic fracturing and recovery of hydrocarbons in reservoirs where porosity is low to create a new network of fractures. The fluid used for the hydraulic fracturing is then re-injected into waste-water disposal procedures. Finally to maintain the pressure in the system and provide a sustainable geothermal energy resource, it may be necessary to refill or stimulate the reservoir once a considerable volume of steam/hot water has been extracted.

The optimized and safe exploitation of different geological reservoirs requires an early/initial understanding and continuous monitoring of their geomechanical properties. This includes measuring the local minimum principal stress, tracing the temporal changes or spatial distribution of the reservoir in-situ stresses, obtaining information of the reservoir porosity and permeability and carefully controlling the volume of fluid injected as well as the flow rates.

Exploitation of geo-reservoirs involving fluid injection/extraction is tightly linked with the occurrence of micro-seismicity. Since the amount of fluid-injection related projects in the recent years has significantly increased, there has been a corresponding drastic increase in the occurrence of seismicity with magnitudes $M \geq 3$ (Ellsworth, 2013). The occurrence of Large Magnitude Events (LMEs) is crucial for public acceptance and poses a potential threat for local communities, which can eventually result in significant socio-economic impact (e.g. Basel Deep Heat Mining, Oklahoma waste-water disposal) as well as affecting the planned reservoir exploitation. However, the great majority of the induced micro-seismicity (> 95%) has very small magnitudes (not even being detectable at the surface) and they constitute an important tool towards reservoir characterization. Also, micro-seismicity contributes to the

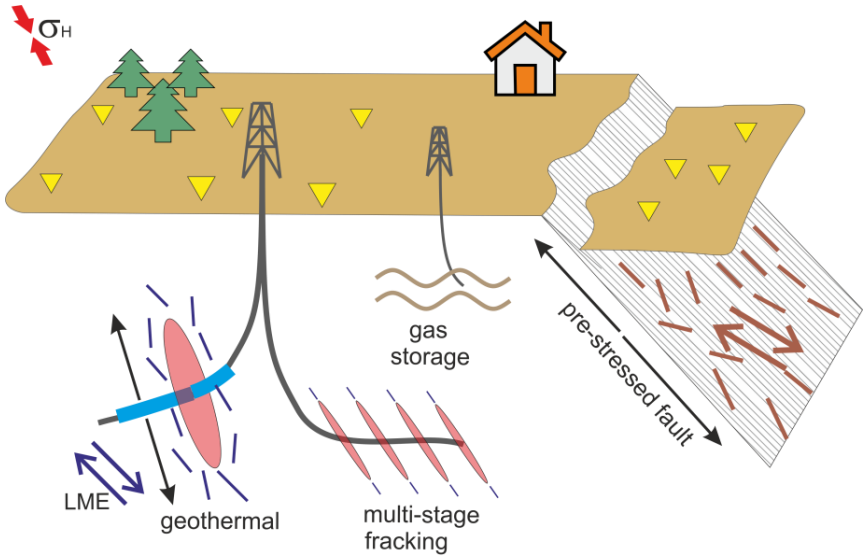

Figure 1.1 Conceptual sketch illustrating different types of fluid-injection activities in the Earth's crust. LME: Large Magnitude Event.

permeability increase of a geo-reservoir (needed for improved fluid flow) and allows tracing the fracture network development and potential fluid paths.

For these reasons, quantitative seismological understanding of the geo-reservoir response and the mechanisms of the induced seismicity together with the reservoir geomechanics ("seismomechanics") is necessary from both scientific and engineering points of view. During the following chapters a number of seismomechanical studies related to the analysis of fluid-induced seismicity into geological reservoirs will be presented.

1.1 Dissertation motivation and outline

The main motivation of this thesis is to contribute towards a better characterization of geo-reservoirs undergoing fluid-induced seismicity by combining the fundamental seismological approaches with geomechanics. Here, special attention is given to the analysis of the stress field. While the variations of the stress field in connection with reservoir production have been largely explored due to its direct application in hydrocarbon industry, the analysis of stress field changes related to fluid-injection operations needs to be further characterized.

Within this dissertation, several key-questions were addressed, the most important ones being the following:

- How is the seismic reservoir response associated to particular sites where fluid injection/extraction is being performed?
- What are the most appropriate seismological techniques to characterize exploitation/stimulation of geo-reservoirs?
- What are the advantages and limitations of the stress tensor inversion applied to reservoir characterization?

- Are there any observable changes in the stress field orientation related to reservoir injection/production at the short and long temporal scales?
- Why the stress field orientation might change in response to injection/extraction processes and what are its implications for safe reservoir exploitation?
- What are the most important physical mechanisms to induce seismicity in geothermal reservoirs?

To address these topics, a number of independent but related studies have been developed during the following chapters. The studies are mostly based on real field data analysis rather than in modelling. Therefore, they have a large experimental component which is based in resolving inverse problems.

As outcome of the research performed during this thesis, two ISI manuscripts have been already published in *Sensors* and *Geophysical Research Letters* (Chapters 2 and 4, respectively), a third manuscript has been accepted for publication in *Seismological Research Letters* (Chapter 3), and a fourth manuscript is ready to be submitted to *Journal of Geophysical Research* (Chapter 5). In addition, a software package related to Chapter 3 with a corresponding extensive documentation is available for all users ready to be downloaded (www.induced.pl/msatsi/). Finally, some results have been also published in a publication in *First Break* (Appendix A). Provided here is a brief summary of the content of each chapter:

Chapter 2

This study investigated the potential occurrence of seismicity and CO_2 leakage associated to the CO_2-EOR performed at the Penn West Pilot Project, Canada. A time period framing two weeks was here analyzed, during which a significant amount of CO_2 migrated to the surface along the monitoring well was here analyzed. The main goal was to detect and locate potential micro-seismicity contained in the continuous geophone recordings as well as to look for any other signals potentially related to the CO_2 leakage. To detect potential seismicity and/or leakage signals, the techniques described in Chapter 1.3.1 were applied. No seismic signals were found during the analyzed period. However, signatures related to the CO_2 leakage along the monitoring well were observed in the average noise level of the geophones.

Chapter 3

The study of the stress field was here initiated for reservoir characterization purposes. After understanding the stress inversion technique, a software package was created to perform stress tensor inversion under MATLAB© environment based on the SATSI algorithm (*Hardebeck and Michael, 2006).* As new features, the overall performance and stability of the inversion method was significantly improved, and a comprehensive error handling and user friendly interface was provided. Additionally, a versatile graphical output which allows visualizing 0 to 3-dimensional stress inversions results was attached offering a variety of plots. The correct performance of the inversion method was tested using input data from various data sets including natural and induced seismicity as well as synthetic data.

Chapter 4

The goal of this study was to investigate potential spatial and temporal variations of the local stress field orientation at The Geysers geothermal field, California. Here, two different stress inversion methods with corresponding detailed uncertainty assessments were tested. Firstly, potential stress field variations with depth all over the geothermal field were investigated. These results reported variations in the orientation of the principal stress axes showing a normal faulting regime at the reservoir depth bounded by a strike-slip regime above and below. Second, one well-constrained cluster of induced seismicity was selected to analyze the temporal evolution of the stress field orientation over a time period of approximately five years. For two different injection cycles, significant changes in the stress field orientation could be observed correlating with the peak-injection periods. Interpretation of these observations was provided in relation with the reservoir geomechanics.

Chapter 5

Given the relevance of the changes found in the stress field orientation during peak-injection periods (Chapter 4), a more complete seismological and geomechanical analysis was performed in order to investigate potential differences in the seismic response of the reservoir during peak-fluid injections. Here, most of the previously described seismological techniques to refine the seismicity catalog were applied (see Chapter 1.3.2), such as double-difference relocation, focal mechanisms calculation, and analysis of spatio-temporal features of the seismicity, but also static stress drop and b-values were estimated. Given that significant differences were found in most of the analyzed parameters, it was here proposed that different physical mechanisms for the induced seismicity might be dominant during the different stages of the injection cycle. Additionally, some constrains to the pore pressure and the local principal stress magnitudes at reservoir depth using available field data were provided.

Chapter 6

A summary of main results obtained within the different studies performed together with a discussion on their potential impact and limitations is here provided.

Appendix A

In this study the application of three different seismological techniques was reviewed in the context of achieving a high-resolution reservoir characterization. Explanations of the relocation of the seismicity, the spectral ratio technique to calculate source parameters and the stress tensor inversion from focal mechanisms were provided to trace the evolution of fluids into the reservoir and improve the estimation of the earthquake damaging potential. These methods were applied to two different geothermal reservoirs. Seismicity relocation and spectral ratio were applied to Berlín geothermal field, El Salvador, while the stress tensor inversion was applied to The Geysers geothermal field, California.

1.2 Particular fluid-injection activities

In the following studies I have focused on the analysis of two particular fluid-injection activities: Geothermal and CO_2 storage. In both of them, fluid is injected into underground geological reservoirs that are expected to have large permeability or to be highly fractured to allow for fluid flow. During or after the injection of fluid into the reservoir, associated induced micro-seismicity might occur. To date, seismicity has been reported more frequently in geothermal reservoirs than in CO_2 storage reservoirs, partially because many geothermal activities involve the stimulation of the reservoir. However, the existing case studies are still not enough to establish clear conclusions on the scenarios than enhance the occurrence of seismicity. Here is provided a description of these two fluid-injection activities as well as an overview of some of the most relevant case studies.

1.2.1 Geothermal

In the simplest case, a geothermal system uses steam to drive turbines and produce electricity. The geothermal power plant preparation process involves the drilling of at least two wells located nearby reaching the target reservoir depth. Through the injection well, the water is injected into the hot reservoir rocks. The water is heated while filling the pore space and it migrates through pre-existing fluid paths until it changes of phase from liquid to vapor. Then, it returns to the surface again through the producer well (Fig. 1.2a). However, not all geothermal reservoirs have sufficient temperature to be able to vaporize the water. In these cases, the injected water is heated inside the geo-reservoir and then returned in fluid state back to the surface, where it is used to heat an artificial liquid with very low boiling point (e.g. Landau geothermal project, Germany). Also, not all geothermal reservoirs are natural. One common practice nowadays is the fracturing or stimulation of deep Hot Dry reservoir Rock (HDR) to enhance the permeability and create new fluid paths between the injection and production wells. This procedure is known as Enhanced Geothermal Systems (EGS) and it is commonly performed in areas with a moderate crustal thermal gradient and low initial permeability (e.g. Soultz-sous-Forêts, France, Alberta Basin, Canada).

Many geothermal sites in the world induce micro-seismicity at major or minor scale, and many studies are available reviewing the development, monitoring and associated seismicity of geothermal projects (e.g. Majer et al., 2007; Evans et al., 2012). Among the best studied fields, The Geysers in Northern California, USA, is the world's largest vapor-dominated reservoir in terms of steam production. The field started to produce in the 1960s and reached its maximum production in 1987. Since 2007, a local dense seismic network is deployed on the field and approximately 4000 events per year (M_W 1 - 4.5) are detected within the reservoir boundaries. Different mechanisms have been proposed for the occurrence of induced seismicity. The most accepted are the thermal fracturing due to local reservoir cooling from the fluid injection and/or poroelastic changes associated to fluid-injection or steam production (e.g. Allis, 1982; Mossop and Segall, 1997; Majer et al., 2007). The source mechanisms, e.g. Double Couple (DC) seismicity vs non-DC, have been also studied, reporting a number of non-DC seismic events (e.g. Ross et al., 1999; Guilhem et al., 2014).Velocity models and V_p/V_s ratios have been also estimated and refined (e.g. Eberhart-Phillips and Oppenheimer, 1984; Gritto and Jarpe, 2014), and peak-ground accelerations and

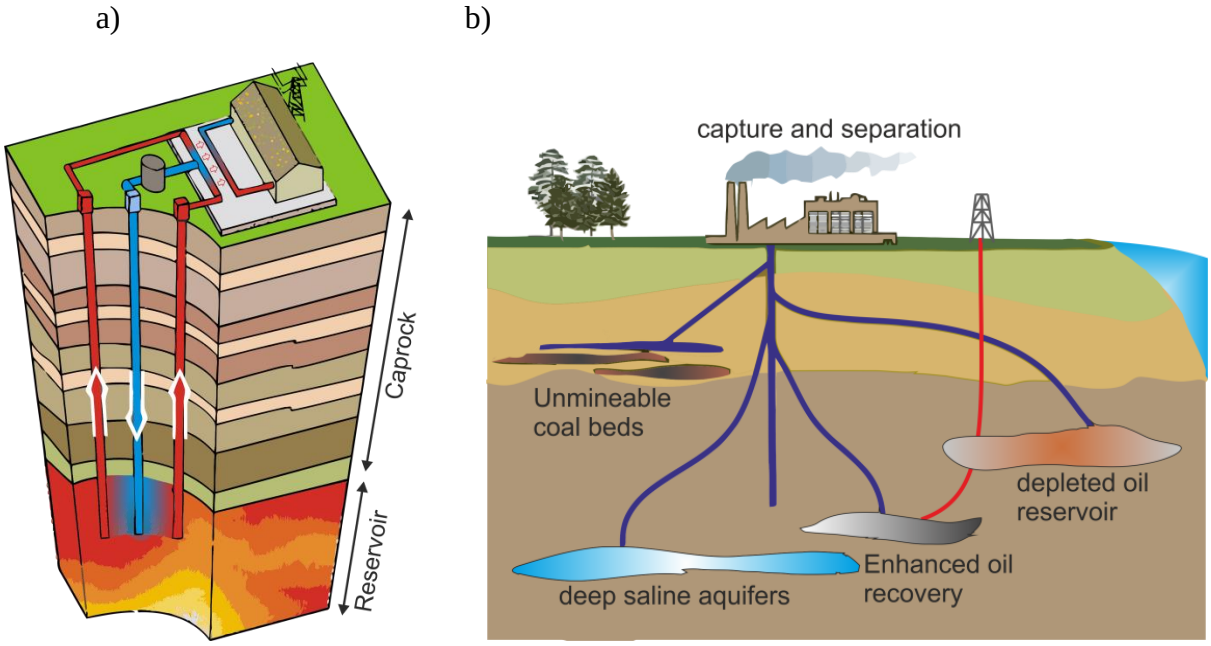

Figure 1.2 a) Conceptual sketch of an EGS: Cool water is injected in the reservoir (blue well). There, it is heated until it becomes steam, and it is returned to the surface through the producer wells (red) (Modified from http://www.mpoweruk.com/geothermal_energy.htm) b) Conceptual sketch of a CO_2 storage site. The supercritical CO_2 is brought to the injector well-heads and injected into the target horizon.

shake-motions scenarios for the LMEs were calculated for the safety of the local communities (Sharma et al., 2013).

In Europe, one of the best studied EGS is the Hot Dry Rock site at Soultz-sous-Forêts, France. Here, the EGS system is organized around three wells drilled into granitic crystalline rock to approximately 5000 m (Caló et al., 2014), reaching 200°C at the bottom. The first successful circulation test was performed in 1997 (Baumgartner et al., 1998). Due to the fracturing of crystalline rock, thousands of seismic events occurred. The largest recorded event with magnitude M 2.9 occurred in 2003 after the shut-in of the injection (Majer et al., 2007). The event had a significant social impact on the local communities resulting in reduction of the injection rate. Currently, no injection is being performed. Among the most relevant studies at this site, Cuenot et al., (2006) calculated systematically the faulting kinematics for hundreds of events, Cornet et al., (2007) determined the complete stress tensor using focal mechanisms and hydraulic fracturing data, and Schoenball et al., (2012) estimated the coseismic static stress transfer caused by the induced events.

1.2.2 CO_2 storage

Capture and storage of CO_2 in geological underground formations has the primary objective of reducing the volume of CO_2 in the atmosphere. The CO_2 is 'captured' and compressed directly at plants with high CO_2 emissions, such as power plants or cement plants. Then, it is transported to the injection site and the CO_2 is injected in supercritical state into a geological formation (mainly depleted hydrocarbon reservoirs, deep saline aquifers or

unmineable coalbeds) where it is intended to be stored for hundreds of years and react with the surrounding reservoir rock (Fig. 1.2b). The target reservoirs are usually composed of sedimentary rocks with high permeability (e.g. sandstone, carbonates). Alternatively, the supercritical CO_2 can be injected underground for EOR purposes at semi-depleted oil fields. In this type of projects, a percentage of the injected supercritical CO_2 is returned to the surface dissolved in the oil.

Verdon et al., (2013) compared the geomechanical deformation and seismic response of three commercial CO_2 storage sites injecting a volume in the order of a Megatonne. The Sleipner Field (North Sea) was the first case in which CO_2 injection was performed successfully into a permeable saline aquifer. The CO_2 movement was traced using time-lapse active seismic methods but no microseismic monitoring was performed. At Weyburn, Saskatchewan (Canada), CO_2 injection was performed for both EOR activities and storage (Verdon et al., 2010). Between 2003 and 2010, approximately 100 seismic events were recorded, noting that the seismic network was not covering the whole reservoir. However at In-Salah (Algeria), where CO_2 injection was performed in fractured sandstone reservoir, approximately 1000 seismic events were detected in a year (Oye, 2012). The different seismic response of these reservoirs was attributed mainly to the elevated pore pressures encountered at In-Salah (~18–30 MPa) (Verdon et al., 2013).

In a pilot CO_2 storage experiment in the Michigan Basin, USA, approximately 10^4 tons of CO_2 were injected into a saline aquifer (Bohnhoff et al., 2010b). Passive seismic monitoring was performed before, during and after the ~17 day injection period. Only one event (M~ -2) was found to be related to the CO_2 injection into the saline aquifer. However, another 94 events occurred in direct vicinity of either of two monitoring wells that penetrated down into a deeper Oil Reservoir (Coral Reef). Since the waveform recordings of these events contained compressional (P) but no shear (S) waves, the authors concluded that the events represented CO_2 leakage from the EOR-CO_2 injection into the Coral Reef, which was going on at the same site for at least 2.5 years (Bohnhoff and Zoback, 2010).

Lastly, a research CO_2 storage Pilot started in 2008 in Ketzin, Germany. There, approximately 67 ktones of CO_2 have been successfully stored. The research at Ketzin has provided a good overview on the processes occurring within the storage reservoir (Martens et al., 2012). This research might be applied to other industrial-scale projects. To date, no seismicity has been detected and no indication for CO_2 leakage has been found (Zimmer et al., 2011).

1.3 Passive seismic monitoring

Passive Seismic Monitoring (PSM) techniques use micro-seismicity to monitor the development of the reservoir stimulation, the fracture network generation and potential fluid paths/leakage (Bohnhoff et al., 2010a). In contrast with the active seismic methods, no artificial sources are necessary. PSM presents significant advantages with respect to active seismic techniques, the most important being related to economic reasons and the time frame that the monitoring is capable of covering. In PSM, the potential micro-seismicity from the reservoir is usually recorded in a number of three component seismic stations installed on the surface or deployed in borehole arrays. By installing the seismometers in boreholes below the surface one can significantly suppress the noise conditions and therefore, increase the observed range of magnitudes.

Goal	Seismological tool	Input data
Detection of seismic signals	Frequency analysis	waveform recordings
	STA/LTA	waveform recordings
	Average noise analysis	waveform recordings
Reservoir characterization	Seismicity location	P and S phase times
	Seismicity re-location	P and S phase times
	Focal mechanism calculation	First motion polarities
	stress inversion	focal mechanism

Table 1.1: Summary of main PSM techniques applied within this dissertation.

The studies presented here involved the application of different seismological approaches. Here, the techniques are divided into detection of potential micro-seismicity and reservoir characterization. A summary of relevant PSM techniques is found in Table 1.1.

1.3.1 Detection of micro-seismicity

Different tools can be applied to systematically detect potential micro-seismic signals contained in continuous seismic recordings from a borehole seismic array (see Chapter 2). The most relevant for the posterior studies are here introduced:

Automatic seismic signal detectors

Basic detectors of seismic signals are usually based on the amplitude of the recordings, but also frequency content can be incorporated if less impulsive onsets are expected (for example when looking for tremors). Among the detection techniques, the Short Time Average / Long Time Average (STA/LTA) is one of the most commonly used. It is based on the ratio between two moving windows of different length. When there is an impulsive signal, the ratio between these two moving windows becomes larger. Alternatively, Akaike Information Criterion or a Hilbert transform methods can be used for the same purpose.

Frequency analysis

Typical micro-seismic signals have higher frequency content than the background noise. Alternatively, low frequency signals may also be contained in the waveform recordings. For example, Long Period-Long Duration (LPLD) events were recently detected in a hydraulic fracturing experiment (Das and Zoback, 2011). These events had large energy content in the frequency band [10 – 80] Hz.

Visual inspection of the frequency content with time can be used to determine the onsets of potential microseismic events. Micro-seismicity will be shown as short time periods (in the order of seconds) during which the frequency content increases significantly. A

frequency analysis can be performed calculating the Fourier transform of the signal for a selected interval of the waveform recording or directly using spectrograms to visually inspect the frequency content of the recordings over time. Once a seismic signal is detected, the calculated spectra can be used to determine various source characteristics such as seismic moment, radiated energy or corner frequency.

Average noise levels

The seismic waveforms have larger amplitudes than the corresponding background noise. For this reason, checking the average noise level of each seismometer and individual components for different moving windows might be relevant to detect periods with larger amplitudes recorded, and therefore, more prone to contain micro-seismicity. For example, during injection periods, the noise recorded in the borehole seismometers close to the injection might be larger due to the fluid migration in the vicinity (e.g. Kwiatek et al., 2010).

1.3.2 Analysis of micro-seismicity

Once the seismic waveforms from the target reservoir have been detected, the next step is to locate the seismicity and create a seismic catalog with earthquake magnitudes and locations (e.g. using hypoinverse or hypoellipse software). For the case studies analyzed here, this step was not necessary and therefore this topic will be not discussed here. Once a seismic catalog is available, the seismological approaches might focus on refining the current seismic parameters. Some of the techniques providing refined seismicity characterization are the followings (see Chapters 4 and 5):

Double-Difference (DD) relocation

The HypoDD relative relocation technique (Waldhauser and Ellsworth, 2000) uses differential travel times of P and S waves to refine the initial earthquake hypocentral location. The differential travel times are calculated for the same station using selected pairs of events forming a cluster. These differential travel times are insensitive to poorly constrained velocity models between cluster's centroid and seismic station. The DD method significantly reduces the relative location uncertainty between the seismic events (Fig. 1.3), but the seismic cluster might be shifted. A more complete description of the method is provided in Appendix A.

Focal mechanism calculation

The focal mechanism calculation is used to determine the orientation of the fault plane and its auxiliary as well as the direction of the fault slip. Typically, the focal mechanism inversion is performed assuming a DC source model. This model implies a pure shear movement occurring on the fault plane. To invert for focal mechanisms, several algorithms have been developed using different input data (e.g. first motion polarities, S/P amplitude ratios or full waveforms). In these studies (Chapter 5), the calculation of focal mechanisms was performed using the FPFIT algorithm (Reasemberg and Oppenheimer, 1985). Here,

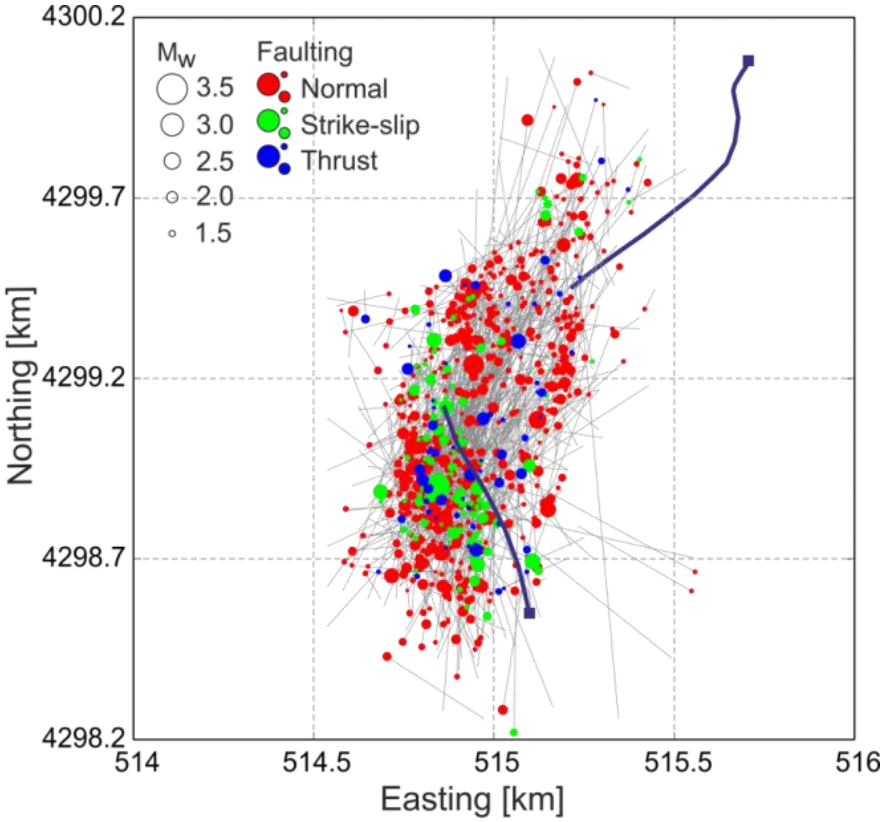

Figure 1.3 Example of relocation of a seismicity cluster. Blue lines: injection wells. Grey lines: trajectory of the seismicity from the original catalog to their relocated position. The relocation allowed visualizing an alignment of the strike-slip mechanisms not seen previously.

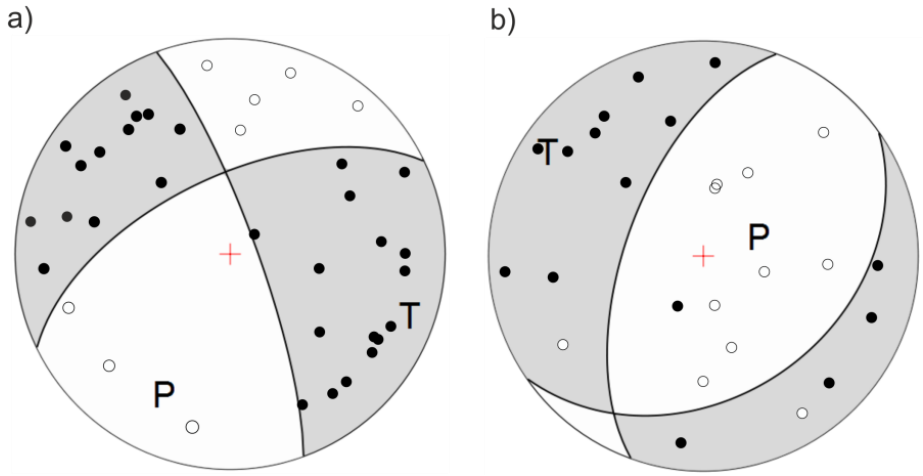

Figure 1.4 Examples of two focal mechanisms calculated using first motion polarities (FPFIT). a) Strike-slip faulting mechanism, there is a perfect fitting with the observation b) Normal faulting mechanism, the best fitting left three polarities wrong.

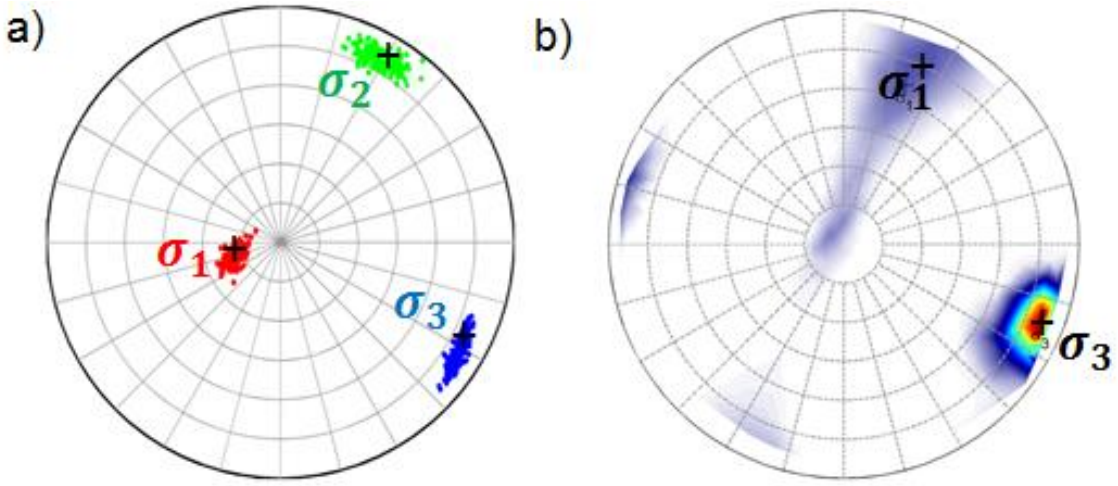

Figure 1.5 Stress inversion results obtained with a) SATSI (Hardebeck and Michael, 2006) showing a normal faulting environment and b) Abers and Gephart, (2001) showing a strike-slip environment. Black cross is the best solution while colored areas represent 95% uncertainty interval.

first motion polarities from stations distributed with reasonable azimuthal and incidence coverage were used to find the fault plane solution that better suit the observations (Fig. 1.4). The best-fitting solution is calculated by two grid search methods composed of a first coarse grid and followed by a finer grid.

Alternatively, the HASH method (Hardebeck and Shearer, 2002) has been tested. This method incorporates a sophisticated uncertainty assessment that takes into account the probability of wrong polarity detection, uncertainties in takeoff angle estimation and poorly known velocity model.

Stress tensor inversion

Estimation of the crustal stress field orientation at depth by inverting focal mechanisms of earthquakes is a well-established seismological technique that can be used over a broad range of scales. The inversion uses mainly focal mechanisms of earthquakes as input data and returns the orientation of the three principal stresses plus a relative stress magnitude (R), which gives a sense of whether the intermediate stress is closer to the most compressive (σ_1) or to the least compressive (σ_3) principal stress. It is defined as:

$$R = \frac{\sigma_1 - \sigma_2}{\sigma_1 - \sigma_3} \qquad [1.1]$$

The stress field orientation is commonly represented using stereographic (equal angle) projection. In the stereonet, the orientation of each of the principal stress axes is determined by two angles: The trend is measured from the top along a circumferential parallel, and it represents the azimuth of the axis from the north. The plunge is measured from the center of the sphere and it represents the verticality of the stress axis, being horizontal at the border of the stereonet and vertical in the center.

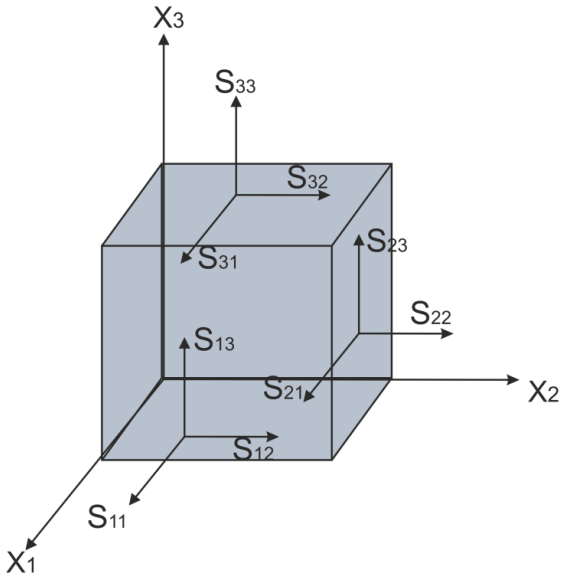

Figure 1.6 Representation of the nine traction vectors acting radially and tangentially in the different planes.

In this dissertation, stress field orientation was determined using different inversion methods (Fig. 1.5). While the SATSI stress inversion method (Hardebeck and Michael, 2006) was mainly used and later improved, a second inversion method using different input data was also tested (Abers and Gephart, 2001). The SATSI software allows for simultaneous stress inversions grouping the seismic events according to different criteria. Therefore, it proves very practical for the purpose of analyzing spatio-temporal changes of the stress field orientation at reservoir scale. The continuous use of SATSI allowed updating the inversion software, which is presented in Chapter 3.

1.4 Reservoir geomechanics

1.4.1 Stress field and faulting styles

Knowledge on the state of stress in the Earth's crust is relevant for both scientific and engineering communities. At the reservoir scale, information on the in-situ stresses is necessary to design the drilling of the well, ensure the caprock integrity and optimize the productivity of the geo-reservoir (Zoback, 2007).

The stress field is defined as a second rank tensor with nine components (Fig. 1.6):

$$S_{ij} = \begin{pmatrix} S_{11} & S_{12} & S_{13} \\ S_{21} & S_{22} & S_{23} \\ S_{31} & S_{32} & S_{33} \end{pmatrix}. \qquad [1.2]$$

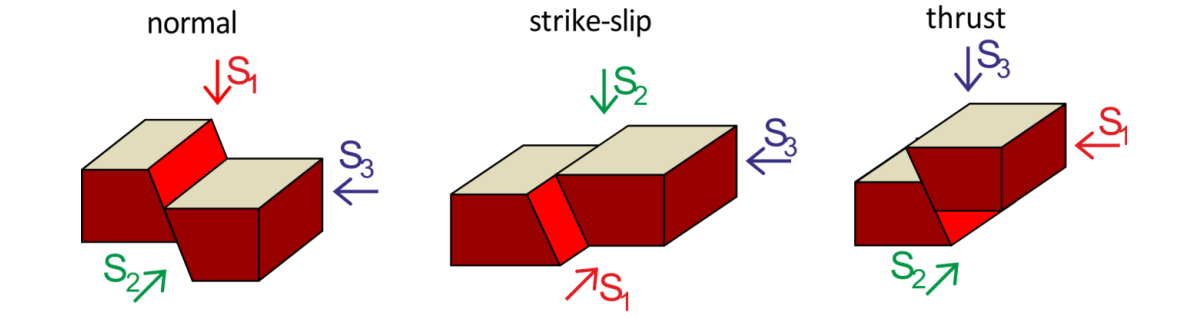

Figure 1.7 Schematic view of the different faulting regimes according to Anderson (1951).

Regime	S_1	S_2	S_3
Normal	S_V	S_{HMax}	$S_{h\min}$
Strike-slip	S_{HMax}	S_V	$S_{h\min}$
Reverse	S_{HMax}	$S_{h\min}$	S_V

Table 1.2 Relative magnitude of principal stresses for each faulting style.

Because of the equilibrium condition, the stress tensor is symmetrical and thus only six components are independent. For any state of stress, a new system of coordinates can be found such that the shear stresses are zero. Therefore the stress tensor can be diagonalized and characterized by the three diagonal components:

$$S_{ij} = \begin{pmatrix} S_1 & 0 & 0 \\ 0 & S_2 & 0 \\ 0 & 0 & S_3 \end{pmatrix}. \qquad [1.3]$$

This new coordinate system is called the principal coordinate system, and the three non-zero elements in the diagonal are the three principal stresses, ordered from most to least compressive. During these studies, compression is considered positive. At the Earth, because of the free surface boundary, the shear traction at the surface is zero. Therefore, for most of the geophysical problems at relatively shallow depth, it can be assumed that one of the three principal stresses is close to vertical, which would correspond to the weight of the overburden above. The mean stress is defined as:

$$M = \frac{(S_1 + S_2 + S_3)}{3} \qquad [1.4]$$

The deviatoric stress tensor is defined by subtracting the mean stress from the trace of the stress tensor (Eq. 1.2):

$$D = \begin{pmatrix} S_{11} - M & S_{12} & S_{13} \\ S_{21} & S_{22} - M & S_{23} \\ S_{31} & S_{32} & S_{33} - M \end{pmatrix} \quad [1.5]$$

Given that the three elements of the trace are modified in the same way, the deviatoric stress tensor has the same eigenvectors as the general stress tensor (Eq. 1.2).

According to Anderson, (1951), faulting regimes are defined by the relative magnitude of the three principal stresses. This way, normal faulting is obtained when the S_1 axis is vertical, strike-slip faulting is obtained when the S_2 axis is vertical, and reverse faulting is obtained when the S_3 axis is the vertical (Fig. 1.7). A description of the relative orientations of the stresses in each faulting style is summarized in Table 1.2.

The orientation of the three principal stresses can be estimated from a number of techniques. Looking at borehole breakouts and/or stress-induced tensile well fractures one can learn about the orientation of the maximum and minimum horizontal stresses, respectively. Also, indirect information on the stress field orientation can be obtained by formally inverting earthquake focal mechanisms. However, estimation on the complete stress state (i.e. the principal stress magnitudes) remains a challenging task given the difficulty of obtaining direct stress measurements at depth. For reservoir-scale problems, one of the most reliable ways to estimate the minimum principal stress would be to perform a leak-off test. Alternatively, borehole breakouts could also provide some constrains on the horizontal stress magnitudes.

In principle, the stress field in the crust at different depths can be considered generally homogeneous, according to data reported from focal mechanisms of earthquakes (Zoback, 1992). However, there might be some effects at the local scale, for example salt domes or fluid injection/extraction activities that might locally redistribute the stress magnitudes (Zoback, 2007).

1.4.2 Poroelasticity and the role of the pore pressure

The pore pressure is defined as the pressure of the fluid filling the pores of a rock volume. According to Terzaghi, (1923), the effective stresses in the crust are defined as:

$$\sigma_{ij} = S_{ij} - \delta_{ij} p \,, \quad [1.6]$$

where σ_{ij} is the effective stress tensor, S_{ij} is the stress tensor, δ_{ij} is the Kronecker's delta and p is the pore pressure. According to this, the pore pressure only affects the normal stresses. For poroelastic deformation, this definition was updated by Nur and Byerlee, (1971) to:

$$\sigma_{ij} = S_{ij} - \alpha \delta_{ij} p \,, \quad [1.7]$$

where α is the Biot coefficient and it varies from 0 for nearly solid rock (e.g. quartzite) to 1 in very porous rocks or uncemented sands (Zoback, 2007). At reservoir scale, where rocks are usually porous, the Biot coefficient is close to 1.

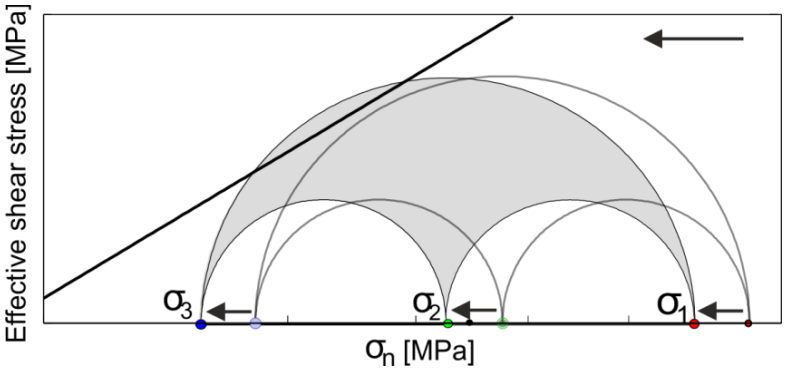

Figure 1.8 Representation in the Mohr circle of the pore pressure increase assuming a Mohr-Coulomb failure criterion. The initial state of stress is plotted with gray lines.

Assuming a Mohr-Coulomb failure condition, the shear strength of a rock is defined as:

$$\tau = H + \mu(\sigma_n) = H + \mu(S_n - p)\,, \qquad [1.8]$$

where τ is the shear strength, H is the cohesion strength of the rock, μ is the coefficient of friction, σ_n is the effective normal stress, S_n is the normal stress and p is the pore fluid pressure. Therefore, increasing the pore pressure reduces the effective normal stresses, reducing the shear stress required for rock failure, and generally brings the rock closer to failure (Fig. 1.8). Note that, since the three principal stresses are shifted by the same amount, the orientation of the principal stresses should not be affected.

The pore pressure plays a very important role for processes occurring at both global and reservoir scale. High pore pressures indicating the presence of fluids in the crust might enhance the failure of adjacent faults (Hardebeck and Hauksson, 1999). In the same way, low pore pressures interpreted from V_P/V_S ratios have been correlated with the locked parts of a subduction interface (Moreno et al., 2014). At reservoir scale, pore pressure monitoring plays a fundamental role given its effect on the effective stresses. For drilling activities, the mud weight should be kept higher that the reservoir pore pressure (to avoid flow out of the well) but lower than the minimum principle effective stress (σ_3, to not fracture the reservoir).

To estimate the value of the pore pressure at the injection interval, one could measure the pressure at the bottom of the well and use it as an approximation. When bottom-hole pressure is not available, some studies have approximated the pore pressure around the injection interval to the well-head pressure plus the hydrostatic pressure (e.g. Baisch and Harjes, 2003). However, pore pressure estimation from real data even at reservoir scale is a challenge, partially due to its high spatial and temporal variability. To describe the spatial pore pressure distribution, theoretical models should be applied, as the pore pressure relaxation front (Shapiro et al., 2003), which has also been recently upgraded for non-linear fluid-rock interaction (Hummel and Shapiro, 2012).

1.4.3 Reservoir stress changes associated to pore pressure

Apart from Terzaghi's Law (Eq. 1.6), changes of reservoir pore pressure due to production and/or injection activities also affect the stress magnitudes. As a result of the in-situ stress changes, the seismicity in pre-existing cracks and local faults might increase. The effect of the pore pressure on the stress magnitudes has been particularly studied for the case of reservoir depletion due to hydrocarbon extraction.

To characterize the state of stress in a reservoir, it is frequently assumed a case of uniaxial strain (Jaeger and Cook, 1971). This means that no deformation occurs in the horizontal reservoir plane:

$$\varepsilon_V \neq 0, \varepsilon_H = \varepsilon_h = 0. \qquad [1.9]$$

Therefore for the horizontal deformation to be null, there must be a variation in the horizontal stresses. An application of this case is the reservoir depletion, where the reservoir decreases its volume due to the long-term production activities. As associated effects, the horizontal stresses at reservoir depth should decrease and vertical subsidence commonly occurs (Fig. 1.9).

From the study of regional fractures, a relation between the stresses and the pore pressure was derived assuming a laterally extensive reservoir (Lorenz et al., 1991):

$$S_{H,h} = \left(\frac{\nu}{1-\nu}\right)\left(S_V\right) + \alpha p\left(1-\frac{\nu}{1-\nu}\right) \qquad [1.10]$$

Where $S_{H,h}$ are the maximum and minimum horizontal stresses, respectively, ν is the Poisson's ratio and S_V is the vertical stress.

By assuming constant vertical stress and taking the derivative with respect to the pore pressure, the following is obtained:

$$\Delta S_{H,h} = \alpha \frac{1-2\nu}{1-\nu} \Delta p \qquad [1.11]$$

This equation shows that for laterally extensive reservoirs, changes in the pore pressure lead to a proportional change in the magnitude of the horizontal stresses at reservoir depth (Fig. 1.9). The validity of this expression has been verified in some reservoirs subjected to depletion such as the Ekofisk Field (Teufel and Rhett, 1991).

The variation of the stresses induced by pore pressure changes has been modelled for different types of reservoir geometries. Among the performed approaches, Segall and Fitzgerald, (1998) used a disk shape reservoir and concluded that in geothermal reservoirs the thermal stresses dominate over the poroelastic stresses. More recently, semi-analytical solutions for fluid production/injection stress changes in poroelastic media have been modelled using the theory of inclusions (Soltanzadeh and Hawkes, 2008). It was shown that, during reservoir depletion considering a horizontal reservoir with rectangular cross section, fault reactivation should occur under normal faulting regime near the flanks of the reservoir and within the center.

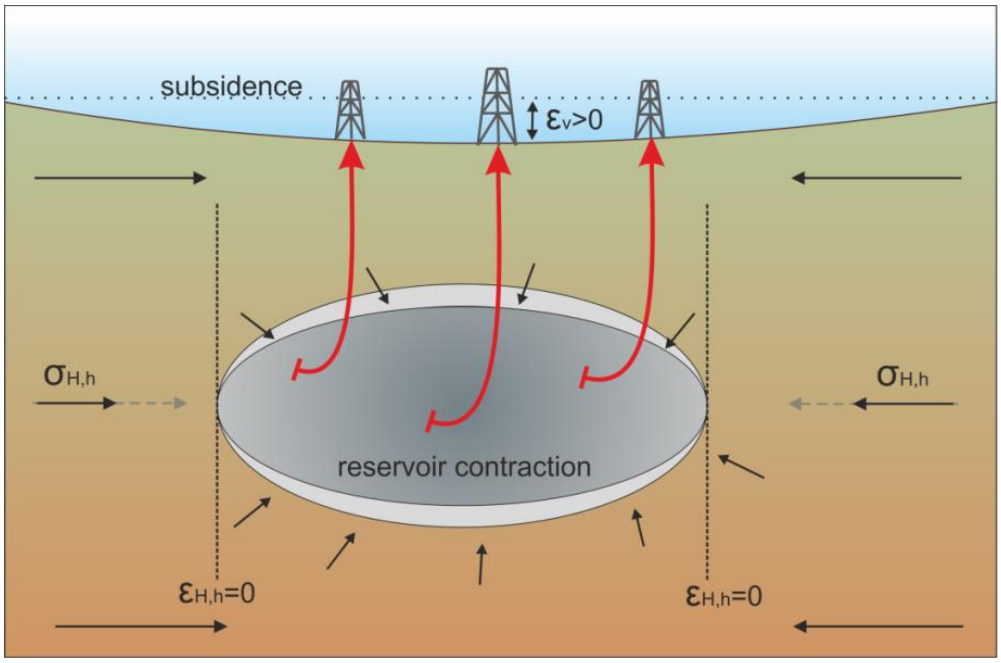

Figure 1.9 Conceptual sketch representing a reservoir where long term production has been performed. The reservoir experiments a volumetric contraction and the horizontal stresses at reservoir depth decrease. Additionally, subsidence occurs.

Still, the question whether the pore pressure could induce locally a rotation of the stress field orientation is not clear. Day-Lewis, (2008) used analytical and numerical models with different reservoir shapes to explain rotations of in-situ horizontal stresses based on pore pressure change, the initial horizontal differential stress and the orientation of the reservoir boundary with respect to the original direction of the maximum horizontal stress. Day-Lewis, (2008) predicted that all these factors can lead to stress rotations in the horizontal direction. However, the model predicted larger stress rotations than observed for two case studies of reservoir depletion. Lately, Altmann et al., (2014) have provided an analytical base for the long-term changes in the 3D stress tensor components as a function of pore pressure changes, using as less assumptions as possible and particularizing the scenario for each stress regime. Their results suggested that the poro-elastic stress changes can modify locally the given tectonic stress regime.

During the Chapters 4 and 5, the rotation of the stress field was addressed in the context of fluid injection in the reservoir. Since results shown temporal rotations of the stress field due to fluid injection, the analysis was extended to interpret the potential causes of the stress rotation in this study.

1.5 Characteristics of fluid-induced seismicity

In order to have an idea on the state-of-the-art knowledge on certain characteristics of the fluid-induced seismicity, this subsection provides a short summary of proposed key-

concepts and observations based on seismicity from geothermal sites and hydraulic fracturing experiments. The fundamentals should also be applicable to any other fluid-injection activity.

Triggering-front of seismicity

The spatio-temporal distribution of the seismicity induced by fluid injection has been described with the concept of the triggering front (Shapiro et al., 2002). This is based on the idea that the pore pressure perturbation propagates further away from the well with time as the pore pressure front evolves (Shapiro et al., 2003; Shapiro, 2008). The maximum distance measured from the injection point at which seismicity is expected to occur at a certain time after the beginning of injection is described by:

$$r = \sqrt{4\pi D t} \qquad [1.12]$$

Where r is the radial distance from the injection point, D is the hydraulic diffusivity of the medium and t is the time since the injection started. The concept of the triggering front has been verified in hydraulic fracturing experiments such as Barnett Shale or Cotton Valley (Shapiro, 2008) as well as for geothermal sites, such as Fenton Hill (Shapiro, 2008) and Paralana (Albaric et al., 2014). This concept was developed for an injection pulse.

Back-front of seismicity

The concept of the back-front of the seismicity was introduced by Parotidis et al., (2004). The idea is that once the fluid injection has stopped, the pore pressure near the well decreases as the pore pressure front propagates further away from the well. As a result of the pore pressure relaxation, seismicity does not occur near the well, but it only starts at a certain distance where the pore pressure perturbation is still sufficiently high (Shapiro, 2008). The distance from the injection well at which the seismic activity starts to occur would be given by:

$$r_{bf} = \sqrt{2dDt\left(\frac{t}{t_0} - 1\right)\ln\left(\frac{t}{t - t_0}\right)} \qquad [1.13]$$

Where r_{bf} is the radius of the back front from the injection well, d is the dimension of the space where pressure diffusion occurs, D is the hydraulic diffusivity, and t_0 is the time at which injection stops. This phenomenon was first predicted by numerical modelling and then also observed in field data from Fenton Hill and Cotton Valley, USA, as well as from the beginning of the stimulation at the EGS-HDR in Soultz-sous-Forêts, France.

Kaiser effect

The Kaiser effect (Kaiser, 1953) states that the seismic activity in a fluid-injection experiment will appear only if the injection rates/volume of fluid injected exceed those from previous stages. It represents an indication of "crustal memory" and it points out the necessity of overcoming previous stress limits to induce micro-seismicity.

The effect was firstly observed from laboratory acoustic emission experiments. During the different loading cycles performed, the seismic activity only resumed beyond the peak load of a previous cycle (Kaiser, 1953). Afterwards, several Kaiser-Effect-based methods have been developed to determine the state of stress in a sample during acoustic emission experiments (e.g. Wang et al., 2000; Lavrov, 2003; Tuncay and Ulusay, 2008).

In reservoirs undergoing fluid injection, the Kaiser effect was first observed at the KTB project (Baisch et al., 2002), where crustal volumes seismically active at a certain pressure where not active afterwards under the same conditions. Later, three dimensional finite-element modelling was used to describe the seismicity from the fluid injection experiments at Soultz-sous-Forêts (France), Cooper Basin (Australia), and Basel (Switzerland). For these geothermal sites, the spatio-temporal patterns of the seismicity were explained using a Kaiser effect (Baisch and Vörös, 2010). More recently, Kaiser effect was also observed at Berlín Geothermal Field (El Salvador) (Kwiatek et al., 2014a).

Shape of the seismicity cloud

Seismicity clusters with approximately ellipsoidal shapes have been observed in some geothermal experiments as for example in Soultz-sous-Forêts, France (e.g. Cuenot et al., 2006), or more recently during the injection experiment in the gas field Zigong, China (Lei et al., 2013). In contrast, more planar structures perpendicular to the direction of minimum horizontal stress are observed typically during hydraulic fracturing stimulation.

To explain the ellipsoidal shape of the seismicity cloud, Shapiro et al., (1999, 2003) proposed an approach introducing anisotropy in the hydraulic diffusivity of a rock, and hence, in the permeability tensor. The results were tested using data from the geothermal sites Fenton Hill, USA and Soultz-sous-Forêts, France. Later on, Schoenball et al., (2010) concluded from synthetic studies that anisotropy of the stress field also results in an ellipsoidal shape of the seismicity cloud. Therefore, these two potential causes are equally possible and indistinguishable in terms of the elliptical shape of the cloud.

Also, the shape of the seismic cloud is suggested to be influenced by the tectonic stress regime (Grob and van der Baan, 2011), from having a more planar shape in strike-slip environments towards a more planar-to-spherical distribution in normal faulting environments.

Lithology

The idea that the injection in crystalline rocks (e.g. granites) may induce more seismicity and with larger magnitudes than the corresponding injection in sedimentary rocks (e.g. sandstone) was questioned by the review of 41 European case studies involving fluid-injection from geothermal and CO_2 storage activities (Evans et al., 2012). After making a separation between these two types of rock environments, the data indeed supported the idea that injection in sedimentary rocks tends to be less seismogenic. However, the data was not totally consistent with the fact that larger events might be induced in crystalline rocks.

More recently, Gaucher and Kohl, (2014) have compared the reservoir response to injection from two geothermal sites (Soultz-sous-Forêts, France and Gross-Schoenebeck, Germany) with crystalline and sedimentary geologies, respectively, but similar conditions in

both levels of natural seismicity and local stress field. They concluded that the induced seismicity level might also depend on the stress field, the porosity of the rocks and the existence of pre-existing faults/fractures.

Large Magnitude Events (LMEs)

Given the socio-economic impact that the occurrence of LMEs has in a fluid injection/extraction project, special attention has been given to their characterization and mitigation.

Empirical observations suggest that there is a large probability for the occurrence of LMEs during or after the shut-in of the injection well. This effect has been related with the increase with time of the area of fluid overpressure (Baisch et al., 2010). Table 1.3 presents a summary of projects where the observed seismic event with maximum magnitude has occurred after shut-in.

In a similar way, it has been observed that there could be a tendency for the LMEs to occur close to the perimeter of the stimulated rock mass. This was observed for example at Soultz-sous-Forêts and Basel Deep Heat Mining Project (Deichmann and Giardini, 2009) and later reproduced by numerical simulations (Baisch et al., 2010). However, these observations might or might not be representative of the potential spatial patterns of the LMEs.

Shapiro et al., (2007) studied different quantities influencing the expected earthquake maximum magnitude. Assuming a constant injection pressure p_0, it was proposed that the number of induced events at a given time $N_{\geq M}(t)$ with magnitudes larger than M is described by the following expression (Shapiro et al., 2007):

$$\log N_{\geq M}(t) = \log\left[\frac{4\pi p_0 R_r t D}{F_t}\right] - bM + a, \qquad [1.14]$$

where R_r is the radius of the borehole, D is the hydraulic diffusivity of the medium, the quantity F_t depends on the tectonic activity in the injection region and a, b are the coefficients of the Gutenberg-Richter's relation. The proposed relation was applied to the datasets from the injection fields Paradox Valley, USA and Ogachi, Japan.

The stimulated rock volume and, more specifically, the shortest principal axis of the seismicity ellipsoid has also been proposed to provide constraints on the corresponding largest expected magnitudes (Shapiro et al., 2011). In particular, a larger shortest principal axis of the seismic ellipsoid results in a larger expected magnitude.

Finally, a recent study by McGarr, (2014) has shown that the seismic event with maximum magnitude observed in several fluid-injection case studies is capped by the total volume of fluid injected in the reservoir and not directly by the injection rates, which would be more related with the seismicity rate.

As a strategy to address the seismic hazard of a fluid-injection project, the "Traffic Light System" was developed (Bommer et al., 2006; Majer et al., 2012). This system is based

Site	M_W	References

Soultz, France	2.7, 2.9	(Baria et al., 2004; Evans et al., 2012)
Landau, Germany	2.7	(Evans et al., 2012)
Basel, Switzerland	2.7, 3.4	(Evans et al., 2012)
Cooper Basin, Australia	3.7	(Baisch et al., 2006, 2010)
Berlin, El Salvador	4.4	(Bommer et al., 2006)
Castor, Spain	4	(Cesca et al., (subm.))

Table 1.3 Examples of fluid-injection projects where the observed seismic event with maximum magnitude occurred during or after the shut-in of the injection well (completed after Baisch et al., (2010)).

on the real-time evaluation of the Peak Ground Velocity (PGV) from seismic recordings. The obtained PGV values are translated into three categories (traffic light colors) based on predefined threshold levels of PGV. This allows the operator to make a decision on whether the injection is appropriate (green), should be performed carefully (orange), or immediately stopped (red). Such systems are not capable of addressing the occurrence of a LME after the shut-in of the injection.

Evolution of *b* value with time/distance/stress regime

The *b* value, defined as the slope of the logarithmic Gutenberg-Richter's relation, gives an idea of the proportion between the number of seismic events of different magnitudes. High *b* values correspond to seismic catalogs containing relatively more seismic events with low magnitudes, while low *b* values correspond to datasets with relatively fewer seismic events but greater magnitudes.

The *b* values were observed to be related to the different tectonic regimes for the seismicity catalogs of California and Japan (Schorlemmer et al., 2005). The highest *b* values were observed for normal faulting environments, intermediate values were attributed to strike-slip faulting, and the lowest *b* values were found for thrust faulting environments.

Some studies have investigated the evolution of the *b* values with fluid injection activities. Bachmann et al., (2011) calculated the *b* values corresponding to the co-injection periods and the post-injection periods for the Basel Deep Heat Mining project. They found that the *b* values decreased in the post-injection period with respect to the co-injection period. In a next step, the distribution of *b* values was calculated with distance from the injection well (Bachmann et al., 2012). *b* values were found to decrease with distance from the injection well and attributed to the corresponding decrease in the pore pressure.

Other studies have looked for the distribution of *b* values between the co-injection and the post-injection periods. In the Zigong gas storage reservoir, China (Lei et al., 2013), an unusual increase of the *b* value was found during the last stages of the injection, caused by the substantial increase in seismicity with low magnitudes. Also, Cesca et al., (subm.) reported that the *b* values substantially decreased after the shut-in of the injection at the Castor gas storage project, Spain.

1.6 Description and comparison of case studies

During the following studies two main sites associated to different fluid-injection activities have been investigated. This section provides an introduction and comparison of both case studies to have an initial perspective about what can be learnt from them.

In the first case study, potential seismicity and leakage signals were investigated in relation to the injection of supercritical CO_2 in the Penn West Pilot in Alberta, Canada, as part of an EOR program (Chapter 2). The seismic instrumentation consisted in eight borehole seismometers located approximately 300 m away from the injection point. CO_2 injection was performed for approximately 6 months. During the here analyzed period of two-weeks, an outflow of CO_2/brine through the monitoring well occurred. Initially, the dataset seemed particularly promising given previous seismic detection of degassing processes associated with CO_2 leakage through the monitoring well at the Michigan Basin CO_2 injection project (Bohnhoff and Zoback, 2010; Bohnhoff et al., 2010b).

The second case study incorporated induced seismic activity at The Geysers geothermal field in Northern California, USA was analyzed. Steam production and subsequent water injection to refill the reservoir has been performed since the 1960s. To monitor the seismicity induced in the field, a local seismic network composed of 34 stations is permanently deployed at the surface, but seismic events may be also recorded by other numerous regional seismic stations. Given the abundant seismicity, many of the here reported studies are focused on a selected seismic cluster of the field, although some analyses based on the seismicity from the entire reservoir have also been performed.

The most important link between both projects is the fluid injection performed into a target reservoir, suggesting that similar processes may lead to the occurrence of induced seismicity, such as poroelastic changes due to fluid injection and/or extraction. Another common aspect is the type of reservoir rock (sandstone). Sandstone is a clastic sedimentary rock composed mainly of sand-sized minerals or rock grains. However, given the wide variety of sandstone rocks with different properties, it does not necessarily mean that the reservoir rocks are equal (Fig. 1.10). At Penn West, the reservoir is composed of various arenaceous sandstone beds and characterized by one or more sequences grading from shale to sandstone (Krause et al., 1994). At The Geysers, the reservoir is composed of Franciscan assemblage greywacke sandstone, which is a hard type of sandstone with low porosity.

The reservoir depths are not very different. At Penn West, the CO_2 is injected into the Cardium Formation, which is located at approximately 1650 m depth and has an approximate thickness of 20 m. At The Geysers, the geothermal reservoir is located approximately between 2 and 3 km. Still, this difference in the reservoir depths results in different vertical in-situ stresses in the reservoir, which may have indirect implications in the occurrence of induced seismicity.

However, the injection volume is completely different. The scale of fluid-injection performed at The Geysers is by far larger than the injection performed at Penn West. At The Geysers, only in one injection well, an average of $0.15 Mm^3$ is injected every month (Source: Department of Conservation, State of California). At Penn West, neither the flow rates nor the volume of CO_2 injected were available, but they were very likely significantly lower.

a) b)

Figure 1.10 a) Core samples from the Penn West Pilot Project (5 m above the target formation) (Courtesy of Gonzalo Zambrano-Narváez) b) Core samples from The Geysers geothermal field. Left: Greywacke sandstone from the reservoir not very fractured Right: Greywacke sandstone from the reservoir with natural tiny fractures increasing the permeability (Source: The Geysers Visitor's Centre, Middletown, California).

The thermodynamic status of these reservoirs is also substantially different. At Penn West, the initial reservoir temperature and pressure were 50°C and ≈19MPa, respectively (Coueslan, 2007). At The Geysers, the reservoir temperature below 2 km is estimated in 240°C (García et al., 2012) and the initial encountered reservoir pressure was 3.5 MPa, progressively decreasing due to the reservoir depletion (Williamson, 1990). Therefore, it is a vapor dominated reservoir substantially under-pressurized where water falls freely into the wells without necessity for elevated injection pressures.

Chapter 2

Microseismic monitoring of CO_2 injection at the Penn West EOR Pilot: Implications for detection of wellbore leakage[1]

[1] Published in *Sensors (Basel, Switzerland)*, as Martínez-Garzón, P., Bohnhoff, M., Kwiatek, G., Zambrano-Narváez, G. and Chalaturnyk, R. (2013). Microseismic monitoring of CO_2 injection at the Penn West EOR Pilot, Canada: Implications for detection of wellbore leakage. 13(9): 11522–11538. doi: 10.3390/s130911522.

Summary

A passive seismic monitoring campaign was carried out in the frame of a CO_2–EOR pilot project in Alberta, Canada. Our analysis focuses on a two-week period during which prominent downhole pressure fluctuations in the reservoir were accompanied by a leakage of CO_2 and CH_4 along the monitoring well equipped with an array of short-period borehole geophones. We applied several state of the art seismological processing schemes to the continuous seismic waveform recordings. During the analyzed time period we did not find evidence for induced micro-seismicity associated with CO_2 injection. Instead, we identified signals related to the leakage of CO_2 and CH_4, in that seven out of the eight geophones show a clearly elevated noise level framing the onset time of leakage along the monitoring well. Our results confirm that micro-seismic monitoring of reservoir treatment can contribute towards improved reservoir monitoring and leakage detection.

2.1 Introduction

One of the key-challenges in the frame of long-term storage of CO_2 is to deliver appropriate monitoring techniques that allow to document and quantify whether CO_2 can be safely stored at selected sites (IPCC, 2007; Schrag, 2007). Amongst the approaches to monitor long-term CO_2 storage, Passive Seismic Monitoring (PSM) can deliver critical information on the effects of pressure perturbation and fracture generation. PSM also allows tracing fluid propagation within the reservoir, within the caprock or along wellbores using locations of small-scale induced earthquakes detected at borehole geophones.

PSM is a well-established method both in the hydrocarbon and geothermal industries where it is used to monitor reservoir stimulation and in fundamental research with various applications in earthquake seismology. There are several studies that use this technique to characterize the treatment of different types of reservoirs (Ruthledge et al., 1994; Majer et al., 2007; Shapiro, 2008; Bohnhoff et al., 2010a; Kwiatek et al., 2010). Despite the great potential of the method, it has not yet been systematically applied to the field of CO_2 storage. However, recent discussions on the feasibility of large–scale CO_2 storage considered including also potential risks posed by induced seismicity (Zoback and Gorelick, 2012).

There is an extensive knowledge supporting the idea that regions with the highest potential for CO_2 storage are basins with thick sequences of sedimentary rocks (Bachu, 2002). This is the case at the Pembina Oil Field in Alberta/Canada, where the Cardium Formation (capping siltstones, shales, and sandstones) is confined between Marine Shales and the Blackstone Formation (Krause et al., 1987). Recent studies support the view that injection in sedimentary rocks generally tends to be less seismogenic than in crystalline rocks (Evans et al., 2012), which is consistent with observations of sparse amounts of induced seismic events all being of low magnitude during and after CO_2 injection in sedimentary formations (Bohnhoff et al., 2010b; Verdon et al., 2010; Oye, 2012). However, the few existing case studies are far from being representative in general and more pilot field studies are needed to derive quantitative statements on the probability of inducing micro-seismicity during and after CO_2 storage.

A CO_2-EOR (Enhanced Oil Recovery) pilot project was initiated in 2005 at the Pembina Oil Field as part of a CO_2 royalty credit program established by the Alberta Government. There, CO_2 was injected into the Cardium Formation located at 1650 m depth with the purpose of enhancing the production of the field. This multidisciplinary research project comprised various studies including geophysical monitoring, reservoir monitoring and reservoir stimulations of CO_2 movement (Gunther, 2008; Hitchon, 2009).

As part of this effort, a PSM campaign was carried out between 2005 and 2008 using an array of eight three-component borehole geophones. Some of the advantages of using borehole geophones are the substantial improvements of noise conditions with respect to the surface as well as the reduction in the attenuation of the signals since the geophones are placed below the uppermost weathering layer and (to some extent) closer to the target reservoir. This results in better quality of the seismic waveforms providing a higher precision for hypocenter locations and a reduced magnitude-detection threshold of the geophone array.
In this study we focus on a two-week time period of continuous seismic recordings. The time window was selected for two reasons. First, we wanted to investigate whether any induced micro-seismicity is occurring in the frame of the EOR-related CO_2 injection into the reservoir. Second, this time period includes a substantial outflow of CO_2 and CH_4 observed at the well-head of the monitoring well and we wanted to investigate whether the outflow resulted in any sort of seismic signatures at the borehole geophones that might serve for an improved detection of gas flow along wells (leakage). The state-of-the-art seismological analysis methods to detect potentially occurring induced seismicity and/or elevated noise levels during the CO_2/CH_4 outflow were applied.

2.2 Input Data

To achieve a comprehensive multi-parameter monitoring of the target reservoir, instrumentation was deployed in a pre-existing vertical production well refurbished as monitoring well (Zambrano-Narvaez and Chalaturnyk, 2007). The monitoring well was located at approximately 300 m lateral distance to the nearest injector well I1 (Fig. 2.1a). Among the deployed monitoring instrumentation there were eight 3-component short-period geophones with a natural frequency of 24 Hz. The geophone string was placed inside the monitoring well between 1500 m and 1640 m depth (see Fig. 2.1b). Sampling frequency for continuous seismic recordings was set to 1 kHz to ensure the ability to record also the higher frequency signals contained in potentially occurring micro-seismic events down to M_W -1.5 (Kwiatek et al., 2011). As the casing was lowered into the well the geophones were still able to rotate around the vertical axis. For this reason, the horizontal orientation of each sensor is different (Coueslan, 2007). Further elements of the monitoring instrumentation were three pressure–temperature sensors and two fluid–sample sensors. Additionally, both injector wells (I1, I2, see Fig.2.1a) had also a pressure sensor at the wellhead.

At the Cardium Formation, the CO_2 was injected in supercritical state with the purpose of enhancing the production of oil. Thus, a percentage of the injected CO_2 was systematically released again dissolved in the produced oil. The two-week time period considered in this study extends between 26th August and 11th September, 2005. Before, CO_2 injections had been suspended for 20 days due to the high percentage of CO_2 detected in the oil. During the first two days of the analyzed time period CO_2 injection was resumed and seven noticeable injections (ΔP = 5 MPa) took place through injector I1. The injections resulted in an increase

(a)

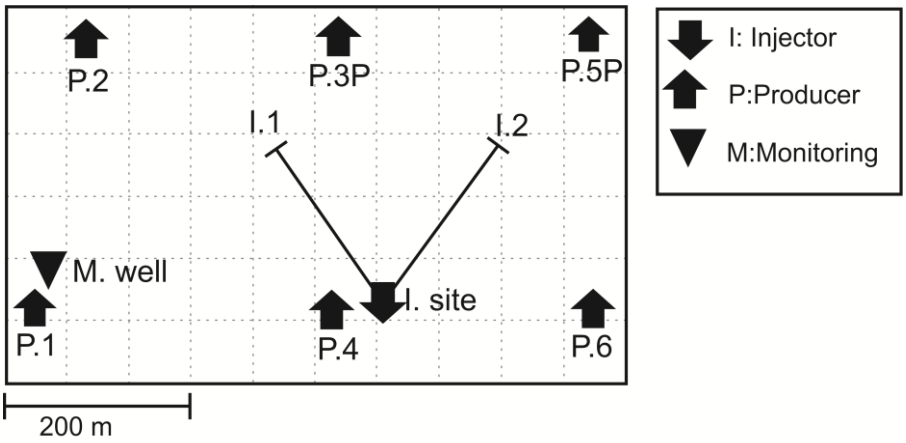

(b)

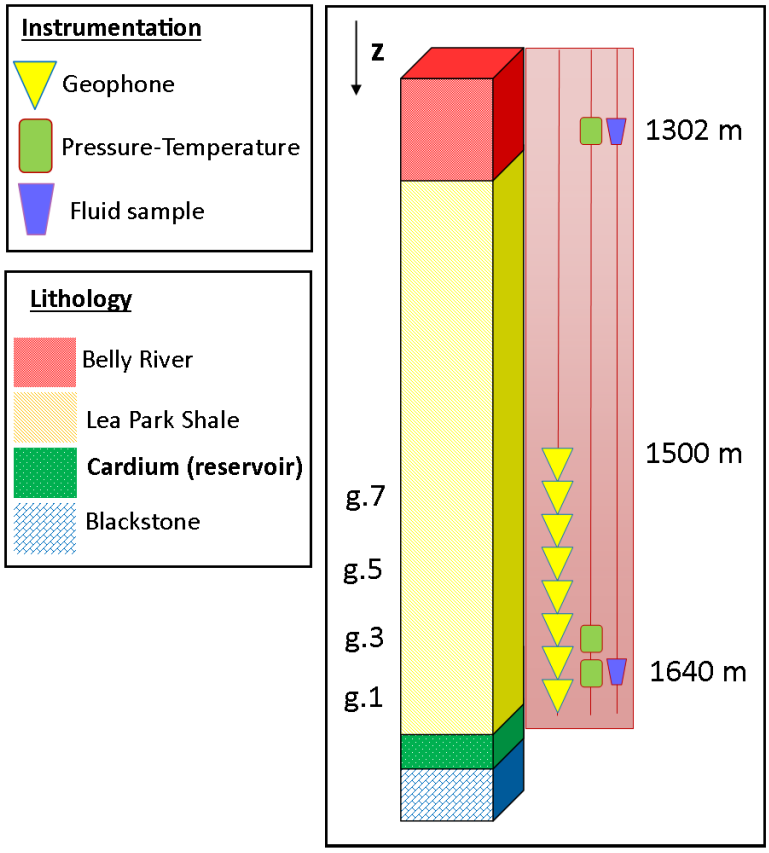

Figure 2.1 (a) Location of the monitoring well (triangle) with respect to the injector (arrows pointing down) and the producer wells (arrows pointing up). P.1: New producer well. P.2-6: Pre-existing producer wells. I.1, I.2: Injector wells (directional wells). (b) Lithological column at Penn West Pilot Project and instrumentation deployed in the observation well. Geophone 1 (g.1) is the deepest sensor, placed at 1640 m. Geophone 8 (g.8) is the shallowest, placed at 1500 m. The distance between sensors is 20 m.

in the percentage of CO_2 in the produced oil, leading to the decision to open up the well-head of the monitoring well which resulted in a subsequent outflow of CO_2 and CH_4 (Zambrano-Narvaez and Chalaturnyk, 2011).

2.3. Methods and Results

The processing scheme applied to the continuous seismic recordings consists of four main parts documented in the following subsections. First, spectrograms were generated to visually inspect the general frequency content of the obtained waveform recordings. Second, we systematically analyzed the average noise levels at each individual sensor to determine times of enhanced noise levels that might be associated with any kind of external process such as e.g. nearby fluid flow. Third, we applied a signal-detection algorithm (STA/LTA) conventionally used to identify micro-seismic signatures in continuous waveform recordings. Fourth, we analyzed the lower frequency band of the recorded spectra (< 100 Hz) to identify potentially occurring slow-slip or tremor-like processes in the reservoir.

We applied a different processing scheme to the continuous seismic time series according to the goals of each subtask. For the calculation of spectrograms and the STA/LTA analysis (Sections 2.3.1 and 2.3.3) recordings were corrected for the baseline shift. We then applied a 2^{nd}-order Butterworth high-pass filter of 0.8 Hz to remove potential long-period signals not associated to any type of micro-seismic events recordable by the used instrumentation. The data displayed significantly increased noise in distinct narrow frequency bands located at 60 Hz and its multiples caused by electrical equipment located nearby. These signals were diminished by applying two notch filters in the intervals [55, 65] Hz and [115, 125] Hz, respectively. For the noise analysis (Section 2.3.2) we worked with baseline-corrected (but not filtered) data since we were interested in all frequencies contained in the data recordings. Lastly, in the analysis of low frequency signals (Section 2.3.4) we applied a 2^{nd}-order Butterworth band-pass filter in the interval [5, 100] Hz.

2.3.1. Spectrograms

Spectrograms allow a complete visual inspection of the frequency content of the waveform recordings during the selected time period. By using spectrograms micro-seismic events could be identified by short-term amplitude increases in the higher frequency parts (usually > 100 Hz, depending on magnitude and hypocentral distance).

To get a first impression of the quality of the data and its frequency content we generated spectrograms for the entire analyzed dataset. We eliminated electronic noise by applying the notch filters as described above. Most of the energy in the recorded time series was transferred in the frequency interval up to 200 Hz (Fig. 2.2). Interestingly, the spectrograms show several short time intervals of elevated energy up to 500 Hz (our Nyquist frequency). Such signals would be part of the frequency characteristics of micro-seismic events and thus would need to be checked in detail. However, most of such signals generally do not show any temporal correlation between the individual geophones. For this reason, they seem to not have an external origin and thus they cannot represent processes related to the injected CO_2 in the storage reservoir.

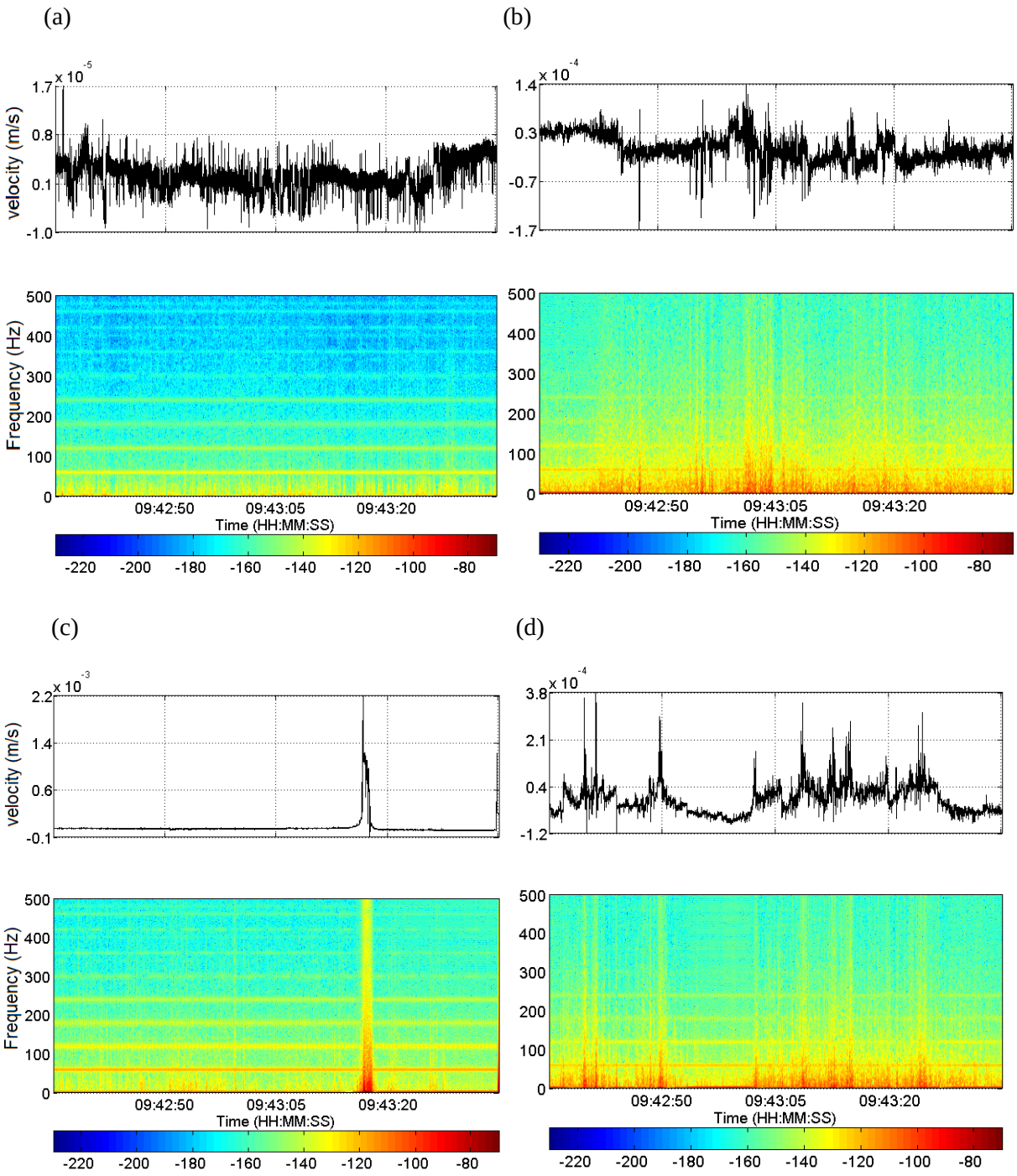

Figure 2.2 Seismograms and spectrograms recorded for different geophones showing one-minute time-windows framing the reported onset time of CO_2/CH_4 outflow. Upper part: Waveform recorded on the vertical component. Lower part: corresponding spectrogram. The amplitude of each frequency appears color-encoded. (a) g.2 shows high electronic amplitudes in the multiple frequencies of 60 Hz. (b) g.3 recorded many sharp spike-signals. (c) g.5 shows a spike with very high amplitude, probably triggered internally. (d) The spectrogram of g.8 is similar to that of g.3 although the spike signals occur at different times.

The spectrograms were also used to investigate the quality of the coupling of the geophones to the tubing string. A general rule of thumb is, that the better the coupling, the larger is the bandwidth of the transfer function of a borehole geophone. We found that all eight geophones are generally capable to record also the higher frequencies indicating a reasonably good coupling to the well-casing, while the deepest sensor (g.1) and also g.3 (Fig. 2.1b) seem to have the best coupling.

Scanning the spectrograms of all sensors for the two-week time period shows that functionality of the downhole geophones is given. None of the clear high-amplitude signal seen at all (most) sensors could be related to an induced micro-seismic event occurring off the array.

2.3.2. Noise Level Analysis

Analysis of the average noise level at the geophones throughout the recording period can provide useful information to determine the quality of the individual geophones (e.g. due to poor coupling or mechanical dysfunction). More importantly, a systematic search for time periods with increased noise levels at several/all sensors could be an indication for injection-related processes in the reservoir or potential leakage along the monitoring well. We carried out noise-level analysis for each individual geophone through the entire two-week data based on one–minute long subsets. This procedure aimed to detect elevated noise conditions levels at the geophone string in the monitoring well.

In general, we find that noise amplitudes are relatively higher at the sensors g.1 and g.3 (Fig. 2.1b). In contrast, g.2 and g.6 recorded significantly lower amplitudes, on average three orders of magnitude less than the others. As indicated also by the spectrograms, this suggests an existing difference in the pre-amplification and/or coupling between these pairs of sensors, while it is entirely unlikely to be caused by varying external noise. Additionally, the higher amplitudes of g.1 and g.3 might be partially related to their proximity to the reservoir being located at only 10 and 50 m vertical distance, respectively. This analysis also revealed that for the last 1.5 days of the two-week period, g.2, g.4 (partially) and g.6 were not recording. Comparing these observations with the field protocols, the geophones with odd number shared one common cable and the geophones with even number shared a second cable. This resulted in two cables running to the surface. Since common characteristics between the even geophones are found, a second explanation for the low amplitudes recorded thus would be a higher resistance of the even cable with a corresponding higher attenuation of the signal.

During the enhanced outflow of CO_2 and CH_4 along the monitoring well as described above, we find a dramatic increase of the noise level for seven out of the eight geophones framing the approximate onset time of the outflow (9:41 AM) (Fig. 2.3a). The respective waveform recordings for the time of the outflow (five minutes framing its onset) are plotted in Fig. 2.3b. They show clear differences in the waveform signals before and after the start of the outflow, which might indicate the arrival of the CO_2/CH_4 front at the geophone array. We then calculated the average noise level at higher sampling using one-second time windows for each component of every geophone during five minutes framing the outflow onset. Fig. 2.3c shows that during this period there is no clear preference for the outflow detection in terms of the vertical or horizontal components. Additional review of the data indicates that the

Geophone number	Geophone status
8	Correct
7	Horizontal component (X) not recording
6	Both horizontal components not recording
5	Correct
4	Correct during certain periods
3	Correct. High noise level (average amplitudes).
2	Horizontal components not recording.
1	Correct. High noise level (average amplitudes).

Table 2.1 Summary of geophone status obtained from spectrograms, noise level analysis and manual review of the data. Geophones are sorted according to their depth (g.8: 1500 m, g.1: 1640 m).

horizontal components of certain sensors display much lower amplitudes than the verticals during the whole analyzed period. Functionality of each geophone is summarized in Table 2.1.

The onset of the outflow can generally be described as a period with extremely disturbed noise levels at the geophones while no uniform waveform signatures are identified amongst the individual sensors. Interestingly, the arrival times of the elevated noise levels are not displaying a linear move out along the array, but in contrast are time-delayed with no systematic order. To further investigate these signals, we investigated the pressure data measured by the sensors installed at the monitoring well (Figs. 2.1b+2.4). At the time of the onset of the outflow, the pressure at the sensor installed at 1640 m decreased by 1 MPa, while the pressure in the sensor installed at 1300 m increased by 300 kPa. Thus, there was a dramatic gradient of pressure with both depth and time which subsequently recovered to the respective pre-outflow level after approximately 2 hours. The gradients registered in the pressure support the interpretation of the detected noise level perturbations as a signal related to the CO_2/CH_4 migration along the well.

2.3.3. STA/LTA Analysis

In order to carry out an automated search for micro-seismic signals throughout the two-week time-series, we applied a Short Time Average/Long Time Average (STA/LTA) triggering analysis based on the amplitude of the signals to the vertical components of each geophone. A STA/LTA trigger detects onset times of characteristic signals (e.g. seismic P and S waves) based on a defined minimum of the ratio of average absolute amplitudes of two time windows of different length. The (theoretical) STA/LTA ratio within noise is one while this ratio would increase once an elastic wave reaches a geophone. Once a pre-defined threshold for the STA/LTA ratio is reached at a particular sensor the time is saved as detection time and can later be cross-correlated with the detection times of the other sensors.

A total of four parameters need to be fine-tuned for a specific data set before applying the STA/LTA algorithm. Due to the lack of regional seismicity and since no calibration shots were available, we tuned these parameters based on the accurate detection of several different

(a)

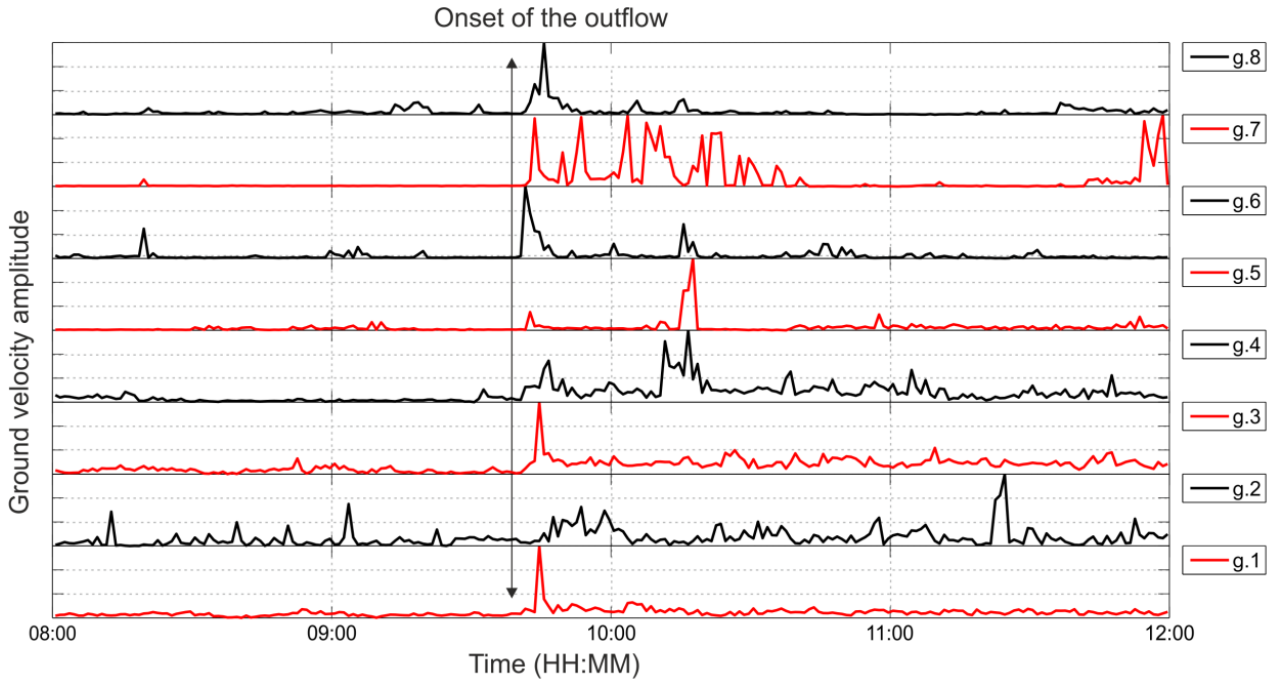
Onset of the outflow
Ground velocity amplitude
g.8
g.7
g.6
g.5
g.4
g.3
g.2
g.1
08:00
09:00
10:00
11:00
12:00
Time (HH:MM)

(b)

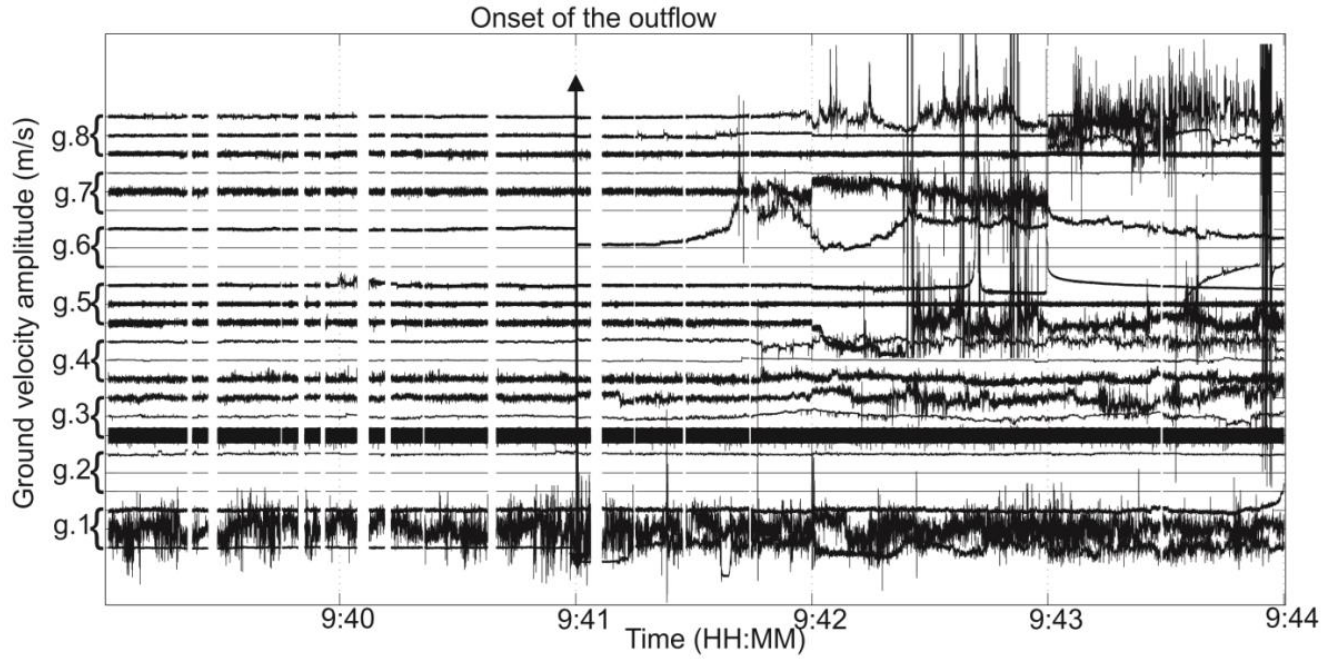
Onset of the outflow
Ground velocity amplitude (m/s)
g.8
g.7
g.6
g.5
g.4
g.3
g.2
g.1
9:40
9:41
9:42
9:43
9:44
Time (HH:MM)

(c)

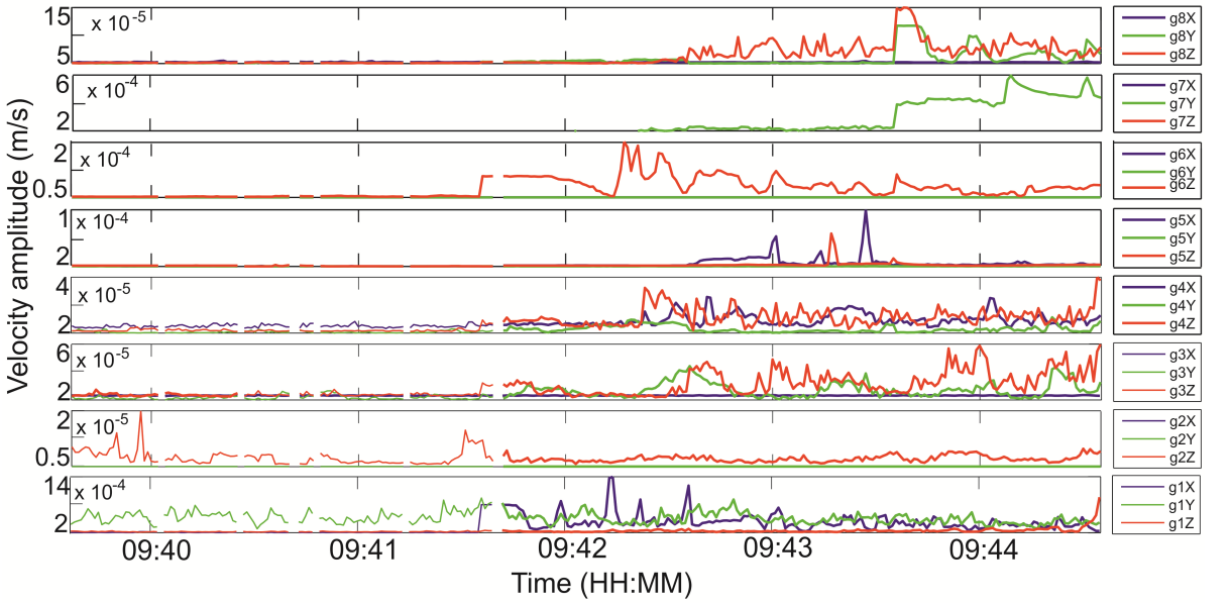

Figure 2.3 (a) Average noise levels at each sensor on 01/09/2005, including the time of the outflow (09:41 AM, indicated by the arrow). Each trace is normalized to the overall maximum of all traces during this time period. (b) Five minutes of waveform recordings framing the onset of the outflow. Traces are normalized to the overall maximum of all traces (g: Geophone). The horizontal white gaps correspond to periods in which the recording was interrupted. The time of the outflow onset is indicated by the arrow. (c) Normalized average noise level for each component of every geophone calculated with 1 s windows.

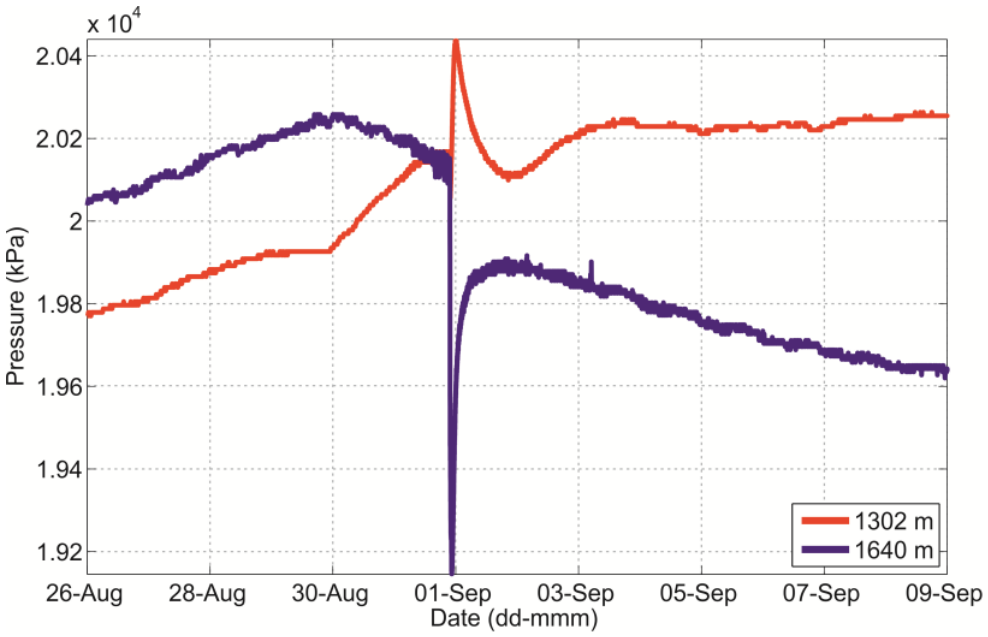

Figure 2.4 Pressure measured by the sensors inside the observation well during the two-week time period analyzed in this study. On 01/09/2005, the deepest sensor (blue) registered a pressure drop of almost 1 MPa within less than one hour. One hour and a half later, the shallowest sensor (red) measured a total increase of 300 kPa. After the outflow, the pressure remained higher at the shallowest level than at the deep reservoir level. This tendency remains during the rest of the analyzed dataset.

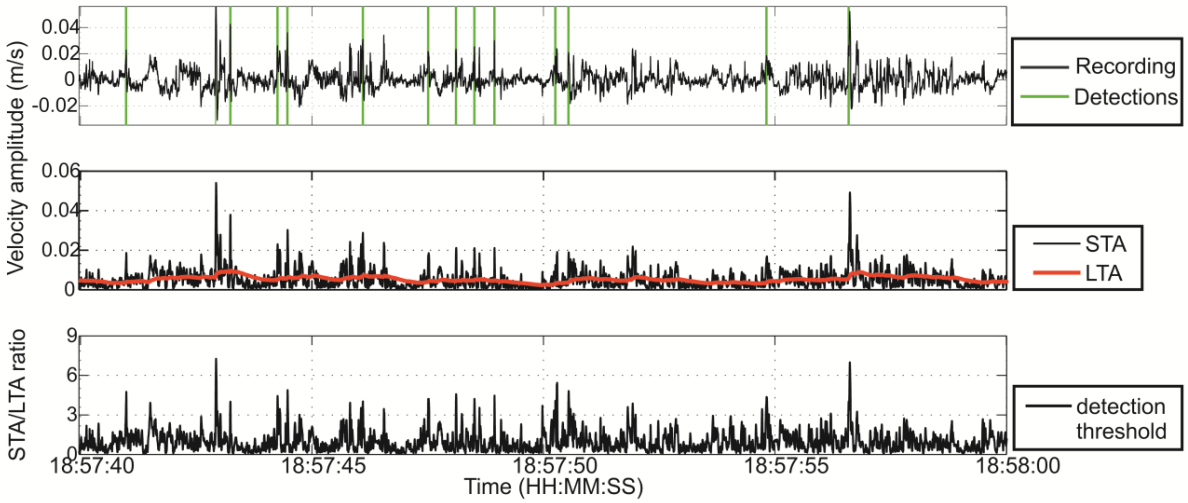

Figure 2.5 Example of waveform analyzed with STA/LTA. The upper plot shows the filtered recordings for 30 s of data. The green vertical lines show the detections of the STA/LTA analysis. The middle plot shows the STA (red) and LTA (black) function for the corresponding data period. The lower plot shows the STA/LTA ratio.

signals visually identified in the data. Fig. 2.5 shows a waveform data example and detections of the STA/LTA algorithm.

The next step was to apply a coincidence trigger to the obtained geophone-specific detection lists in order to select only those seen at a minimum number of four geophones within a given time window (40 ms). We defined the time window length for the coincidence trigger considering the velocity of the formation from (Coueslan, 2007). We used a homogeneous velocity model of V_p = 3.5 km/s, which is slightly lower than the estimated V_p for the formation. As the distance between first and last geophone is 140 m, the window length was settled as $\Delta t = \frac{x}{V_p} = \frac{140\ \mathrm{m}}{3500\ m/s} = 0.004\ \mathrm{s} = 40\ \mathrm{samples} = 40\mathrm{ms}$. The resulting detections were visually checked and classified into six different categories (Fig. 2.6a): A-Type detections have large amplitudes at only one geophone, which suggest that the signal was a spike at this particular sensor (e.g. caused during digitization). B-Type detections typically occur close to the start or end times of periods without recordings (i.e. no seismic origin). C-Type detections display larger amplitudes at more than one, but not all sensors. D-Type detections have extremely low signal-to-noise ratios and thus they can be excluded of further analysis since no reliable onset time can be picked as a pre-requisite for a stable location (potentially very weak seismic signals). E-Type detections belong to periods when the time series exhibit periodic-electronic signals. These signals are not introduced by the data processing, since we can observe corresponding waveforms also in the raw data. Finally, F-Type detections are signals that have high similarity between the different geophones and thus, they have a higher probability to be seismic events. However, even these signals cannot be associated with waveforms typical for induced seismicity, since it is not possible to observe P and S phases. For this reason, none of the categories actually represent clear elastic waveforms resulting from failure of rock but rather very local (in part sensor-specific) signals of different origin. In Fig. 2.6b we have plotted the daily number of detections for each type. Nearly all A-type and most of the E-Type signals occurred after the onset of the outflow.

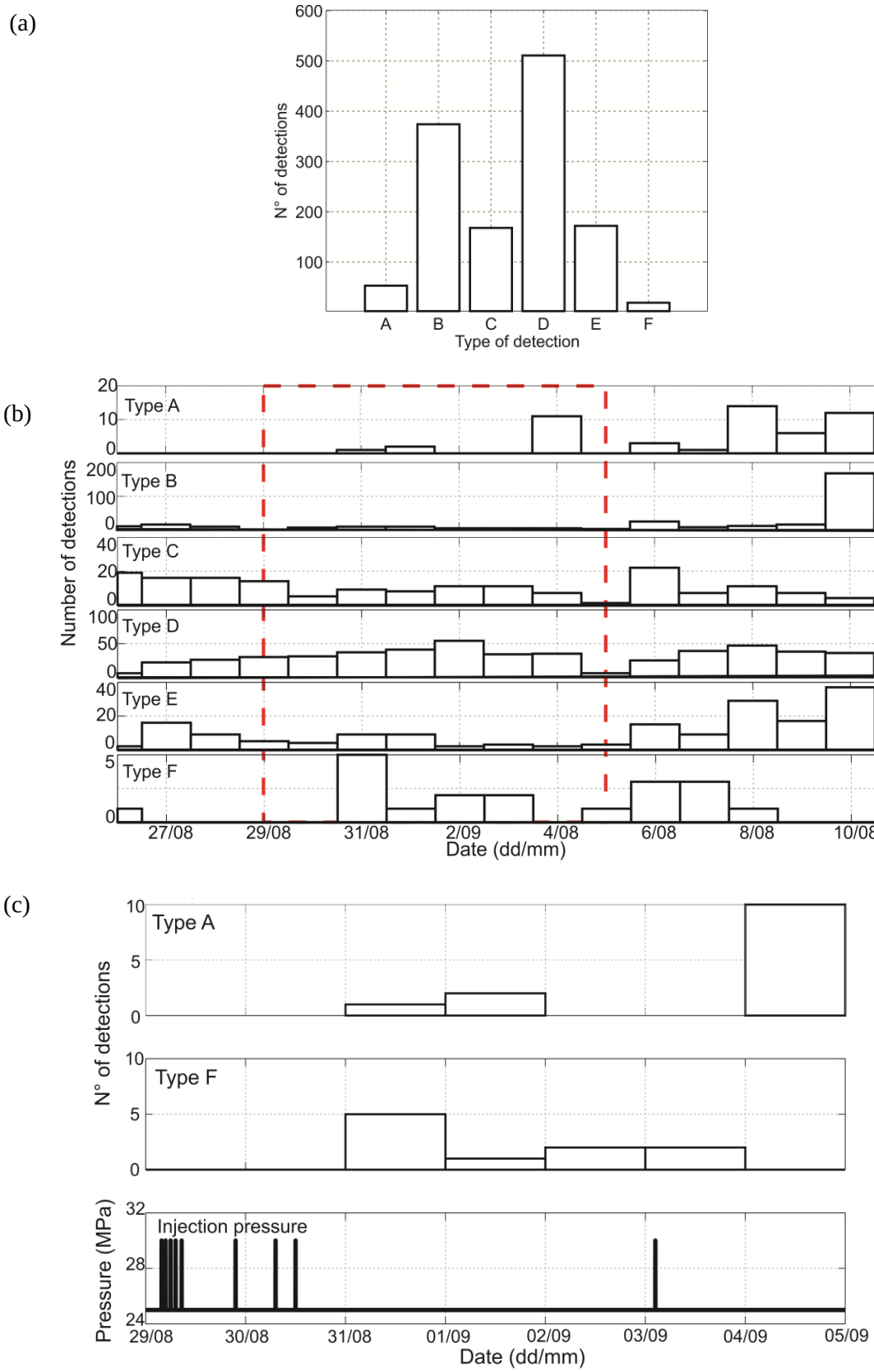

Figure 2.6 (a) Number of detections of each type detected during the whole analyzed period from the STA/LTA. (b) Daily distribution of detection types from A to F. The outflow occurred on 01/09/2005. The red rectangle frames the area enlarged in (c). (c) From top to bottom: Number of detections of Type A, Type F and well-head pressure in the injector well I1 during the represented period, respectively.

Since both types of detections might be related with electrical disturbances, it suggests that the outflow of CO_2/CH_4 could have partially damaged the instrumentation and/or the cables used for the data transmission to the surface. Finally, the highest number of Type-F events is registered the day after the shut-in of injector I1. Interestingly, most of them occurred the day after peak flow rates of CO_2 injection (Fig. 2.6c). It is well known that one of the periods with highest likelihood for induced micro-seismicity due to fluid injection is after the peak injections. This could be considered as a reason in favor of observing Type–F events as weak induced seismicity. Finally, on September, 3rd, when injection was resumed, electronic spikes and spurious signals increased substantially. We speculate that the last injection increased the damage to the cabling/instrumentation resulting in increasing noise levels. Alternatively, the recording equipment at the surface might be responsible for generating these signals (through induction or direct impact of the power net).

Since the geophone array was placed on average 1.6 km below the surface, in case of seismic events with their sources at similar depths of the instruments, they might primarily be recorded on the horizontal components. For this reason, we finally run the STA/LTA test also on the horizontal components. Once again, the obtained results did not reveal any waveform clearly representing induced micro-seismicity.

2.3.4. Analysis of Low-Frequency Signals

To ensure considering all relevant frequency bands potentially related to seismogenic processes in the storage reservoir we also looked for potential waveforms generated by slow-slip processes. At reservoir scale, long-period and long-duration seismic events have been found in a multi-stage hydraulic fracturing experiment conducted in a shale gas reservoir (Das and Zoback, 2011). The authors described events observed during fracturing periods that have a typical duration of 10- 100 s and most of their frequency content is in the interval [10-80] Hz. However, recent studies (Eaton et al., 2013) indicated that such events are not necessarily occurring even when the treatment involves hydraulic fracturing. The Penn West Pilot Project was not designed to include hydraulic fracturing, and thus no such signals are likely to occur. Nevertheless, such studies are still quite sparse and it is worth to analyze the corresponding frequency band.

We first stacked of the amplitudes for all sensors (only vertical components), and then calculated spectrograms of 50 min time-windows by stacking the spectral density of the vertical components (Fig. 2.7a+b). We observe a number of signals that display a similar spectral content and duration as those shown by long-period and long-duration events. However, we cannot exclude other possible sources for these signals, and the signal-to-noise ratio is rather small. Given the unknown orientation of the horizontal components of each geophone, we cannot perform an analogous horizontal stack to check the consistency of these signals in other channels.

The low-frequency data processing pointed our attention towards several signals with similar waveforms of micro-earthquakes, especially following the CO_2/CH_4 outflow. However, these signals have much lower frequencies than those of typical micro-seismic events, and most of them are only detected in one component of an individual geophone. Fig. 2.7c shows the data for 100 minutes. The onset of the outflow is reported to be at around 1000 s. At this time, the spectrogram shows a clear change in the frequency content. We interpret these signals to be associated with the CO_2/CH_4 flow along the monitoring well and

(a)

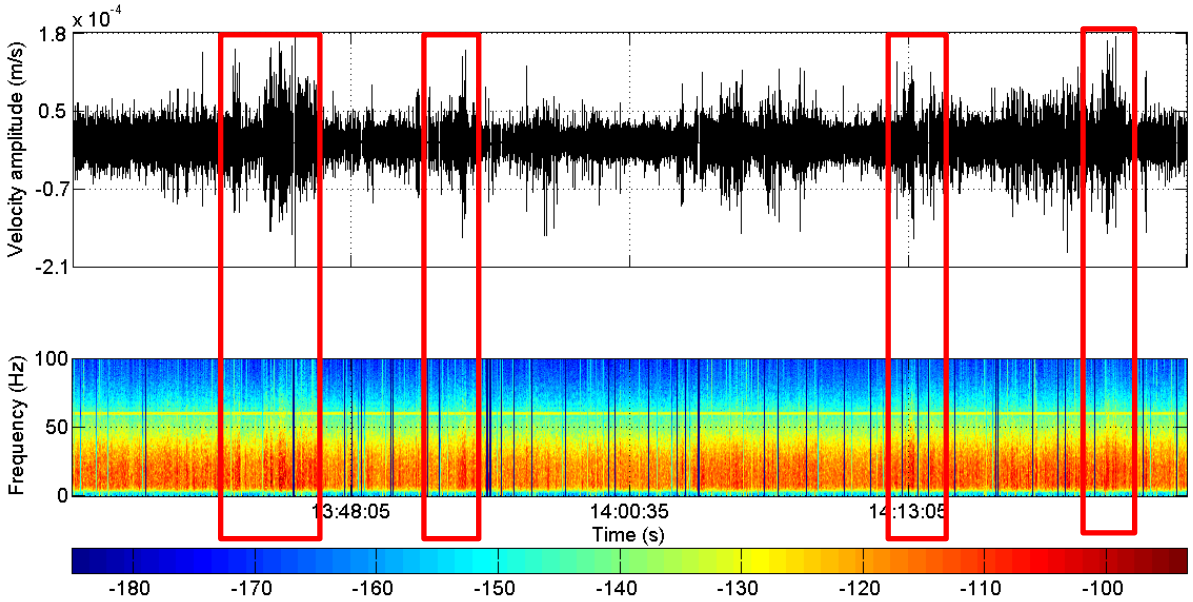

(b)

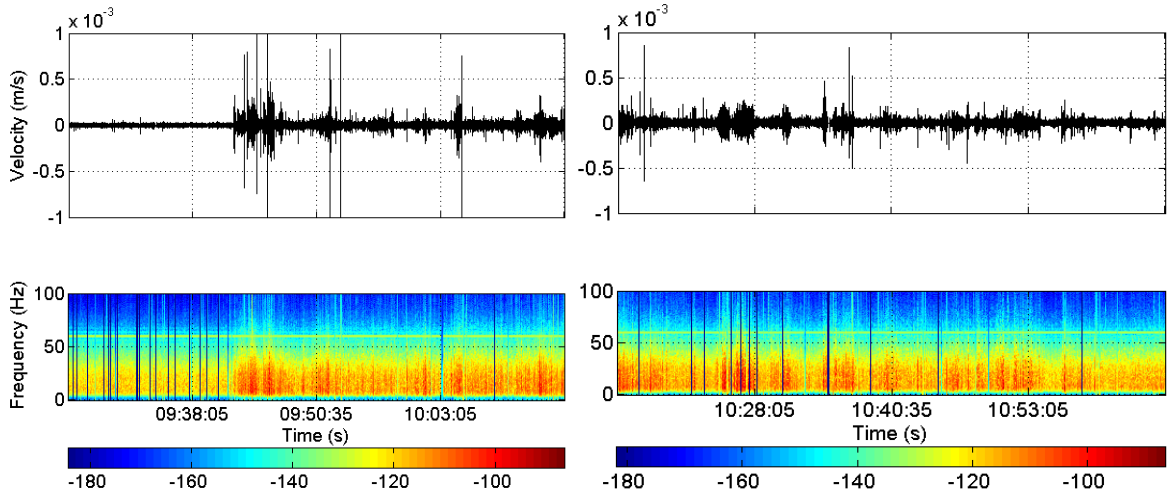

Figure 2.7 (a) Examples of signals with high similarity to long-period and long-duration events found in the two-week period data set. Upper part of each figure: stacking of the amplitudes of the vertical components for each geophone for 50 min. data. These plots have been re-filtered with a 2nd order Butterworth band-pass between 5 and 40 Hz. Lower part of each figure: Spectrograms for the same time period of the upper part, stacking the spectral density for the vertical components of each geophone. The red rectangles in each picture frame potential long-period and long-duration signals. (b) Spectrogram of 100 min time window, from 01/09/2005 at 09:25 AM. Upper part: Stack of the amplitudes for the vertical components of every geophone. Lower part: Spectral density stacking for the vertical components of every geophone.

passing by the geophones. They cannot be related to any external process from off-the geophone array. In any case one needs to keep in mind that the spectrograms in Fig. 2.7c are calculated from stacked signals of all seismic sensors, while not all individual sensors would clearly pinpoint to any sort of external (seismic) event.

In summary, we checked the two-week database for low frequency (< 100 Hz) contents to put the focus on slow slip processes (eventually occurring in the storage reservoir). We found potentially relevant signals on individual components, although no coherent signal in several geophones could be identified, suggesting that no external slow–slip processes are visible during analyzed observation period.

2.4. Discussion and Conclusions

In the Penn West CO_2-EOR Pilot Project there is a small potential for the occurrence of detectable induced seismicity due to its long production record, progressing depletion in the reservoir and the lack of (known) faults in the area. However, induced micro-seismicity might occur mainly due to local pressure perturbations caused by CO_2 injection into the reservoir and/or leakage/migration of CO_2 along the monitoring well and/or through the caprock. In the present study our primary intention was to detect and analyze potentially occurring CO_2-induced seismic signatures focusing on a two-week period framing a substantial CO_2 and CH_4 leakage along the observation well.

The geophone array composed of eight three-component sensors installed in the observation well at 1500-1640 m depth was operating at a sampling frequency of 1 kHz allowing to detect signals with frequencies up to approx. 500 Hz. However, based on the experience from a number of similar field experiments, this frequency is usually reduced due to several factors, and so good resolution up to 300 Hz can be expected for our data set. According to (Kwiatek et al., 2011), assuming a conservative average stress drop of 1 MPa, the sensor array should be able to detect nearby micro-seismicity with reasonable high signal-to-noise ratio for magnitudes down to at least M_W -1.5. Therefore, the network was capable to detect seismic events with source radii of a few meters. Similar instrumentation has been facilitated in geothermal studies with similar targets and longer distances between injector and observation well, reporting micro-seismicity down to M_W -1.8 (Kwiatek et al., 2010).

The application of various processing techniques to the continuous seismic data recordings for the two-week time period considered here did not result in detection of any signal which can be associated with micro-seismic events with source size greater than a few meters. The most promising Type-F events (Section 2.3.3) do not reflect sufficiently strong signals and therefore it was not possible to determine their source location or to perform any further analysis. The waveforms which were identified with the low-frequency analysis cannot be considered as micro-seismicity either since they were detected mainly on only one sensor.

The most striking observation we derive from our analysis is that we clearly identified signals related to the outflow of CO_2/CH_4 in that seven out of the eight geophones do show a clear elevated noise level and complex signals during the reported onset. The fact that these signals are not occurring simultaneously leaves open several questions related to the actual processes triggering these signals.

Spectrograms provided information about the frequency of the signals contained in the data set. Most of the energy of the signals is contained in an interval up to 200 Hz. They displayed numerous spikes of uncertain origin, since they could be due to electrical failures or they might represent a signal of the CO_2 migration very close to each instrument. Noise analysis allowed the detection of a time period with a significant increase in the noise level at seven out of the eight geophones. This increase occurred at the reported time for the onset of the outflow and could reproduce the evolution of the CO_2/CH_4 along the observation well. STA/LTA analysis allowed us to focus on those parts of the data which partially fulfil the criteria to be considered as seismic events (F-Type). However, even the signals that could represent micro-seismicity are too weak to be located due to their small signal-to-noise ratios. Finally, the study of the low-frequency signals allowed the detection of certain waveforms which might be similar to long-period long-duration events. This analysis also revealed a considerable amount of waveforms with reasonable good signal-to-noise ratio which, however, are detected only at individual components of a single geophone. As a consequence, these signals cannot be classified to reflect induced micro-seismic events.

Due to the CO_2/CH_4 leakage reported along the observation well, the data from our borehole geophone array provide valuable hints about processes related to the migration of CO_2. However, given the temperature and pressure conditions, an elastic wave caused by drastic volume increase of CO_2 during its phase change from supercritical to gaseous would occur at depth levels around 1000 ± 100 m (Bohnhoff and Zoback, 2010; Bohnhoff et al., 2010b). Since in our case the geophone array was placed much deeper (1500-1640 m) and given the small energy of such signals the current location of the monitoring equipment would not allow to detect those signals although they might occur in the context of the outflow but far above the geophone array. This conclusion, however, is restricted to CO_2 while any similar behavior for the CH_4 would need to be evaluated in detail separately.

Acknowledgments

We acknowledge funding within the Helmholtz-Alberta Initiative (HAI), from the Helmholtz foundation in the framework of the Helmholtz Young Investigator Group ‘From microseismicity to large earthquakes‘ and from the EU-GEISER project. We thank Georg Dresen for his corrections and feedback.

Chapter 3

MSATSI: A MATLAB package for stress inversion combining solid classic methodology, a new simplified user-handling and a visualization tool[2]

For copyright reasons, this chapter was removed from the electronic version

[2] Published in *Seismological Research Letters (electronic seismologist)*, as Martínez-Garzón, P., Kwiatek, G., Ickrath, M., Bohnhoff, M. MSATSI: A MATLAB package for stress inversion combining solid classic methodology, a new simplified user-handling and a visualization tool. *Seism. Res Lett*., 85,4, doi: 10.1785/0220130189. Software package available to download at www.gfz-potsdam.de/msatsi.

Chapter 4

Stress tensor changes related to fluid injection at The Geysers Geothermal Field, California[3]

[3] Published in *Geophysical Research Letters*, as Martínez-Garzón, P., Bohnhoff, M., Kwiatek, G., Dresen, G. (2013). Stress tensor changes related to fluid injection at The Geysers Geothermal Field, California. *Geophys. Res. Lett.*, 40, 2596–2601, doi:10.1002/grl.50438.

Summary

Studying variations of the stress field in reservoirs caused by massive fluid injection is important towards an improved understanding of geomechanical processes involved. We report on spatio-temporal variations of the local stress tensor orientation at The Geysers geothermal field, California. We apply two stress inversion methods with detailed uncertainty assessments using a selection of events recorded between 2007 and 2012. Our results clearly indicate variations in the orientation of the principal stress axes for the reservoir as a whole showing a normal faulting regime at the reservoir depth between 2 and 3.7 km bounded by a strike-slip regime above and below. Analyzing the temporal evolution of the stress tensor orientation for a prominent seismicity cluster we observe a clear correlation of changes in orientation for $\sigma_{1\text{-}3}$ with the highest injection rates. These results suggest that temporal changes in the stress tensor orientation could contribute to characterize reservoirs during stimulation.

4.1 Introduction

Determining and studying crustal stress field orientations by inverting earthquake focal mechanisms has proven to be a robust and effective tool to study fault mechanics along plate boundaries (e.g. Hardebeck and Hauksson, 2001; Townend and Zoback, 2001) or even spatiotemporal rotations of principal stresses related to major earthquakes (e.g. Michael, 1987a; Bohnhoff et al., 2006). While stress rotations in most studies were in the order of 10-20° at best and thus close to the typical resolution limit of most datasets, recent M~9 megathrust earthquakes showed larger stress rotations (>20°) clearly associated with the mainshock ruptures (Hasegawa, 2011; Hardebeck, 2012).

Stress inversion techniques have also been applied to induced seismicity related to fluid injection into different types of reservoirs (Oppenheimer, 1986; Feng and Lees, 1998; Sasaki and Kaieda, 2002; Bohnhoff et al., 2004). These studies have mainly focused on spatial analyses around the geothermal area and particularly on the variations in stress field orientation with depth.

Spatio-temporal variations of the crustal stresses on the reservoir scale may be caused by massive fluid injections (Segall and Fitzgerald, 1998). Detection of potential stress changes is important towards an improved understanding of the associated geomechanical processes at reservoir depth. However, an accurate and reliable determination of injection-induced changes in stress orientation is not trivial and requires dense local seismic networks allowing determining reliable and accurate focal mechanism data. For this reason, such observations are still few and a description of the stress field response of a reservoir where massive fluid injection is performed remains not fully understood.

In this study we investigate potential spatial and temporal variations of the stress field orientation at The Geysers (TG) geothermal area, which provides the largest existing data set of induced seismicity with ~500.000 events since the beginning of operation in the 1960s. We also selected this dataset due to the great amount of local and regional seismic networks and stations available allowing calculating reliable focal mechanisms. First, we calculate the stress tensor orientation at different depths (local coordinate system) throughout TG. Second, we

investigate a prominent cluster of induced seismicity within the reservoir and relate the stress inversion results to injection rates of the two nearby wells. Our main goal is to determine whether changes in the stress field can contribute to detect (or even monitor) potential changes in a reservoir due to fluid injection.

4.2 Data and Method

We used the stress inversion software package SATSI developed by Hardebeck and Michael (2006). SATSI is a linearized inversion scheme which uses focal mechanisms (strike/dip direction/dip angle) as input data. It allows for a spatial and/or temporal subdivision of the focal mechanism data set into smaller subareas. Then, a damped inversion method is applied to resolve the stress field orientation for each subarea taking into account the adjacent subareas in order to smooth the solution. Therefore, only strong heterogeneities of the stress tensor are left, while other variations, e. g. artifacts arising from data subdivision are smoothed. When using SATSI, we selected only seismic events with more than 10 high-quality first-motion polarities available (weight 0 as defined in Klein, (2006)). Complementary, we also applied the MOTSI stress inversion method (Abers and Gephart, 2001). MOTSI is a non–linear scheme using first motion polarities as input data. Here, two nested grid searches are performed to identify the best-fitting stress orientations and focal mechanisms. The outer search tries a range of values for three stress directions and a relative stress magnitude $R = {\sigma_1 - \sigma_2}/{\sigma_1 - \sigma_3}$. Then, an inner grid search is conducted for each stress model and determines the focal mechanisms that best fit the first motions. To perform stress inversion with MOTSI we selected only events with a minimum of 20 high-quality first-motion polarities available (as recommended by Abers and Gephart, (2001) to ensure correct results with this method). Outputs of both methods are the orientations of the principal stresses, σ_1, σ_2, σ_3, as well as a relative stress magnitude.

To investigate the local stress tensor at TG we selected the hypocenter catalogue, fault plane solutions and first motion polarities as provided by Northern California Earthquake Data Center (NCEDC). We focus our study on the time period September 2007 - June 2012. The analyzed dataset contained approx. 16800 seismic events that occurred within TG area (Fig. 4.1). They were recorded by a local seismic network operated by Lawrence Berkeley National Laboratory (LBNL), and by several regional permanent stations deployed at different distances around TG. The hypocenters were determined with an absolute location method HYPOINVERSE (Klein, 2002). The local multi-layered 1D velocity model provided by Eberhart – Phillips and Oppenheimer (1984) is considered. Given the reasonably good azimuthal coverage of the seismic events and the large number of stations, the reported average horizontal location error for the NCEDC catalog calculated with HYPOINVERSE is 200 m and the vertical location error is 300 m.

In a first step we searched for potential depth-dependent variations of the stress field orientation (Fig. 4.2). For this part we selected seismic events with their epicenters distributed over the whole reservoir and sorted them according to the increasing depth. We performed a stress inversion of focal mechanisms using SATSI and a subset of first (shallowest) 150 events. Then, we moved by 100 events and repeated the inversion again using 150 events (i.e. the second subset contained 50 events overlapping with first one). This procedure (moving-depth window) was repeated until the last possible depth subset (containing the deepest 150

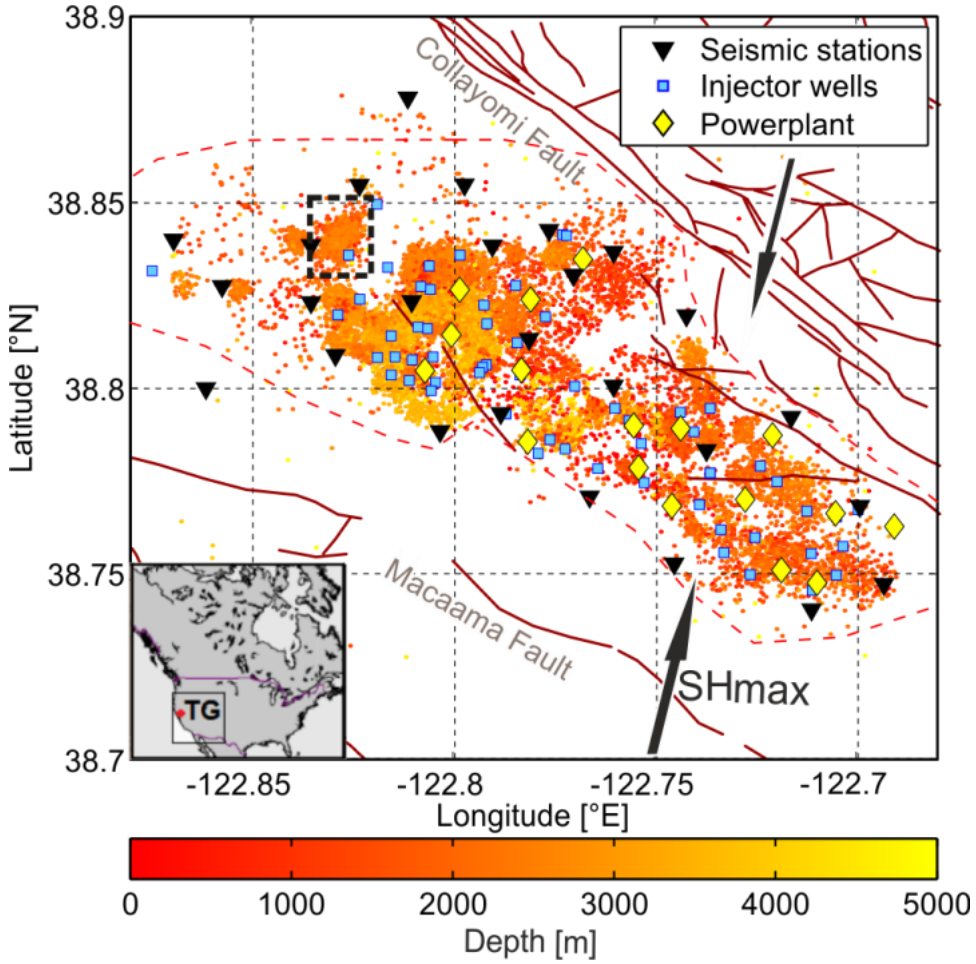

Figure 4.1: Spatial distribution of seismic events at The Geysers (M > 1) from September 2007 to July 2012 (Data from NCEDC catalog). Hypocentral depth is color encoded. Selected cluster for temporal stress field variation analysis is surrounded with a black rectangle. Green triangles represent the local seismic network from LBNL. Yellow rhomb represent active powerplants, blue squares represent injection wells (not all wells from the field are plotted). Black arrows represent the direction of the regional stress field as described in Oppenheimer (1986) and Provost and Houston (2003). Bottom-left corner: Overview on the location of TG in North America.

events). A few selected depth subsets are shown in Fig. 4.2b+c, together with the corresponding results of stress inversion (Fig. 4.2a). For comparison we also performed separate stress inversions using MOTSI.

For the temporal analysis, we selected seismic data from a spatially-constrained seismicity cluster located in the north–western part of the reservoir (rectangle in Fig. 4.1). In the direct vicinity of the cluster there are two wells for fluid injecting. The first well is used as a demonstration site for an Enhanced Geothermal System (EGS); there, injection resumed in November 2007. At the second well, injections started on April 2010. Gross amount of fluid injected is remarkably lower than in the first well, although both follow the same seasonal tendency (gross amount of fluid injected during winter months is higher than in summer months). During these injections, 742 earthquakes occurred. Their magnitudes vary between

1.0 and 3.1, and the majority of them are located at depths between 2000 m and 3000 m. There is no first-order depth variation throughout the analyzed interval. If more than one possible focal mechanism was provided, we selected the one with the smallest misfit. The focal mechanism catalog includes a substantial variation in mechanisms allowing for a reliable estimation of stress field orientation. Sorting the events with time we formed subsets of 55 events and inverted moving windows with 10-event increments using the SATSI stress inversion. The number of events in one subset was selected to balance a tradeoff between the discrimination of different injection stages and the insurability of a certain variety of focal mechanisms. The required variety of focal mechanisms for each stress inversion was checked by inspection of the respective distribution of P and T axes.

Since we aimed at detecting relatively small variations in the stress field orientation that could be close to the resolution limit of the methods applied, we performed complete uncertainty assessments for both used inversion methods. For SATSI we used bootstrap resampling method. Each fault plane solution taken into inversion was selected randomly from the two nodal planes available (i.e. we do not have a preference for one of the two permitted fault planes). For MOTSI the uncertainties were estimated applying a Bayesian technique. All inversion results shown in the following sections provide the best solution as well as the 95% confidence interval (2σ).

4.3 Results

4.3.1 Depth-dependent stress field changes

Inverting subsets formed after hypocentral depth with the SATSI routine we find clear changes of the stress field orientation with depth (Fig. 4.2a). At shallower level (down to Z=1000 m) the σ_1 and σ_3 axes are oriented sub-horizontal corresponding to a strike–slip regime. Between Z=1000 m and Z=1900 m, the position of the σ_1 and σ_2 axes is undefined considering plunges, indicating a transtensional stress regime. Between Z=1900 m and Z=2500 m, the σ_1 and σ_2 axes stabilize and σ_1 becomes vertical indicating a WSW/ENE-extensional normal faulting regime. Further below and down to Z=3800 m changes to transtensional and normal faulting are repeated. Finally, at the deepest analyzed intervals Z=3800 m to Z=4100 m (below the geothermal reservoir) the σ_1 axis rotates back towards subhorizontal suggesting a strike-slip/transtensional regime as observed above the reservoir. As shown in Fig. 4.2b+c for six selected depth intervals, the epicentral distribution of the seismic events considered for stress inversion is approximately homogeneous throughout the reservoir down to Z=2600 m, while below this depth the hypocenters cluster in the central part of the reservoir delineating a circular structure (Boyle and Zoback, 2011). The deepest seismicity is observed in the central and western part of the reservoir (cf. two right-most depth intervals presented in Fig. 4.2). In all performed stress inversions the σ_3 axis is located sub-horizontal pointing to N105°E. The trend of σ_1 and σ_2 remains stable at N15E°. Only for the deepest part of the reservoir the trend of σ_1 and σ_2 seems to be slightly rotated clockwise by 15°. The results from MOTSI generally follow those from SATSI described before with σ_1 and σ_3 being sub-horizontally oriented in the shallower section. In contrast, the result for the

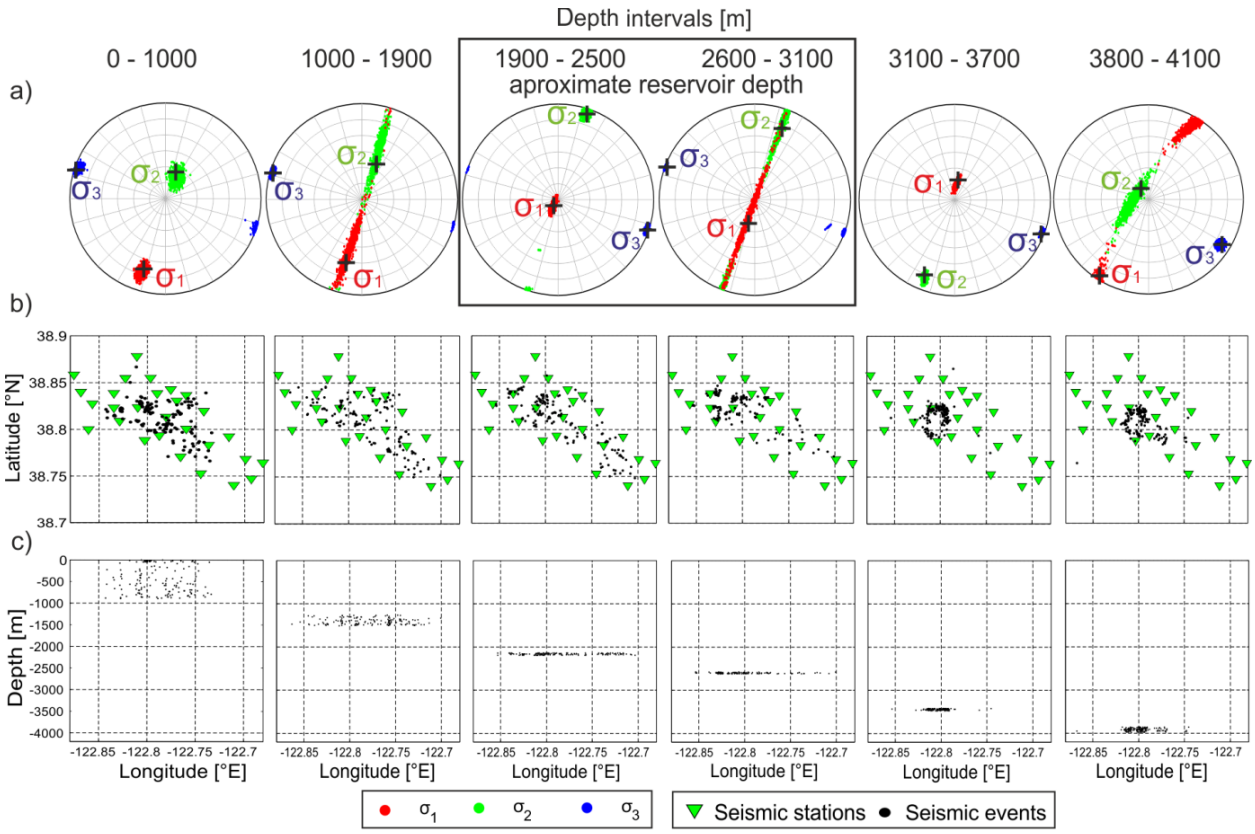

Figure 4.2 a) Example of stress inversion results (lower hemisphere projection) representative for the average stress orientation of the total of inversions performed in each depth interval (depths in local coordinate system). Red, green and blue colors correspond to σ_1, σ_2 and σ_3 axes, respectively. Dots represent sampled bootstrap points framing the 95% confidence intervals. Black crosses mark the best stress orientation obtained from inversion. b) Epicentral distribution of seismicity used in the corresponding inversion shown in a). Green triangles represent seismic network from LBNL. c) Seismic events from b) represented as a function of depth (note that as described in the text, several other stress inversions are performed, and therefore the seismic events plotted here are not representative of the total amount of seismicity but just for those event used in one particular inversion).

deeper section includes a substantially steeper direction for σ_1 reflecting a strong normal faulting component. However, since the confidence intervals for σ_1 and σ_2 are partly overlapping the results indicate a transtensional stress regime at larger depth. This is also confirmed by the low values for the relative stress magnitude *R* obtained from both inversion routines.

4.3.2 Time-dependent stress field changes

Analyzing the distribution of P and T axes of the 742 seismic events from the selected cluster suggests systematic variations during the investigated 5-year time period that can be easily correlated to injection rates (Fig. 4.3a). The plunges of P axes before and after time

periods with maximum injection rates are mainly distributed around the vertical direction. Remarkably, during the times of maximum flow rates P axes plunges decrease. We selected two time intervals framing the most prominent three peak injections (Intervals A and B, see black rectangles in Fig. 4.3b) and performed a detailed time-dependent stress inversion analysis as described above using subsets of the data. The results confirm a clear and statistically significant relation between injection rates and changes in stress field orientation for all three principal stress axes (Fig. 4.3c).

The change in plunge of σ_1 is similar for all three injections. Prior to an injection, the σ_1 axis is close to vertical. Inversion of faulting mechanisms from seismic events that occurred during peak-injection rates results in a progressive decrease in the plunge of σ_1. Moreover, including seismic events from the time period after the injection peak, the σ_1 axis rotates back towards close to its initial vertical position. The change in the plunge of σ_1 is significant and varies between 15° and 20°.

During interval A (peak-injection in December 2008), the plunges of the σ_2 and σ_3 axes also vary in accordance with injection rates. The plunge of σ_2 increases gradually and then during injection it slightly decreases by 15°. Similarly, the plunge of σ_3 gradually increases until the peak-injection and then decreases towards values from prior to the injection. For both σ_2 and σ_3 axes a counterclockwise and transient change in the axes trend is observed by about 25°. During interval B (peak injections in December 2010 and March 2011) the plunges of σ_1 and σ_2 show the most pronounced correlation with the gross amount of fluid injected. They show an inverse variation of approximately 20°. The plunge of σ_3 remains constant.

There are two minor but important differences between the two analyzed periods: First, the time interval A shows variations in both trend and plunge of the three principal axes, while for the interval B no remarkable changes in trend are observed but the plunge of the σ_1 and σ_2 axes varies significantly. Second, during interval A the change in stress orientation is synchronous with fluid injection, whereas in interval B the stress changes appear slightly delayed.

4.4 Discussion and conclusions

Due to the high rate of seismicity at The Geysers geothermal field and the exceptionally good quality of the seismic data available, this dataset provides a good opportunity to derive a better understanding on the effects of fluid injection on the stress state in the reservoir. In this study, stress inversion methods have been applied to two data subsets of induced seismicity. For the first case, the seismic events are distributed over the entire reservoir and we searched for potential variations of the stress tensor orientation with reservoir depth. For the second case, seismic events from a particular cluster of events were analyzed with regard to potential temporal variations in the orientation of the local stress field related to fluid injection in two wells. In both cases, the variations observed are significant considering 95% of confidence interval.

Studies about the regional stress field of Northern and Central California indicate that the stress field around TG is consistent with a strike–slip regime with the direction of maximum horizontal compression being oriented N26°E, and thus inclined by 55° with respect to the regional strike of the San Andreas Fault system (Provost and Houston, 2003; Hardebeck and Michael, 2004). No first-order spatial variations within TG have been reported. In general, our analysis shows a combined strike-slip/normal faulting regime consistent with the known regional stress field in Northern California.

Results from depth-dependent changes of the stress field orientation indicate a transition in the stress regime from strike slip above the reservoir to transtensional and normal at the reservoir level and finally transtensional and strike-slip below. This clear variation of the stress field orientation with depth is due to the flip of the plunges of the σ_1 and σ_2 axes, while their trend remains constant at N15°E. The changes observed in these axes are in accordance with changes in the value of the relative stress magnitude R, indicating that the magnitudes of σ_1 and σ_2 are less separated within the reservoir than outside.

The cause of the changes in stress orientations observed with depth across the TG reservoir is still not well understood. A potential explanation could be related to the presence of fluids in the vapor-saturated reservoir level. The role of fluids modifying the stress field and the faulting regime has been already pointed out in earlier studies (e.g. Hardebeck and Hauksson, 2001; Kato et al., 2011). In particular, Segall and Fitzgerald (1998) related a potential vertical variation of the stress state within the reservoir, above and below it to poroelastic effects related to reservoir depletion, i.e. on a time scale of decades. Specifically, the authors suggest that the horizontal stresses immediately above and below a reservoir are more compressive than within the reservoir. This is in qualitative agreement with the observed change in maximum compressive stress orientation from about horizontal above and below the reservoir to vertical within the reservoir. However, a quantitative assessment of interaction of stress rotation with variations in fluid pressure and depth does not yet exist for TG. Alternatively, the variations of the stress regimes with depth could also be related to the different geological formations within and above/below the reservoir. Particularly, the transition from graywacke sandstone to thermally altered graywacke sandstone where the temperature gradient is extremely high could affect the state of stress in the rocks, while a correlation between the average stress regime and the different geological layers remains imprecise due to the irregular high temperature layer at TG.

Although one of the assumptions for the inversion of fault plane solutions to determine the stress field orientation is a homogeneous stress field within the volume considered by the individual focal mechanism hypocenters (Michael, 1987), we believe that the stress field at TG might have local spatial variations due to different injection and production sites and schedules. For this reason, the stress field orientations calculated in this part of the study provides an average of the expected different local stress field orientations throughout TG.

In the second part of the study we analyzed potential temporal variations of the stress field orientation focusing on one particular spatially well-constrained seismicity cluster at the northwest of TG. Our results clearly show a systematic rotation of the principal stress axes during periods of massive fluid injection (Fig. 4.3). This observation for itself is remarkable in that it allows using an observed stress field orientation as a proxy for a change in the geomechanical status of a (geothermal) reservoir, e.g. during stimulation through massive fluid injection. More interestingly, this correlation of stress field rotation and peak-injection rates is observed in all cases analyzed so far. On the other hand, the variation is more evident in the first remarkable injection performed in the investigated area (corresponding to interval A). This observation suggests that the effect of the stress perturbation due to the fluid

injection might decrease over time with repeated injections. This might also be seen as an explanation for the delayed stress change during the second peak-injection period. It is well known that the injection of fluid increases the pore pressure of the rock matrix and according to the rock failure criteria it facilitates the slip of the rocks. However, a complete geomechanical explanation of the stress tensor changes observed in our study leaves open several questions. The existence of local faults at TG NE/SW oriented is consistent with the direction of regional maximum horizontal stress. In response to the three injections considered in our study, the σ_1 axes are moving towards shallower plunges, while the trend is changing by a lesser extent and being in SW direction in first order approximation. One potential explanation for the observed stress tensor perturbation, therefore, is that with the massive fluid injections, pre-existing local faults and fractures well-oriented for the regional stress would be reactivated or weakened for a short interval during high injection rates. A second possibility might be related to the fact that the analyzed cluster of seismicity is the result of one of the few EGS project performed at TG involving massive fluid injection and thereby aiming at increasing the permeability of the reservoir. Therefore, the active stimulation of the low-permeable reservoir may imply hydro-fracturing. It is then possible that during the time periods with higher injection rates of cold water, new small fractures were created and might have opened. These small fractures would then be oriented in the direction of S_{HMax} (NE - SW) and their activation could also perturb the stress field in the observed way.

Acknowledgements

We acknowledge funding within the Helmholtz-Alberta Initiative, from the Helmholtz foundation in the framework of the YIG ‘From microseismicity to large earthquakes‘ and from the EU-GEISER project. We acknowledge seismic data availability from North California Earthquake Data Centre and hydraulic parameters from Department of Conservation State of California. We thank Roland Gritto, Calpine Ltd. and Michèle Ickrath.

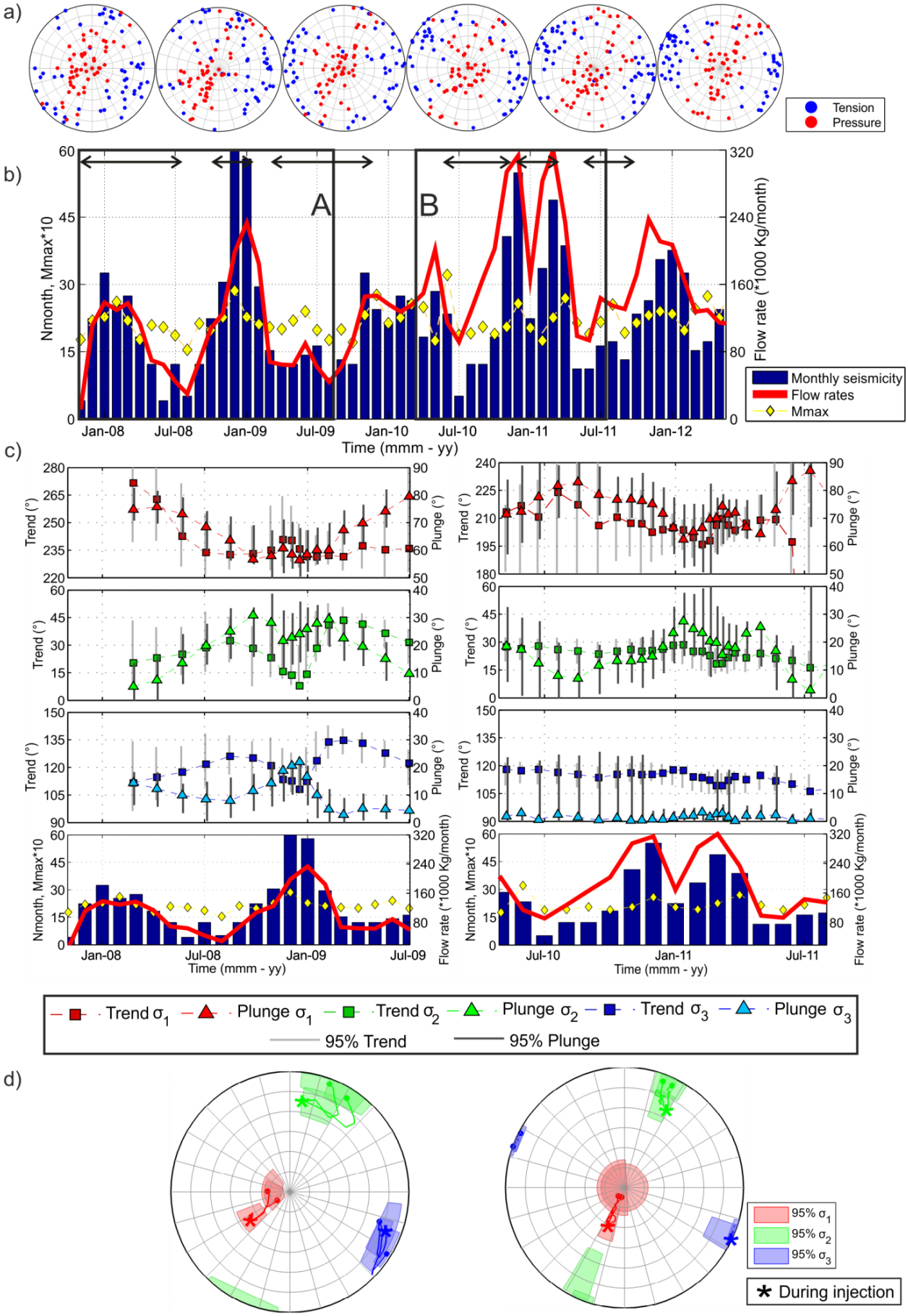
a)
Tension
Pressure
b)
A
B
Nmonth, Mmax*10
Flow rate (*1000 Kg/month)
Monthly seismicity
Flow rates
Mmax
Jan-08
Jul-08
Jan-09
Jul-09
Jan-10
Jul-10
Jan-11
Jul-11
Jan-12
Time (mmm - yy)
c)
Trend (°)
Plunge (°)
Trend σ1
Plunge σ1
Trend σ2
Plunge σ2
Trend σ3
Plunge σ3
95% Trend
95% Plunge
d)
95% σ1
95% σ2
95% σ3
During injection

Figure 4.3 a) Distribution of P and T axes of events used for stress inversions which contain seismic events from before, during and after the analyzed injections, respectively. The time frame covered in each plot is shown with the consecutive black horizontal arrows on b). b) Monthly seismicity rate from events from analyzed cluster. Injection rates are plotted as a sum from both considered wells (solid red line). The black rectangles frame the two analyzed time intervals (A and B). c) Results from the stress inversions performed during the time interval framed by black rectangles in b). Each symbol represents one stress inversions which time average corresponds to the X coordinate. From top to bottom: Trend (squares) and plunge (triangles) of σ_1 (first plot - red), σ_2 (second plot + green) and σ_3 (third plot - blue). For these three graphics, light and dark gray vertical bars represent 95% confidence intervals of trend and plunge, respectively. Next plot contains a zoom from b) corresponding to the analyzed time intervals. d) Variations of the stress field orientation during the selected time frames plotted in the lower hemisphere. Red: σ_1, Green: σ_2, Blue: σ_3. Solid lines: Trajectory described by the best solution. Semi-transparent region: 95% confidence interval corresponding to three inversions before, during and after the performed inversions.

Chapter 5

Spatiotemporal changes, faulting regimes and source-parameters of induced seismicity: A case study from The Geysers geothermal field[4]

[4] In preparation to *Journal of Geophysical Research* as: Martínez-Garzón, P., Kwiatek, G., Bohnhoff, M., Sone, H., Dresen G., Hartline C. Spatiotemporal changes, faulting regimes and source-parameters of induced seismicity: A case study from The Geysers geothermal field.

Summary

The spatiotemporal, kinematic and source characteristics of induced seismic events occurring during different fluid-injection rates are investigated to determine the predominant physical mechanisms responsible for induced seismicity and associated reservoir stimulation at The Geysers geothermal field in California. We analyze a relocated hypocenter catalog from a seismicity cluster located in the northwestern part of the geothermal field, where significant temporal variations of the stress tensor orientation have been previously observed to correlate with peak-flow rates of fluid injection.

We find that the stress tensor changes can be explained as an effect of the increased pore pressure and the corresponding increase in absolute horizontal stresses at reservoir depth. Utilizing high-precision hypocenters we observe that seismic events during peak-injection intervals tend to occur at greater distances from the injection point, preferentially trending north-east and parallel to the maximum horizontal stress. In contrast, at lower injection rates the seismicity tends to align in a SE-NW direction and suggests the presence of a local fault. Fault plane solutions show that during peak injection intervals, the relative contribution of strike-slip faulting mechanisms increases significantly and the seismic moment released by these strike-slip events is higher on average than that of normal faulting events. Furthermore, an increase in fluid injection rate is also noted to cause a decrease in *b* values. These previous observations may be related to the increase of pore pressure in the reservoir with fluid injection.

Our observations suggest that during pre- and post- peak-injection stages, the induced seismicity results from thermal fracturing of the reservoir rock. However, during peak injection intervals, pore pressure increase may have caused faulting and related seismicity.

5.1 Introduction

Mitigation of Induced Seismicity (IS) caused by fluid injection into geo-reservoirs has recently become a topic of increasing concern when considering efficient and sustainable energy production (e.g. Ellsworth, 2013). Reservoir stimulation is a common practice in geothermal energy projects as well as in production of conventional and unconventional hydrocarbons (e.g. shale gas). However, it involves the injection of large amounts of fluids frequently with the consequence of increased seismic activity and non-negligible seismic hazard in the surrounding areas (Dost and Haak, 2007; McGarr, 2014). An improved understanding of the physical processes governing IS and their relation to geomechanical reservoir conditions (e.g. stress, pore fluid pressure) and hydraulic parameters (e.g. injection rates) is of practical importance for reservoir operators and local communities (Majer et al., 2007; Evans et al., 2012).

The role of pore fluid pressure in reducing the principal effective stresses is well understood in the theory of poroelasticity (Wang, 2000). When fluid is injected into underground formations, the pore pressure increases. Terzaghi's Law (Terzaghi, 1923) states that the effective normal stress is reduced by the increase of pore pressure: $\Delta\sigma_n = S_n - \Delta p$, where $\Delta\sigma_n$ is the effective normal stress, S_n is the absolute normal stress and p is the pore

fluid pressure. Using a Mohr-Coulomb failure condition, failure is promoted by increasing the pore pressure, reducing the effective normal stresses and lowering the shear strength of the rock according to the formula:

$$\Delta\tau = H + \mu(S_n - \Delta p)\,, \qquad [5.1]$$

where τ is the shear strength, H is the cohesion strength of the rock and μ is the coefficient of friction.

However, the effect described by Terzhagui's Law is not the only factor that changes the effective stress in a reservoir. If we consider a laterally infinite, isotropic, porous, and linearly elastic reservoir that deforms uniaxially in the vertical direction, horizontal stresses are related to the vertical stress and pore pressure as follows (Lorenz et al., 1991):

$$S_{H,h} = \frac{\nu}{1-\nu} S_V + \alpha p \frac{1-2\nu}{1-\nu}\,, \qquad [5.2]$$

where $S_{H,h}$ and S_V are the horizontal and vertical stresses at reservoir depth, respectively, ν is Poisson's ratio, and α is Biot's coefficient. Assuming a constant vertical stress, the poroelastic change in horizontal stress from fluid pressure change may be expressed as (see Brown et al., 1994):

$$\Delta S_{H,h} = \alpha \frac{1-2\nu}{1-\nu} \Delta p\,. \qquad [5.3]$$

Poroelastic changes of the reservoir stress state are often used to explain the faulting and fracturing resulting from production activities in hydrocarbon and geothermal reservoirs (Segall et al., 1994; Segall and Fitzgerald, 1998).

Advanced IS waveform processing techniques allow monitoring of geomechanical processes occurring in the reservoir due to injection of fluids and also illuminate the fracture network. In particular, the double-difference relocation of IS hypocenters may reveal high-resolution patterns of the spatiotemporal distribution of seismicity (Waldhauser and Ellsworth, 2000). The method allows tracing potential migration of seismic events in the vicinity of the well, especially valuable during injection and after shut-in (e.g. Kwiatek et al., 2013, 2014a; Albaric et al., 2014). The spatio-temporal evolution of IS has been described using the triggering and back front of the seismicity (Shapiro et al., 2002; Parotidis et al., 2004). Furthermore, calculation of seismic source mechanisms followed by stress inversion provides important information on the orientation and relative magnitudes of principal stresses in a reservoir and the potential seismic hazard associated with stimulation (e.g. Terakawa et al., 2012). Combined analyses of microseismic and geomechanical data have been performed for Enhanced Geothermal Systems (EGS) e.g. at Soultz-sous-Forêts/France. At this site, Cuenot et al., (2006) found that most of the IS events likely represent normal faulting mechanisms, while the occurrence of strike-slip events was limited to the deepest part of the stimulated volume. Additional information on seismic faulting processes is provided by analysis of earthquake source parameters and statistical attributes of earthquake populations, for example Gutenberg-Richter magnitude-frequency distribution. Bachmann et al., (2012) reported a decrease of *b* values with distance from the injection well at the Deep Heat Mining project in Basel/Switzerland. Also, increase of the stress drop with distance from the injection well has been reported for the same site (Goertz-Allmann et al., 2011) and for the Berlin Geothermal field, El Salvador (Goertz-Allmann et al., 2011; Kwiatek et al., 2014a).

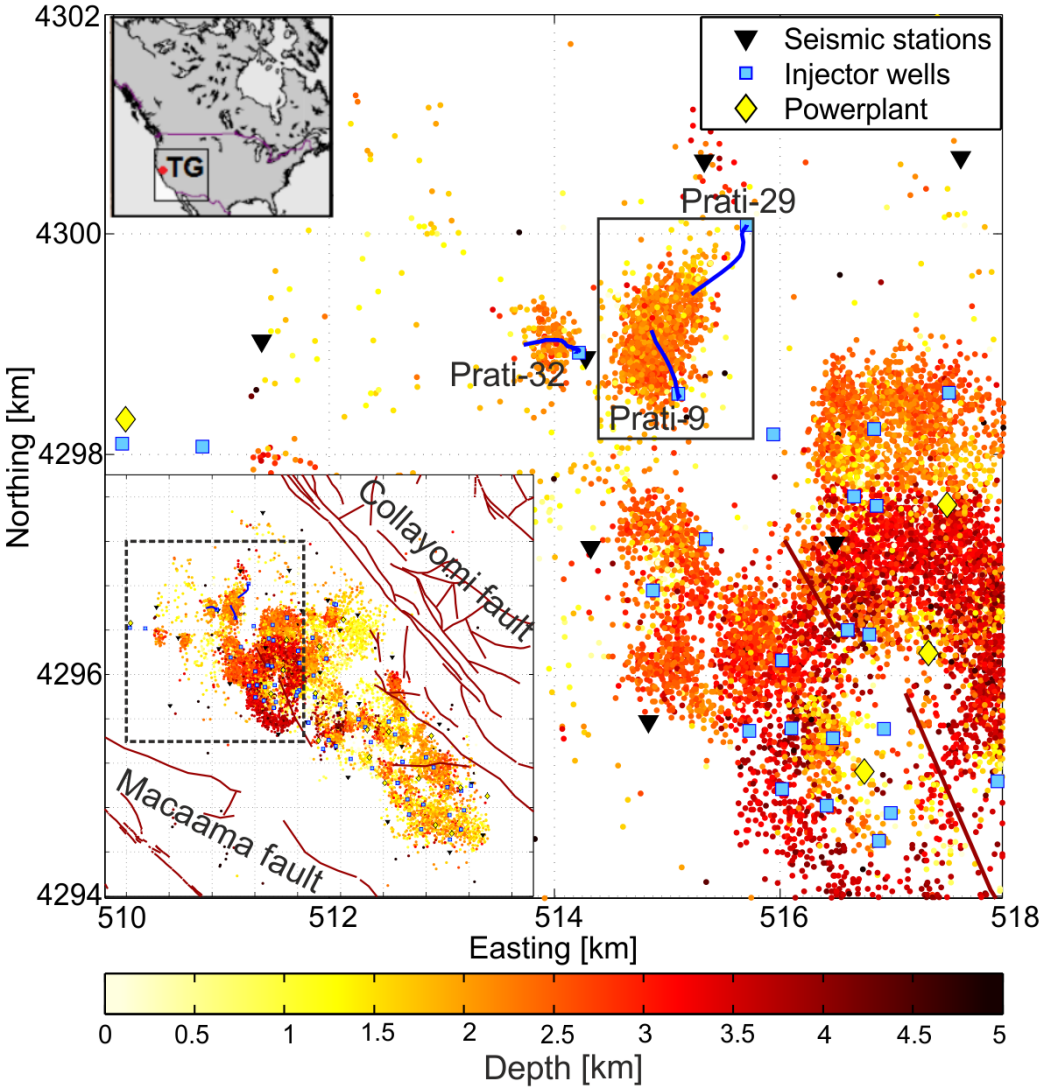

Figure 5.1 Map views of seismicity for The Geysers geothermal field between 2007 and 2012 (locations from NCEDC). Upper left: Location of TG in North America. Lower left: TG map view of the entire field. The dashed square is enlarged within the main map. Depth of the seismicity is color scaled. The trajectory of particular wells is plotted in blue. The analyzed cluster in this study appears within the black rectangle in the main figure. Brown lines are faults mapped by USGS.

The motivation for the analyses presented here originated from a previous study (Martínez-Garzón et al., 2013) that observed significant rotations in the orientation of principal stresses during peak-fluid injections at one seismic cluster on The Geysers geothermal field, California (Fig. 5.1). The stress rotations were interpreted to be caused either by reactivation of pre-existing well-oriented fractures or due to potential tensile opening of cracks. Here, we investigate the short-term effects of peak-injections on source characteristics of IS. In particular, we analyze variations in the faulting kinematics, spatio-temporal distribution of the relocated hypocenter catalog, temporal changes in *b* values, static stress drop and relative stress magnitudes from seismicity induced during two injection cycles at the same site as presented in Martínez-Garzón (2013). We then interpret the temporal fluctuations of the investigated parameters in relation to the injection-induced pore pressure changes surrounding the injection well.

5.2 The Geysers geothermal field

The Geysers (TG) geothermal field in Northern California, USA is the largest producing geothermal field in the world with approximately 330 active steam production wells and 60 active water injection wells (Brophy et al., 2010). This vapor-dominated reservoir has been producing since the 1960's, achieving maximum production in 1987. Since then, the reservoir production has been slowly declining (Gunasekera et al., 2003; Majer and Peterson, 2007). The decay was caused primarily by the decrease in reservoir pressure, along with some cooling of the reservoir (Mossop and Segall, 1997). To stabilize the reservoir pressure and preserve the steam production, large volumes of fluid have been injected with the construction of pipelines supplying treated waste water from Lake County since 1997 and Sonoma County since 2003 (Majer and Peterson, 2007; Majer et al., 2007). Associated with the reservoir pressure decline, GPS surveys indicate surface subsidence above the reservoir at a rate of approximately 5 cm/year between the years 1977-1996 (Mossop and Segall, 1997).

The Geysers geothermal field exists within a complex assemblage of Franciscan rocks (200 to 80 Ma) representing the ancient Farallon plate subduction complex. These Franciscan rocks consist primarily of graywacke, an impure mixture of silt, sand and rock fragments that were accreted to the North American continental margin resulting in a complex assemblage of intensely deformed, faulted and sheared metamorphic rocks. A West Coast transition from subduction to right-lateral strike-slip faulting began about 30 Ma as the spreading center between the Pacific Plate (to the west) and Farallon Plate (to the east) began to be subducted beneath the North American continent. With this transition, right-lateral strike-slip motion along the San Andreas Fault Zone (currently at ~24 mm/yr) and progressively lower rates of strike-slip motion along a series of more easterly right-lateral fault systems accommodate the relative motion between the Pacific Plate and North American Plate (DeCourten, 2008) . This right-lateral strike-slip motion of nearly parallel faults at progressively slower rates resulted in the transtensional tectonic environment between the (now inactive) Macaama and Collayomi faults associated with the development of The Geysers geothermal system. Here, approximately 1.1 Ma ago, a 760°C a granitic intrusion (the “Felsite”) resulted in recrystallization and fracturing of the Franciscan complex at depth. Magmatic and hydrothermal gases, reacting with deeply circulating ground water with dissolved silica, formed the reservoir caprock. More recently (~0.25 Ma) the 300°C liquid-dominated geothermal reservoir, resulted in the modern (pre-development) 240°C/3.5 MPa vapor-dominated Geysers geothermal reservoir with renewed heating by additional magmatic intrusions, some possibly as recent as 0.01 Ma (Hulen et al., 1997a, 1997b; Moore et al., 2000).

Within The Geysers, the local NNE-SSW trending maximum horizontal stress (S_{HMax}) is generally consistent with the regional geological structures (Oppenheimer, 1986), suggesting that the tectonic stress in the region dominates the local stress perturbations induced by geothermal activities. The low permeability, highly fractured reservoir rocks (greywacke) have a total porosity of about 1-2%. (Barker et al., 1992), reservoir temperatures of approximately 240°C at 2 km depth (García et al., 2012), and temperatures exceeding 350°C in the northwest Geysers at depths below ~2.75 km. (high-temperature zone, Jeanne et al., (2014)).

At TG, relatively cool water falls freely into the “injection” well resulting in a significant volume reduction as the reservoir steam condenses. This results in negative

pressure at the wellhead, quite a different situation than the active surface pumping at elevated wellhead pressures utilized in hydraulic fracturing.

Since a dense local seismic network was deployed in 2007, approximately 4000 seismic events per year with duration magnitudes M_d between 1.0-4.5 have been observed. The seismicity has been attributed to both water injection and steam production (Eberhart-Phillips and Oppenheimer, 1984; Oppenheimer, 1986; Foulger et al., 1997). As a result, different physical processes have been proposed to explain the occurrence of IS (Allis, 1982; Majer et al., 2007). Thermal fracturing of the hot reservoir rock due to local and rapid contraction during relatively cool water injection is considered to be a prominent mechanism producing microseismicity (Majer et al., 2007; Rutqvist et al., 2013). Additionally, changes in the pore pressure from both fluid injection or reservoir depletion may lead to perturbation of effective stresses in the reservoir resulting in seismic activity (e.g. Segall and Fitzgerald, 1998). Lastly, induced seismicity due to geochemical alteration of the rocks during cooling has also been proposed (Allis, 1982).

Progressing reservoir depletion has been proposed based on declining steam production in conjunction with subsidence at the surface (Gunasekera et al., 2003; Vasco et al., 2013). However, most of the NW part of the field was practically not exploited until 2007. To recharge the reservoir and reduce non-condensible gas concentrations, the previously-noted water-injection projects were established.

We analyzed the seismic data from the most prominent and spatially isolated cluster of induced seismicity in the NW part of TG (Fig. 5.1). The injection of water into Prati-9 started in November 2007. In April 2010, the injection well Prati-29 also started to inject water in the vicinity of the investigated area. Until December 2011, no production occurred through the nearest producer well, Prati-25. A clear correlation between the monthly seismicity rate and the volume of water injected from both wells was observed. The inversion of focal mechanisms from this cluster generally reported a normal faulting stress regime, and a significant (15°-20°) rotation of the principal stress axes directions towards lower plunges was found during peak-injections (Martínez-Garzón et al., 2013). The observed rotations of principal stresses were aligned with the maximum horizontal regional stress (Oppenheimer, 1986; Provost and Houston, 2003).

5.3 Data and methodology used

We initially used absolute hypocenters locations and focal mechanisms available from the catalogs of Northern California Earthquake Data Centre (NCEDC). Approximately 1150 seismic events with duration magnitude M_d ranging between 1.0 and 3.1 were detected and located during the time period between Sep 2007 and Jul 2012. Those hypocenters were determined using the HYPOINVERSE method (Klein, 2002) using a local 1-D gradient velocity model (Eberhart-Phillips and Oppenheimer, 1984). To locate the events, seismic data from both local and regional stations were used. Given the good azimuthal coverage of the seismic network and the large number of stations, the reported average horizontal and vertical location uncertainty was in the order of 200 m and 300 m, respectively.

For this cluster, 973 focal mechanisms were available in the NCEDC catalog. They were calculated with FPFIT (Reasemberg and Oppenheimer, 1985) using on average more than 30 first-motion polarities for each event. Monthly injection rates were provided by the

Department of Conservation State of California, and daily injection rates were provided by Calpine Corporation.

We first investigated potential differences of the seismicity patterns during different injection stages (before/during/after peak-injections). As the original catalog did not display any particular spatial features (cf. Fig. 5.1) we applied the double-difference earthquake relocation method to improve the precision of spatial offsets between the individual earthquake hypocenters (Waldhauser and Ellsworth, 2000). The same velocity model as for the absolute location catalog was here used. The double-difference method allowed us improving the precision of the relative hypocentral locations down to 40 m. A total number of 770 events were successfully relocated.

Second, we recalculated the focal mechanisms with the FPFIT software (Reasemberg and Oppenheimer, 1985) based on the relocated hypocenter dataset catalog and using all first motion polarities available. The new focal mechanism catalog was categorized into strike slip, normal and thrust events based on the relative orientation of P/T/B axes (i.e. which of the axis was closer to the vertical).

Then, we traced the evolution of various kinematic, spatial and source characteristics of IS with time to investigate their response to changes in injection rates:

1) Monthly distribution of the earthquake faulting types using all recalculated focal mechanisms.
2) Monthly cumulative seismic moment release, separately for the three faulting types. The moment magnitude was recalculated from coda duration magnitude using the M_W-M_d relation estimated for TG (Edwards and Douglas, 2013) and converted to seismic moment using a standard relationship (Hanks and Kanamori, 1979).
3) Temporal evolution of the Gutenberg-Richter *b* values. This was calculated using the goodness of fit method (Wiemer and Wyss, 2000) for different moving time windows containing 55, 65 and 75 events, respectively. The values for the moving windows were selected to maximize the number of events at fixed resolution to visualize potential changes during peak injection intervals.
4) Temporal evolution of the relative stress magnitude $R = \frac{\sigma_1 - \sigma_2}{\sigma_1 - \sigma_3}$ from the stress inversion technique. The stress inversion was performed using the MSATSI package (Martínez-Garzón et al., in press), which is an updated version of SATSI (Hardebeck and Michael, 2006). Stress inversion was performed using moving windows of 55 events with a step size of 10. It should be noted that *R* is the parameter with the largest uncertainty for the stress inversion technique irrespective of the performed 95% confidence interval uncertainty assessment.
5) Spatio-temporal changes in the average hypocentral and epicentral distance of the seismicity from the injection point of the well Prati-9. The data was subdivided in moving windows as described for the stress inversion. Here, we excluded those seismic events that were clearly related to the injection into the nearby well (Prati-29, see Fig. 5.2). The criteria to remove those events were based on time and proximity to the injection point from Prati-29 (see limiting line in Fig. 5.2). Note that since a temporal criteria is also used, events close to Prati-29 might be included if they occurred before the well began injection.
6) Evolution of the average static stress drop with time released by seismic events characterized by different faulting types. The static stress drops were calculated following a slightly modified spectral fitting method (Kwiatek et al., 2011, 2014a). The original 3-

	Stage	Time interval	Number of events
Cycle-1	Before	Apr 08 – Sep 08	24
	During	Oct 08 – Feb 09	59
	After	Mar 09 – Sep 09	30
Cycle-2	Before	Jun 10 – Oct 10	60
	During	Nov 10 – Apr 11	207
	After	May 11 – Oct 11	65

Table 5.1 Time intervals and number of events used in each stage of the analyzed cycles.

component waveforms from stations located <20 km from the seismicity were initially filtered using a 1Hz high-pass filter. Waveforms were analyzed with a window length of 0.40 s with additional 0.10 s period prior to either P or S wave onsets, respectively. The windows were smoothed using von Hann's taper. Far-field ground velocity spectra $\dot{u}(f)$ were calculated from three components of the sensor separately using the multi-taper method (Percival and Walden, 1993) and then combined using $\dot{u}(f)=\left[\dot{u}_V(f)^2+\dot{u}_{NS}(f)^2+\dot{u}_{EW}(f)^2\right]^{0.5}$ (e.g. Abercrombie, 1995). The observed ground velocity spectra were fitted using Boatwright's point-source model (Boatwright, 1978):

$$\dot{u}(f;M_0,f_C,Q_C)=\frac{R_C}{2\rho V_C^3 R}\frac{fM_0}{\left(1+(f/f_C)^4\right)^{0.5}}\exp\left(-\frac{\pi Rf}{Q_C V_C}\right) \qquad [5.4]$$

where R is the source-receiver distance, M_0 is the seismic moment, f_C is the corner frequency, Q_C is the quality factor and R_C is the P- or S- wave average radiation pattern correction coefficient. Following Boatwright and Boore (1982), we used R_P=0.52 and R_S=0.63 for P and S waves, respectively. V_C stands for the P- or S- wave velocity in the source area. We assumed V_P=4100 m/s and V_S=2441 m/s using V_P/V_S=1.68 (Gritto and Jarpe, 2014) and a density of ρ=2700 kg/m^3. The logarithm of the modelled ground P and S velocity spectra (Eq. (5.4)) was fit to the observed spectra of P and S phases and we inverted for (M_0, F_C, Q_C) separately for each station and phase. The optimization was performed using a grid-search technique followed by simplex refinement (cf. Kwiatek et al., 2011, 2014a). The seismic moment was calculated from P and S phases as a median value from all stations fulfilling the quality criteria. The source radius was calculated in a similar way using corner frequencies of P waves and assuming the circular source model (Madariaga, 1976) with scaling constant k=2.01 and a constant rupture velocity of V_R=0.9V_S. Finally, the static stress drop was calculated following Eshelby's formula (Eshelby, 1957):

$$\Delta\sigma_D=(7/16)M_0 r_0^{-3} \qquad [5.5]$$

In the following analysis, we focused on time intervals framing two particular injection cycles. Seismicity from each cycle was divided into three subsets (stages) preceding, containing and following the peak injection. Cycle-1 was composed of seismic activity framing the peak injection at well Prati-9 (the only well injecting fluid during this cycle), reaching a maximum flow rate of 0.24 Mm^3 per month. During Cycle-2 (May 10 – Oct 11) both wells Prati-9 and Prati-29 were active. Summing the injection volumes from both, a maximum injection rate of 0.32 Mm^3 per month was reached. Since water injection at TG follows a seasonal tendency, the peak injection usually occurred during the winter months.

Note that the analyzed cycles do not contain any periods of shut-in when the injection was stopped. The analyzed time intervals used in each stage are summarized in Table 5.1.

5.4 Results

The relocated hypocenter catalog and corresponding fault plane solutions allow identifying distinct spatial and temporal patterns of the seismicity not visible in the original catalog (Fig.5.2). Seismic events form an ellipsoid centered below the injection point of Prati-9. The long axis of the seismicity cluster is subparallel to the NNE/SSW orientation. There is a significantly smaller shallow sub-cluster of seismicity around the injection point of well Prati-29.

The most common faulting mechanism is normal faulting, while a substantial number of events also show strike-slip faulting. Many of the strike-slip events form an elongated but diffuse zone in the NNW-SSE direction with one of the nodal planes typically aligned in similar direction (Fig. 5.3). The NNW-SSE trending alignment of the strike-slip events forms an angle of ~40° with the orientation of S_{HMax}. Additionally, many normal faulting events are also located within this alignment, including the largest event from the analyzed cluster (M_L 3.1). Thrust events are sparse and evenly distributed throughout the whole cloud of IS. From the depth profile (Fig. 5.2b) we observe that most of the larger seismic events as well as most of the strike-slip and thrust events occurred at the bottom of the seismic cloud.

In the following, we focus on potential variations of faulting kinematics and source parameters in relation to peak injections during both injection cycles. The spatial distribution of the seismicity before, during and after peak injections reveals a distinct temporal evolution (Fig. 5.4). For Cycle-1 (Fig. 5.4a-c), prior to and after the peak injection the seismicity was located mainly towards the south of the injection point of Prati-9 around the mentioned NNW-SSE alignment. In contrast, during the peak injection we observe a significant increase in seismic events extending NNE and SSW of the injection point, aligned with S_{HMax} (Oppenheimer, 1986; Provost and Houston, 2003). Spatial evolution of seismicity during Cycle-2 follows an analogous behavior, although some seismicity also occurs close to the injection well Prati-29. We also observe that some of the larger strike-slip events occur at a greater distance from the injection point during the peak injection, especially during Cycle-1.

Fig. 5.5 shows ternary Frohlich diagrams (Frohlich, 1991; Bohnhoff et al., 2004) plotted for each stage to display the diversity of the fault plane solutions. The dominant faulting style is normal faulting, according to the average local stress field (Boyle and Zoback, 2011). However, a substantial part of the calculated focal mechanisms display a mixed mode of faulting. In particular, many events with mixed normal/strike-slip faulting behavior are observed, especially during peak injections. Still, note that many of the largest events from the analyzed cluster display pure strike-slip or a very large strike-slip components. Especially for Cycle-2, many of the normal faulting events have small magnitudes (M~1). During peak injections, the number of pure strike-slip (and slightly thrust faulting) events also increases. On average Cycle-1 displayed fewer events than Cycle-2 but with larger magnitudes. Cycle-2 contains more events with a mixed normal/strike-slip faulting style. However, one should keep in mind that during the peak-injection of Cycle-1, a larger number of small events were excluded in the relocation process.

For both the original and relocated catalogs, the total number of seismic events per month is well-correlated with the injection rate (Figs. 5.6a-b). During high injection rates an

increase in the number of normal faulting events is observed (Fig. 5.6b) but the number of strike-slip and thrust events is also seen to increase. More interestingly, the monthly percentage of faulting style shows that the relative contribution of normal faulting is decreasing by approximately 20% at the time of peak-injections, and this percentage is recovered in the strike-slip and the thrust faulting mechanisms (Fig. 5.6b). The number of events from each faulting type during different injection stages is summarized in Table 5.2. During Cycle-2, the number of thrust faulting events and strike-slip events increased by a similar proportion. However, during Cycle-1, the increase in strike-slip events is proportionally larger than the number of thrust events.

Within most of the analyzed time period, the monthly seismic moment release by normal faulting events is greater during the peak-injections (Fig. 5.6c). This can be attributed to abundant seismicity with normal faulting mechanisms, including several of relatively large magnitude. The cumulative seismic moment released by strike-slip events also increases during peak injection intervals, reaching nearly the seismic moment release of the normal faulting events with significantly fewer events. Therefore, this increase is related to the average higher magnitude of the strike-slip events. In July 2010 the seismic moment release by the normal faulting events reaches a maximum. This is mainly due to one M_L 3.1 normal faulting event occurring approximately two months after injection started at Prati-29.

During both analyzed cycles, a month-scale short-term response in b value decrease is observed coinciding with peak injections (Fig. 5.6d). In addition, a general trend towards decrease in *b*-values is observed for Cycle-2. These observations can be seen with each of the three moving windows utilized. In general, increasing the bin size would have the effect of diminishing the observation, as there would not be sufficient resolution to constrain the peak injection.

We also study variations of the relative stress magnitude *R* with time and injection history. In general, the variations in the *R* value correlate well with the injection rates, and therefore they reflect the changes of stress in the reservoir when increased volumes of water are injected. During peak injection intervals, the relative stress magnitude increased slightly (Fig. 5.7b). Although these changes are in the range of statistical uncertainty, they do correlate well with observed changes in principal stress orientation (Martínez-Garzón et al., 2013). Additionally, a steady decrease of *R* is observed over the duration of both injection cycles.

The average hypocentral and epicentral distance between the seismic events and the injection well Prati-9 also increased during peak injection (Fig. 5.7c). This increase is particularly clear for Cycle-1 (Table 5.3).

During the first peak-injection interval (Cycle-1) we observe a decrease in the average static stress drop of the normal faulting events, with the opposite trend visible for strike-slip events. (Fig. 5.7d). The average stress drop from thrust faulting events remains constant during Cycle-1. In contrast, during Cycle-2 no significant change in the average stress drop for any faulting type is observed.

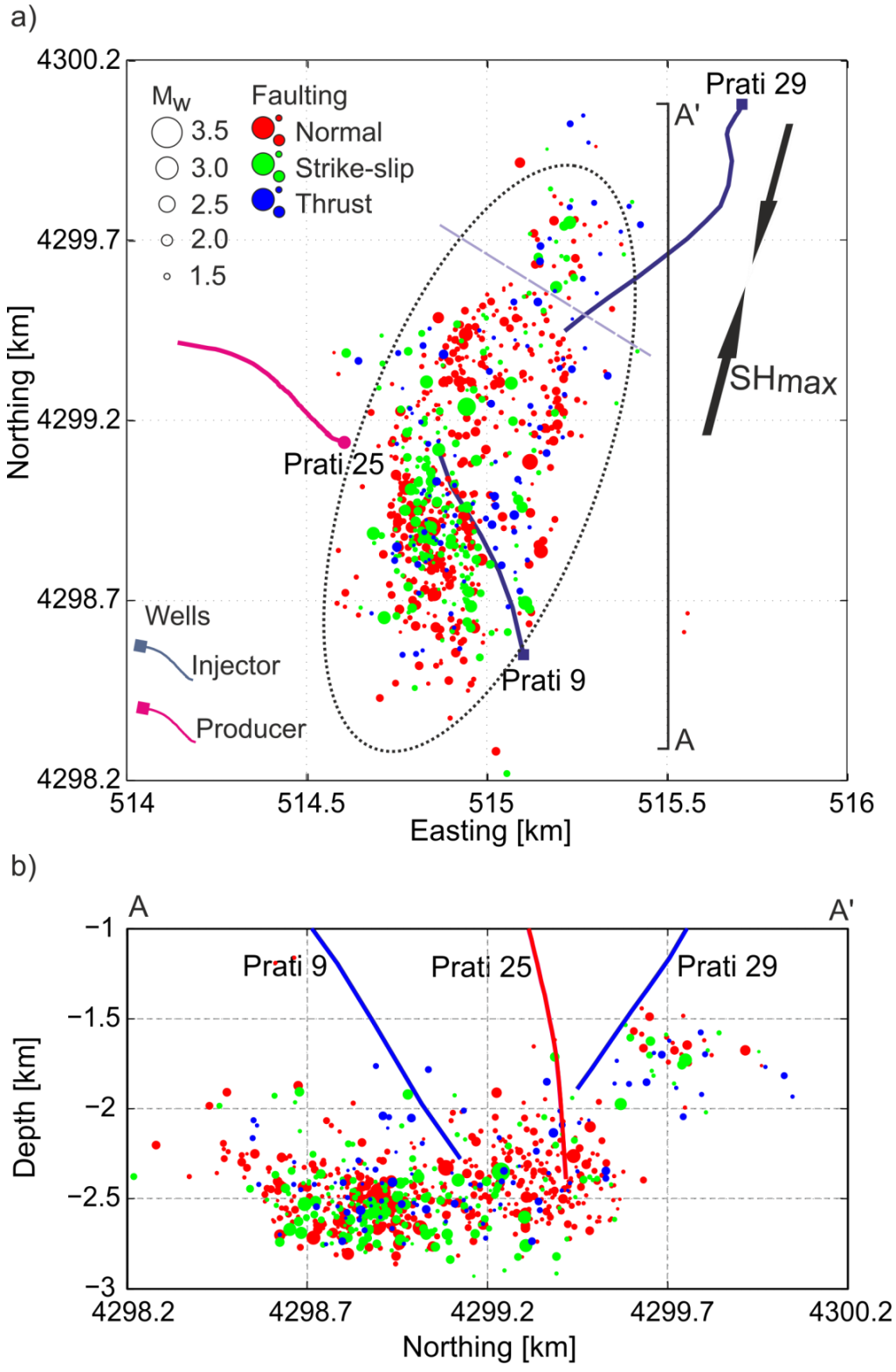

Figure 5.2 a) Map view of the relocated seismicity from the analyzed seismicity cluster at The Geysers geothermal field. Line A'-A marks the profile selected for the bottom plot. Violet dashed line marks the limit from distribution used in the calculation of distance from injection point. Note that a temporal condition is included, and some events NE of the line might be included. b) Depth section of the seismicity cluster along the profile A'-A. Easting and Northing coordinates are relative to the 10 N UTM zone.

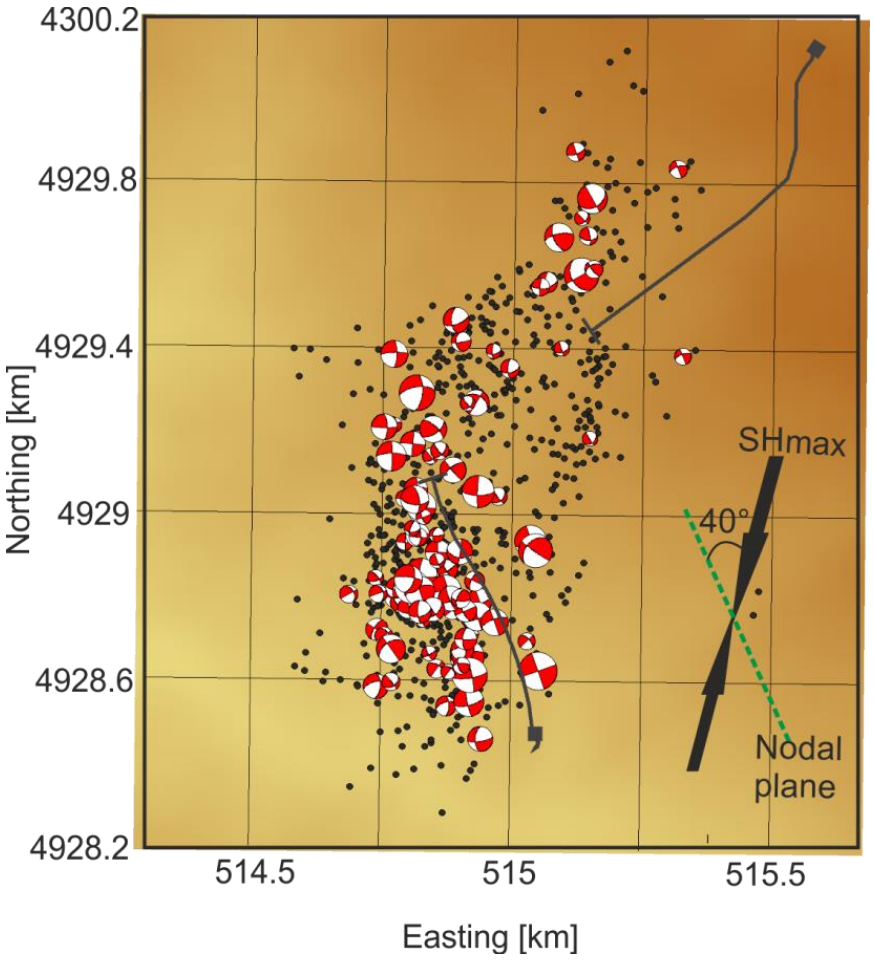

Figure 5.3 Map view of the nodal planes and the focal mechanisms of the 100 strike-slip seismic events with lowest misfit in the focal mechanism.

	Stage	Normal	Strike Slip	Thrust
Cycle-1	Before	10	6	4
	During	30	20	9
	After	15	13	2
Cycle-2	Before	36	16	8
	During	126	50	31
	After	35	25	5

Table 5.2 Number of strike-slip and thrust events during the different injection stages over the two cycles.

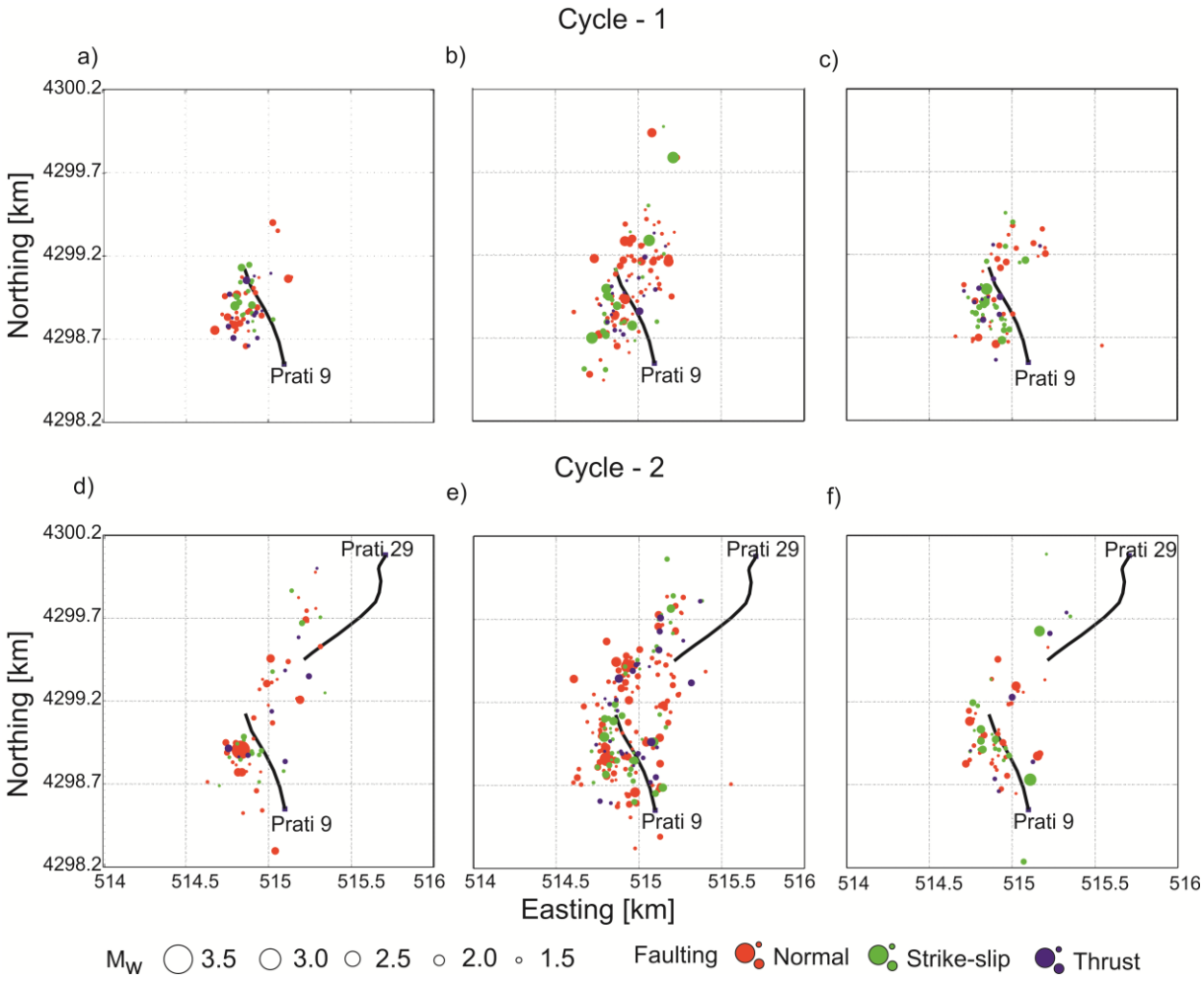

Figure 5.4 Snapshots of the spatial distribution of the seismicity during the different stages of both analyzed injection cycles. Symbol color is encoded by faulting style and size is scaled by magnitude.

	Stage	3D Distance [m]	2D Distance [m]
Cycle 1	Before	339	233
	During	477	374
	After	408	260
Cycle 2	Before	400	300
	During	450	360
	After	370	235

Table 5.3 Average hypocentral and epicentral distance from the injection point for each stage and cycle.

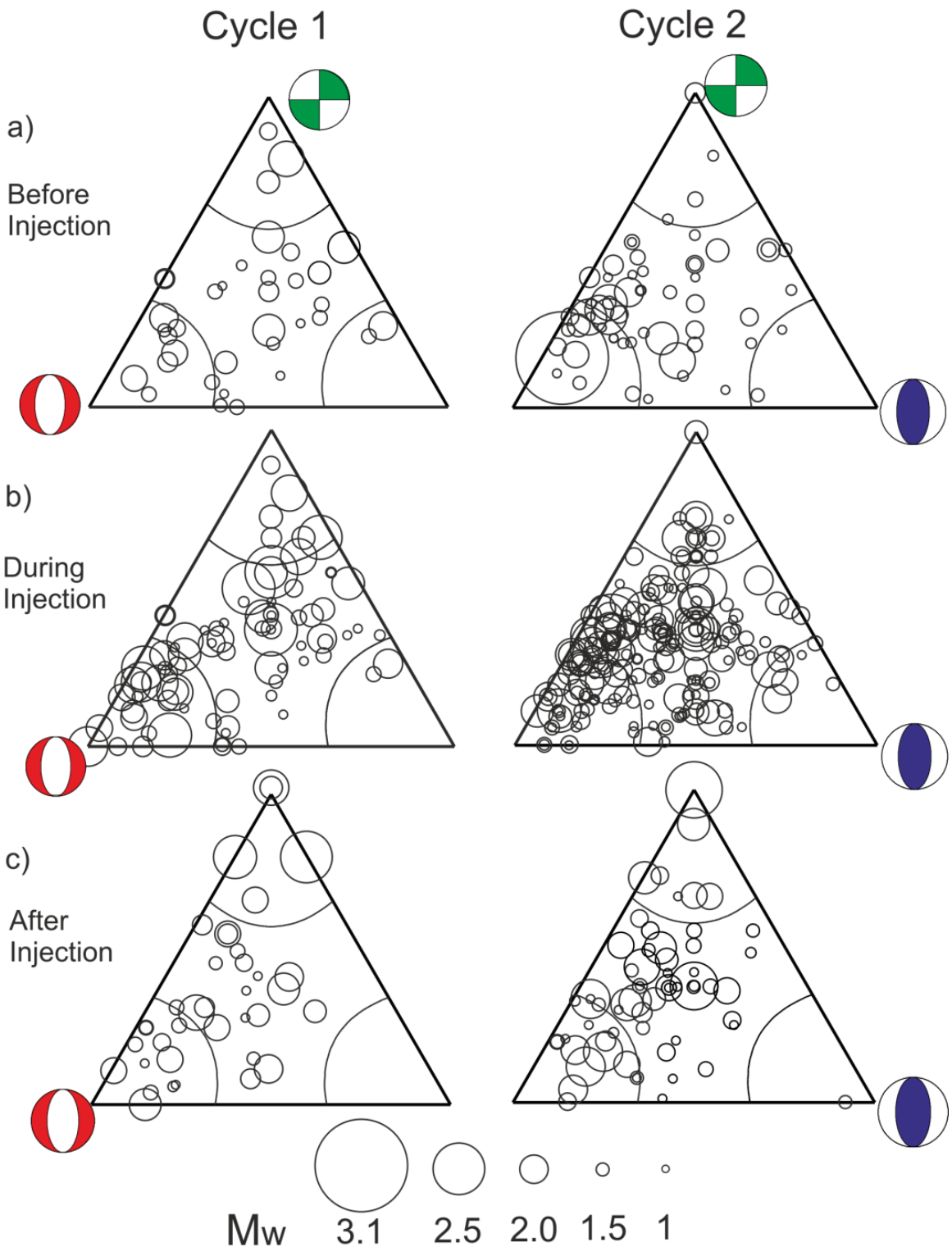

Figure 5.5 Ternary diagrams (Frohlich, 1991) for each of the stages of both analyzed injection cycles. Size is encoded with magnitudes. The angular lines mark 50° dip. Green: Strike-slip. Red: Normal faulting. Blue: Thrust faulting.

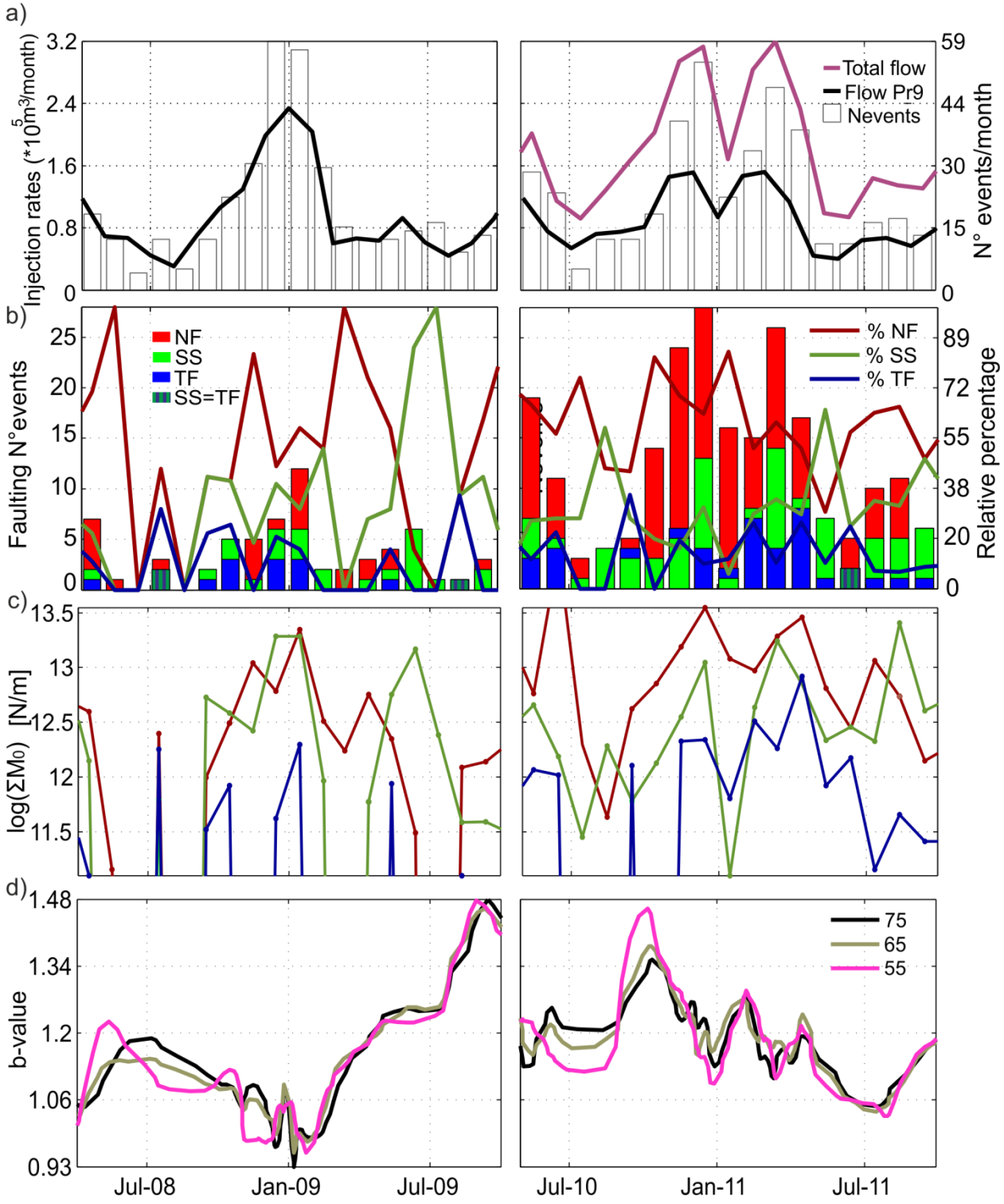

Figure 5.6 Temporal evolution of flow rates and seismic observation (Part I). Left column: Cycle-1. Right column: Cycle-2. a) Injection rates from Prati-9 and total injection rates. Monthly seismicity rate is indicated with white bars (original catalog). b) Monthly number of events of each faulting type (bars) and relative contribution of each faulting style with time (relocated catalog). c) Logarithm of the cumulative seismic moment for each faulting type. Color is encoded as in b). d) *b* value distribution for moving windows with a specific number of events.

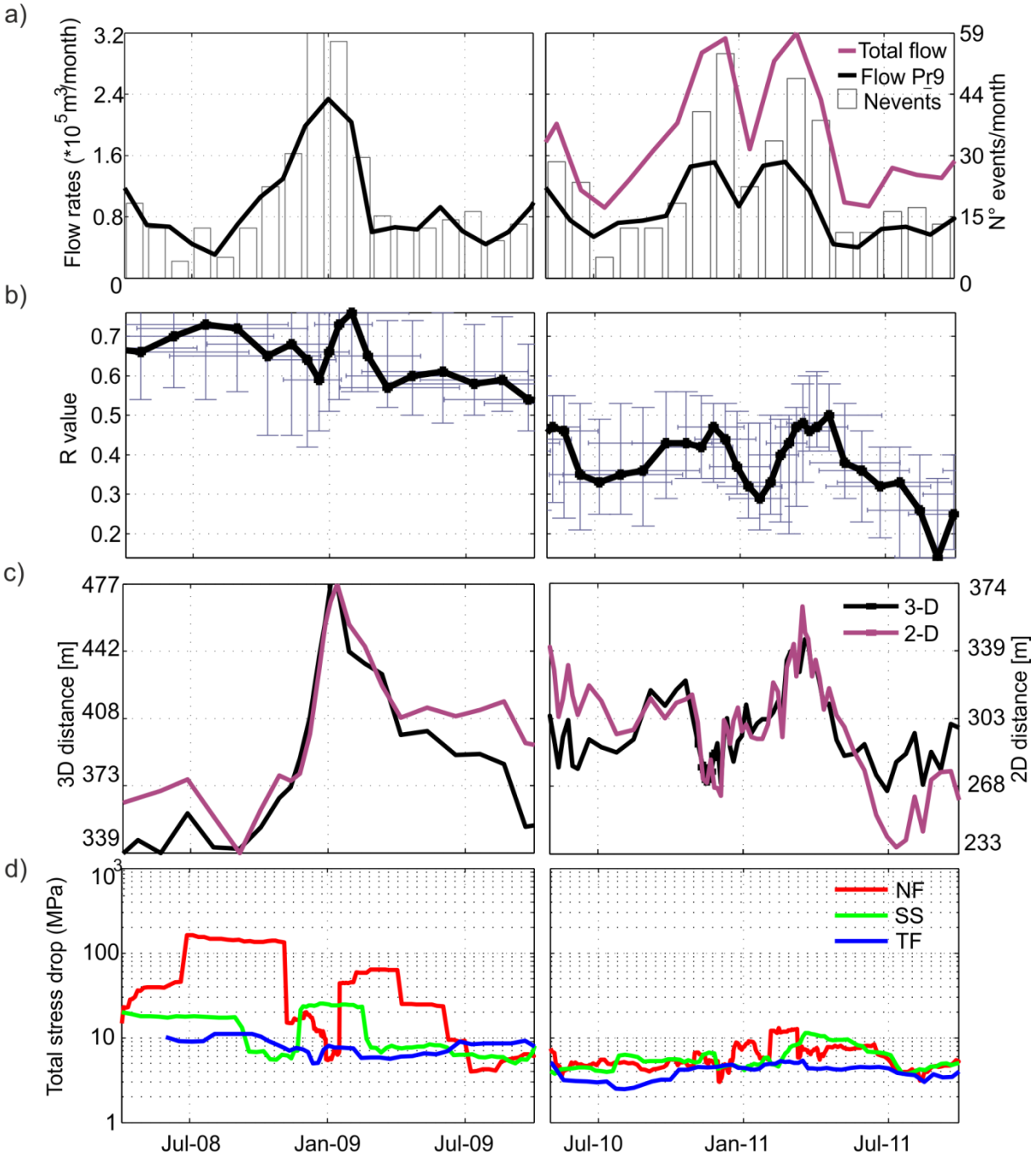

Figure 5.7: Evolution of flow rates and seismic observables with time (Part II). Left column: Cycle-1. Right column: Cycle-2. a) Flow rates from Prati-9 and total. Monthly seismicity rate is indicated with white bars (original catalogs). b) Relative stress magnitude R (black line). Vertical lines represent 95% confidence intervals. c) Hypocentral and epicentral distances from the well Prati-9. d) Time evolution of average static stress drop from each faulting style.

5.5 Discussion

The analysis of the selected seismicity cluster in the northwestern part of The Geysers geothermal field provides an excellent opportunity to gain additional insight in the mechanics governing induced seismicity associated with fluid injection. This relatively isolated system is especially interesting given the long injection history including several cycles of injection variation, the abundant seismic activity and the correlation between the injection rates and induced seismicity.

Recently, significant changes were observed in the stress field orientation during peaks of fluid injection into the reservoir (Martínez-Garzón et al., 2013). The current study aims to understand the physical mechanisms responsible for perturbation of the local stress field and changes in seismic response. The stress rotations were slightly more pronounced for the first peak injection (Cycle-1) at Prati-9. The observed changes in seismicity parameters described in the previous section follow a similar trend, being generally stronger during Cycle-1 than during Cycle-2. This is likely due to the fact that Cycle-1 was the first major injection in this area, while Cycle-2 occurred after several injection cycles. Other factors also might have played a role, e.g. additional injection at Prati-29. Also, the history of reservoir fracturing (Kaiser, 1953) may have influenced the analyzed characteristics of the seismicity. In difference with previous studies of fluid-induced seismicity (Baisch et al., 2002), no clear Kaiser Effect has been observed here.

5.5.1 Thermoelastic vs poroelastic stress perturbations

A potential explanation for observed changes of the seismic characteristics during peak injection intervals may be related to interactions of various physical mechanisms responsible for induced seismicity. Of the mechanisms proposed for TG, thermal effects are considered to play the most important role regardless of the injection stage (i.e. before/during/after peak injection). Thermal fracturing is effective in increasing the permeability of a reservoir, given that a network of secondary cracks oriented perpendicular to the main fracture direction is introduced (Ghassemi, 2012). Therefore, abundant low magnitude microseismicity is likely to be observed in response to thermal contraction close to the well (Fig. 5.8). Assuming that the heat diffuses isotropically, no preferential direction is required in principle for the thermal fractures. During peak injection intervals, the corresponding increase in pore pressure might be sufficient to reactivate faults within an existing fracture network. In general, thermal conductivity of the rock is smaller than the hydraulic diffusivity. Pore pressure diffuses rapidly with distance from the injection point and perturbs larger areas than those affected by thermal conduction. Additionally, numerical modelling of poroelastic stress changes from fluid injection indicates increased differential stress promoting failure dominantly parallel to the S_{HMax} direction (Schoenball et al., 2010). The poroelastic effect might be responsible for the predominant ellipsoidal shape of the seismicity cluster (Fig. 5.2). During peak injection intervals, thermal and pore pressure effects are expected to occur concurrently in the vicinity of the well. Since these two physical mechanisms are conceptually different (Fig. 5.8), changes in their relative contribution with time and distance could explain the different seismicity characteristics observed during different stages of the injection cycles.

Thermal fracturing caused by relatively cool fluid injection is assumed to be the primary mechanism responsible for IS at TG. This belief is supported by a series of modeling studies and research conducted by the field operator (Calpine Corporation) (e.g. Majer et al., 2007; Rutqvist et al., 2013). At the northwest part of TG, relatively cool water at approximately surface temperature (≈20-25°C) is injected into the reservoir. According to a pressure-temperature log performed in the well Prati-9 in Dec 2011, the water temperature at the bottom of the well was approximately 76°C. The injected water is heated rapidly by the surrounding rocks of the reservoir (240°C at the well Prati-9) (García et al., 2012). Considering these temperatures, the thermal stress change $\Delta\sigma_T$ directly at the wellbore can be estimated (Stephens and Voight, 1982):

$$\Delta\sigma_T = -\frac{\alpha_L E \Delta T}{1-\nu}, \qquad [5.6]$$

where α_L is the coefficient of linear thermal expansion of the reservoir rock, E is the Young modulus of the reservoir rock, ΔT is the difference in temperature between the reservoir rock and the water, and ν is the Poisson's ratio. If we use $\alpha_L = 1 \cdot 10^{-5} {}^{\circ}C^{-1}$ (Segall and Fitzgerald, 1998), $E = 12 \cdot 10^9 Pa, \nu = 0.25$ and the temperatures mentioned above, this results in an estimated thermal stress magnitude of approximately -26 MPa. At the depth of the seismicity cluster studied here, the temperature is expected to increase with a strong gradient, reaching 340°C only a few hundred meters deeper. Therefore, our estimation of the thermal stresses around the borehole is considered conservative. However, the thermal stress change attenuates rapidly with distance from the wellbore.

At TG, the pore pressure at reservoir depth is sub-hydrostatic. The height of the water column remains mostly within the reservoir limits, (less than 1 km below the surface). However, the increase in the injection rate closely correlates with the occurrence of IS suggesting that there is a mechanism by which pore pressure influences the seismic activity. Also, the ellipsoidal shape of the seismic cloud suggests that seismicity is induced by pore pressure changes at larger distance to the well.

The pore pressure associated with Prati-9 water injection is directly related to the height of the standing water column within the wellbore, which is in turn dependent upon the water injection rate. During a December 2011 "injectivity step-test", sustained injection rates of 2725 m^3/day (500 gpm), 4933 m^3/day (905 gpm) and 8231 m^3/day (1510 gpm) resulted in pressures of approximately 2.75 MPa (400 psi), 3.17 MPa (460 psi) and 3.79 MPa (550 psi), respectively for a tool suspended at a measured depth of 2682 m. With a total measured depth of 3053 m for Prati-9, this indicates total water column heights of approximately 668 m at 2725 m^3/day, 712 m at 4933 m^3/day and 779 m at 8231 m^3/day and corresponding total bottom hole pressures of approximately 6.20 MPa (899 psi), 6.6 MPa (958 psi) and 7.23 MPa (1048 psi), respectively.

In this calculation, only the volume of fluid injected through the well Prati-9 is taken into account. The obtained pore pressures always remain sub-hydrostatic and a pore pressure difference of about 1 MPa is estimated between peak injection and pre/post injection periods. This value is still relevant considering the minimum necessary pore pressures estimated to induced associated seismicity (Rothert and Shapiro, 2007). A maximum pore pressure of 7.2 MPa was estimated to be reached during Dec 2008 – Jan 2009 based on the injection rates from this well. During Cycle-2, additional fluid was injected from the Prati 29 well. Therefore the pore pressures we estimate here considering fluid injection rates from only Prati-9 are likely a lower estimate.

The conclusions of this study using observed seismicity are consistent with the synthetic geomechanical modelling of an Enhanced Geothermal System (EGS) system located approximately 1 km to the west (Rutqvist et al., 2013). The authors concluded that the EGS induced seismicity was primarily due to thermal contraction, with a secondary contribution from reservoir steam pressure changes.

In our study, the influence of reservoir depletion is not considered because no production was being performed during the analyzed times in the area. However, reservoir depletion is also expected to affect the seismicity at TG on larger time and spatial scales.

5.5.2 Hypocenter distribution and faulting mechanism

The spatial pattern of relocated seismicity (Figs. 5.2 and 5.4) reflects the regional stress field in that the first-order ellipsoidal shape of the seismic cloud has the long axis subparallel to S_{HMax}. This orientation is consistent with both the regional stress field and with the direction of preferred fault planes studied in another proximal seismicity cluster (Boyle and Zoback, 2011). This suggests that the regional stress field generally dominates the spatial distribution of the IS during the analyzed time period. The alignment of seismicity with S_{HMax} has also been observed in other geothermal projects, as in Soultz (Cuenot et al., 2006; Cornet et al., 2007) as well as in numerical modelling (Schoenball et al., 2010). The observed shape of the seismic cloud has been attributed either to increased differential stresses in this orientation during pore fluid pressure increase or to a preferred orientation of faults and fractures (anisotropic permeability of the reservoir).

The expansion of the seismicity away from the injection point during peak injection periods (Fig. 5.7c) may be explained by the pore pressure diffusion. This process will result in migration of an induced seismicity triggering front away from the injection well (Shapiro et al., 2002). The gradual evolution of the triggering front with time after shut-in has been observed in several field studies (Shapiro et al., 2002; Bachmann et al., 2011; Albaric et al., 2014). However, here we observed a short-term correlation between ongoing fluid injection and increase in distance that was not previously noted. Note that the seismicity collapses towards the injection point once the flow rate of the injected water has decreased (‘pulsation of the seismic cloud’). This behavior is conceptually different from that of the back front of the seismicity as described by *Parotidis et al.*, (2004). These authors stated that no seismic event is expected to occur close to the injection point once the injection has stopped. In this study, we are not expecting to observe a backfront since there is no shut-in. Our observations are in better agreement with an almost instantaneous or at least rapid poroelastic perturbation of the stress field caused by the injection.

The existence of NW-SE trending alignment of strike-slip/normal faulting events (and one of their nodal planes) suggests the existence of a fault forming an angle of ~40° with S_{HMax} that might have been reactivated (Figs. 5.2 and 5.3). The seismic events occurring within the potential fault might likely experience shear mode failure, given the optimal angle of the fault with respect to the local stress field. The seismicity within this alignment is clear before and after peak injection.

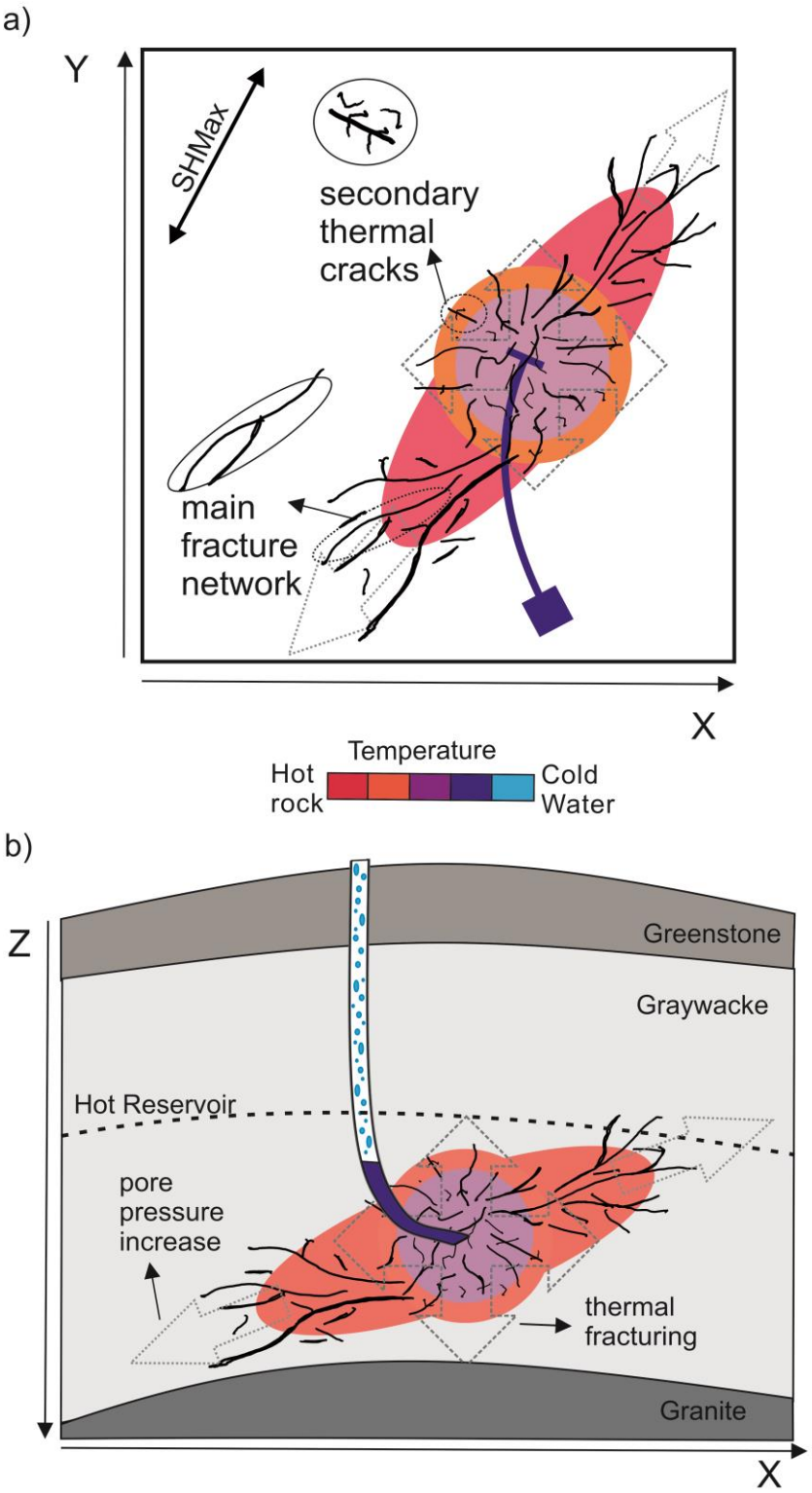

Figure 5.8 Schematic diagram of thermal fracturing and pore pressure increase at The Geysers. Colored areas are scaled by temperature. Dotted grey arrows represent the orientation of the seismicity closer to and away from the well a) Map view. Closer to the injection point (locally cooled), the fracture network is randomly oriented (spherical) given their thermal origin. As the pore pressure diffuses further from the well, the main fracture network is ellipsoidal and is aligned with S_{HMax}. b) Depth profile showing the ellipsoidal shape of the cloud. At TG, only a limited water column exists within the injection wells.

5.5.3 Relative stress magnitude

The small local increase observed during peak injection intervals is not straightforward to interpret. According to poroelasticity, these variations could be described as follows. Let the initial relative stress magnitude R_1 before the peak injection be:

$$R_1 = \frac{\sigma_1 - \sigma_2}{\sigma_1 - \sigma_3} = \frac{\Delta\sigma_{1-2}}{\Delta\sigma_{1-3}}. \quad [5.7]$$

During the peak injections, the pore pressure will increase. Accordingly, the magnitude of the horizontal stresses will increase according to Eq. (3). Assuming a normal faulting stress regime, the horizontal stresses are aligned with the σ_2 and σ_3 axis. Therefore, the relative stress magnitude during the peak injection R_2 can be expressed as:

$$R_2 = \frac{\sigma_1 - (\sigma_2 + C\Delta p)}{\sigma_1 - (\sigma_3 + C\Delta p)} = \frac{\Delta\sigma_{1-2} - C\Delta p}{\Delta\sigma_{1-3} - C\Delta p}, \quad [5.8]$$

where C is a constant defined as $C = \alpha\frac{1-2\nu}{1-\nu}$ with α being the Biot coefficient and ν the Poisson's ratio (cf. Eq. 3). Forming the ratio from Eqs. (5.7) and (5.8) we obtain:

$$\frac{R_1}{R_2} = \frac{\Delta\sigma_{1-2}}{\Delta\sigma_{1-3}}\frac{(\Delta\sigma_{1-3} - C\Delta p)}{(\Delta\sigma_{1-2} - C\Delta p)} = \frac{\Delta\sigma_{1-2}\Delta\sigma_{1-3} - \Delta\sigma_{1-2}C\Delta p}{\Delta\sigma_{1-2}\Delta\sigma_{1-3} - \Delta\sigma_{1-3}C\Delta p}. \quad [5.9]$$

In this case, by definition $C\Delta P$ is increasing during injection. Then:

$$\sigma_{1-3}C\Delta P > \sigma_{1-2}C\Delta P \quad [5.10]$$

And the ratio becomes:

$$\frac{R_1}{R_2} > 1 \rightarrow R_1 > R_2. \quad [5.11]$$

Therefore, assuming a normal faulting stress regime, the R value would be expected to decrease during the peak injections. However, this is somehow opposite to our observations, which report a local small increase in the R values during peak injections. Interestingly, when one repeats an analogous procedure assuming a strike-slip regime, an increase in the R value during peak-injections is obtained. Given our previous observations concerning the relative increase in the contribution of the strike-slip events during peak injections, the increase in the R value might be reflecting the influence that the strike-slip events have in the stress inversion.

5.5.4 *b* values and stress drop

The observed decrease in *b* values during peak-injections may be interpreted as the result of increased contribution by strike-slip and thrust faulting events. *Schorlemmer et al.*

(2005) observed from the complete seismic catalog of California that *b* values were related to the faulting regime, with the largest *b* values expected for normal faulting, intermediate *b* values for strike-slip faulting and the lowest *b* values expected for thrust faulting. The decreased observed in the b value at the time of the peak injections is in agreement with these observations, given that at these times the relative contribution of strike-slip and thrust faulting events is increasing. Our findings cannot be directly compared to the results found for the Basel Deep Heat Mining Project, where a decrease in the *b* values occurred between the injection period and the post-injection period (Bachmann et al., 2011). The main difference between these studies is the lack of a shut-in period at TG. A second difference might be related to our observed change in proportion of each faulting mechanism. At Basel, the reported stress regime is strike-slip (Terakawa et al., 2012). To our knowledge, no significant change in faulting mechanism during peak injection intervals was reported.

Additionally, the decrease found in the *b* value during peak injections may be attributed to the increase in the horizontal stresses resulting from the pore pressure increase (Lorenz et al., 1991). To assess this, we assume that *b* values are inversely proportional to the differential stress ($b \propto 1/(\sigma_1 - \sigma_3)$). According to the relative distribution of stress depending on the position from the injection well with respect to the horizontal stresses, the differential stress is larger in the direction of S_{HMax} (Schoenball et al., 2010). Since during peak-injections the seismicity mainly occurs aligned within this direction, the differential stress will increase and the *b* values should decrease according to our observations. Given that the decrease in *b* values occurred during the pore fluid pressure increase in the reservoir, our results are in agreement with those of Bachmann et al., (2012), where the decrease of *b* values with distance from the well was attributed to the decrease in the pore fluid pressure. In our case, lower b values are occurring during peak-injections when the seismicity is occurring on average further away from the well. However, the assumed hypothesis and the applied methodologies from both studies are quite different, as their study assumed a hydraulically isotropic medium while we assumed a laterally infinite reservoir.

The observed small variations of the stress drop observed in the normal faulting and strike-slip events are not clear enough to allow conclusions. Additionally, the fact that they only occur during Cycle-1 complicates their interpretation. Results showing that the stress drop associated with thrust faulting is larger than that associated with normal faulting have been reported for a number of previous studies (e.g. Cocco and Rovelli, 1989; McGarr and Fletcher, 2002), but it is not always seen. Here, the higher stress drops for strike-slip faulting may reflect the increase in the differential stresses during peak injection intervals.

5.5.5 Stress magnitudes and pore pressure

To estimate effective stress magnitudes at reservoir depth, we used the calculated pore pressures and information from a density log. Assuming an average density of the greywacke reservoir rock of 2700 kg/m^3, the vertical stress is calculated from:

$$S_V = \rho_g g z \qquad [5.12]$$

where ρ_g is the density of the graywacke, g is the acceleration of gravity and z is the average depth. Assuming a normal faulting stress regime, a value of $S_V = S_1 = 78MPa$ is obtained.

Then, we assume that maximum stresses in the reservoir are limited by critically stressed faults near failure as we observe IS occurring with small pore pressure perturbations (~1 MPa) in comparison to the overburden stress. For the case of frictional equilibrium of optimally oriented faults the relationship is (Jaeger and Cook, 1971):

$$\frac{S_V - p}{S_h - p} = \left[\sqrt{\mu^2 + 1} + \mu\right]^2 \qquad [5.13]$$

where μ is the coefficient of friction for pre-existing faults. Assuming a value of $\mu = 0.85$ (Byerlee, 1978), and a minimum pore pressure of $p = 6MPa$ for the periods before and after peak injections, a value of $S_h = 21MPa$ for the time period before the peak injection is obtained.

To estimate the intermediate stress, S_H, we use the stress ratio R (Plenefisch and Bonjer, 1997). An average *R* value for Cycle-1 is $R = 0.65$ and the intermediate stress can be estimated from:

$$R = \frac{\sigma_1 - \sigma_2}{\sigma_1 - \sigma_3}, \qquad [5.14]$$

leading to $S_H = 41MPa$ before peak injection. Therefore, the initial effective stress magnitudes $S_h = 21MPa$ for the time period before the peak injection (assuming a pore pressure of about 6 MPa) are about: $\sigma_V = 72MPa, \sigma_H = 35MPa, \sigma_h = 15MPa$.

During the first peak injection, the difference in pore pressure is approximately $\Delta p = 1MPa$. Therefore, the corresponding effective stresses would be: $\sigma_V = 71MPa, \sigma_H = 35MPa, \sigma_h = 15MPa$. However, the horizontal stresses in radial direction from the injection well will increase during the peak injection (Eq. 5.3). Assuming a Poisson's ratio of $\nu = 0.25$ and a maximum Biot coefficient of $\alpha = 1$, we obtain a maximum increase of the horizontal stresses of $\Delta S_{H,h} = 0.7MPa$. Therefore, during peak injections assuming a predominant normal faulting regime, the stresses would have been modified to $\sigma_V = 71MPa, \sigma_H = 35.7MPa, \sigma_h = 15.7MPa$. Here we assumed S_V to be constant and no lateral strain.

Note that, by taking into account the value of the thermal stresses estimated at the wellbore, the effective stresses in proximity might be reduced such that σ_h would exceed reported tensile strength for greywacke sandstone (estimated in -8-12 MPa, *Holub et al.*, 2009). Therefore, it is possible that tensile failure could occur very close to the wellbore.

5.5.6 Superimposed effects of thermal fracturing and pore pressure increase

Before and after the peak injections, the type of faulting is predominantly normal and the seismicity is mainly located around the injection point and aligned with the direction NNW-SSE. When cool water interacts with the hot reservoir rock during injection, contraction of the rock is expected. As with reservoir depletion (Segall and Fitzgerald, 1998), volumetric contraction of the reservoir rock should reduce the horizontal stresses at least locally. This can be illustrated schematically in a Mohr circle diagram. Assuming a normal faulting stress regime, a reduction of the intermediate and minimum stress would result in a larger differential stress and a stress state closer to the failure envelope (Fig. 5.9a). The thermal effect is likely to occur near the well, but not at larger distances, given that thermal conductivity is small compared to hydraulic diffusivity.

The pore pressure increase during peak fluid injection intervals may be responsible for the increase in seismic activity and its occurrence further away from the injection well. As a consequence of the pore pressure increase, the effective principal stresses would decrease and the Mohr circle would be shifted to the left and towards the failure envelope (Fig. 5.9b). This effect alone would not create a rotation of the stress tensor that was observed previously (Martínez-Garzón et al., 2013). The combined effect of poroelastic stress and pore pressure change from fluid injection results in a reduction of horizontal effective stresses. Assuming isotropic expansion of the pore pressure away from the well, radial horizontal effective stress components will experience less reduction than tangential horizontal effective stress components (Altmann et al., 2014). In a normal faulting environment, this results in larger differential stresses along the S_{HMax} direction (Schoenball et al., 2010; Altmann et al., 2014).

5.6 Conclusions

In this analysis we studied the seismicity associated with two fluid injection cycles performed in the northwestern part of The Geysers geothermal field, California. A total of 770 induced seismic events were relocated, followed by the recalculation of their fault plane solutions and an assessment of their source characteristics. Both of the analyzed injection cycles included a peak injection interval with extended periods of moderate injection both preceding and following this peak. The temporal evolution of the spatial distribution of the seismicity, faulting kinematics, *b* values, relative stress magnitude, distance from the injection point and stress drop show substantial changes during the times of peak-fluid injection with respect to periods preceding and following the peak injection.

The spatiotemporal distribution of focal mechanisms has suggested that during the peak injection, the pore fluid pressure in the reservoir increased and resulted in increased horizontal stresses at reservoir depth. Therefore, the pore pressure front extended away from the well, with induced seismicity aligned with S_{HMax} occurring at greater distances from the well. During the peak injection intervals the number of normal faulting events substantially increased and the number of strike-slip and thrust faulting events increased more than expected. The peak injection resulted in the extension of the fracture network. This analysis also detected the presence of a seismicity alignment within the cluster which could represent a local fault favorably oriented with respect to the regional stress field.

A decrease in *b* values simultaneous with the increase in relative amount of strike-slip and thrust events at peak injection rates has been observed. These observations, combined with the analysis of the relative stress magnitude, suggest that during peak injections an increase in the reservoir in-situ horizontal stresses occurs.

The observed changes in the seismic properties confirm the idea that different physical mechanisms are playing a more relevant role during the different injection stages. In particular, it is proposed that although thermal fracturing of the reservoir might be predominant mechanism regardless of the injection stage, during the peak-fluid injections, the pore pressure increase also contributes to seismicity beyond the influence of thermal fracturing. We estimated the change induced by thermal stress at the wellbore to be around 26 MPa, while variations in the pore pressure are approximately 1 MPa. While this value is small compared to thermal stresses, this effect has a significant effect on the seismicity and thus poroelastic effects cannot be neglected. Using the data from the stress inversion and the pore pressure calculation, an estimation of the state of stress before and during the peak-fluid injection was provided.

Acknowledgments

We acknowledge funding within the Helmholtz-Alberta Initiative and from the Helmholtz Association in the framework of the Young Investigators Group ‘From microseismicity to large earthquakes‘. We thank the Northern California Earthquake Data Center and the Lawrence Berkeley National Laboratory for providing the seismic data, and the Department of Conservation State of California supplying us with the hydraulic parameter data. We thank Calpine Ltd. for high-resolution hydraulic data and additional relevant information related to The Geysers geothermal field. We thank Luca Urpi for early discussions and Martin Schoenball for providing a ternary plot code.

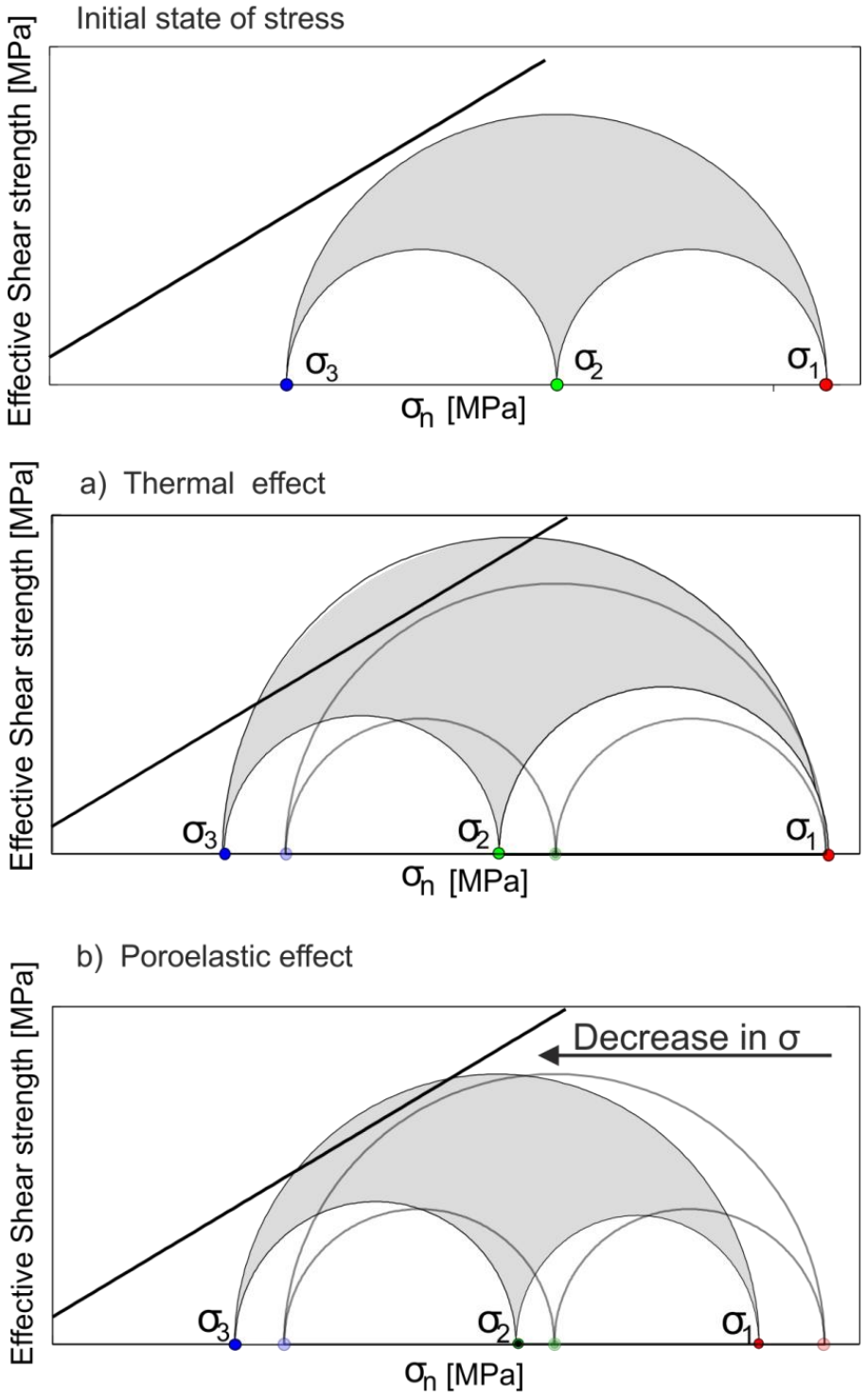

Figure 5.9 Conceptual illustration of the variation of the principal stresses on the Mohr circle. Normal faulting is assumed. a) Changes in the Mohr circle activated due to the thermal contraction of the reservoir. b) Changes in the Mohr circle activated with a pore pressure increase considering different effects as Terzhagui's Law and increase in the stress magnitudes with pore pressure (see text for details).

Chapter 6

Synthesis and conclusions

The purpose of this chapter is to provide an overview of the main results obtained throughout the studies presented in the previous chapters and link them towards an integrated discussion on their impact for reservoir geomechanics. In addition to the main goal of this thesis –an improved understanding of processes in geo-reservoirs related to stimulation, production and storage- I also discuss the current limitations of the performed studies and provide suggestions on how these studies could be further improved in the future. Finally, I provide an outlook on new research topics that emerged from this study.

6.1 Discussion of results and conclusions

One of the main lessons learnt from the case study at the CO_2-EOR Penn West Pilot Project is the importance of performing an appropriate seismic monitoring of the reservoir processes for the purpose of reliable reservoir characterization but also for safety issues such as leakage detection. In particular, the analysis of waveform data was difficult due to the continuous high electrical noise level as well as countless electrical disturbances observed at most of borehole geophones. In this case study, no seismic event was detected with magnitude above M_W -1. However, the continuous seismic recordings were used to detect systematic changes of the noise level at the sensors in connection with a fluid and gas leakage within the monitoring well. The Penn West Pilot Project demonstrated that the appropriate design of downhole seismic instrumentation plays a crucial role not only for monitoring processes within the reservoir but also to improve along-well leakage detection capabilities, a likewise relevant topic especially in the context of potential effects of downhole operations on fresh water bearing layers.

In contrast, the case study at The Geysers geothermal field in California provides an extensive seismicity catalog with thousands of induced seismic events recorded by tens of seismic stations forming the base for in-depth analysis. Furthermore, available hydraulic data allowed investigating the impact of fluid-injection and its relation to the occurrence of induced seismicity. Given that the pore pressure increase during fluid injections is lower at The Geysers than at Penn West, here it is highlighted that the pore pressure increase is not the only factor governing the occurrence and magnitude of induced seismic events. Other factors like the net volume of the fluid injected (McGarr, 2014), the injection rates or the local stress state may play an important role. Additionally, the different seismic response from both reservoirs could also be due to differences in rock types and geological settings between the tight greywacke sandstone from The Geysers and the porous conglomerate rocks from Penn West.

Knowledge on the in-situ stresses is of great importance in order to develop procedures for safe drilling operations and optimizing the production as the economical key parameter. The development of the MSATSI stress inversion software package may serve as an additional yet underestimated tool to be applied during monitoring of reservoir treatments.

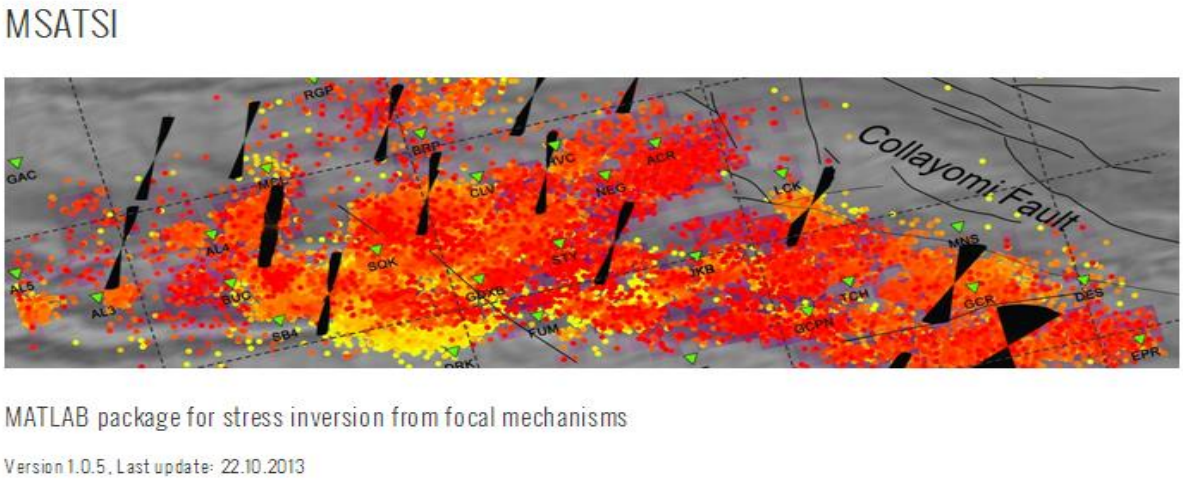

Figure 6.1 Main heading of the website dedicated to the software package MSATSI.

The updated code and extensive documentation are freely available for both scientific and applied purposes, and it might serve as user-friendly tool broadening the use of the stress inversion technique (Fig. 6.1).

MSATSI software package was effectively used not only for characterization of fluid-induced seismicity, but also in other scenarios such as natural tectonics and synthetic datasets. However, it is also important to be aware of the limitations. As MSATSI is based on the 'Slick' inversion code by Michael, (1984) and then extended by Hardebeck and Michael, (2006), it is assumed that the mean stress should be significantly larger than the corresponding deviatoric stress. For cases of high pore pressures, the effective normal stress will be reduced and the previous assumption will no longer hold. Therefore, the current version of MSATSI stress inversion as well as the other linear approaches would not be appropriate in scenarios with pore pressures approaching the magnitude of the minimum principal stress, as for example hydraulic fracturing experiments. This would be a task to address in forthcoming studies and improvements of MSATSI package (see Chapter 6.2).

The analysis of the stress field and the orientation of principal stresses at different depths at The Geysers geothermal field reported normal faulting stress regime at reservoir depth and strike-slip above and below the reservoir. The changes in faulting regime were related to the long-term production activities and the consequent reduction of the horizontal stresses at the reservoir depth. Assuming a case of uniaxial strain, the decrease in the horizontal stresses is commonly accompanied by subsidence at the surface. This effect has been observed at The Geysers geothermal field in different studies over the entire field (e.g. Mossop and Segall, 1997; Vasco et al., 2013). The decrease in the horizontal stresses due to decrease in pore pressure had not been observed before from field data using focal mechanisms of fluid-induced micro-seismicity. Our observations are similar to those from the EGS at Soultz-sous-Forêts, France, where most of the seismicity presented normal faulting, but many strike-slip events occurred in the basement of the reservoir (Cuenot et al., 2006).

To perform an appropriate inversion for the stress field orientation one must find a balance to satisfy two conditions: On one hand, certain variety must be included in the fault plane solutions to correctly constrain the orientation of the three principal stresses and the relative stress magnitude (McKenzie, 1969; Hardebeck and Hauksson, 2001; Bohnhoff et al.,

2004). On the other hand, the stress field orientation within the selected region should be homogeneous to obtain reliable results. In Chapter 3.4.2 it was shown that the stress field at the reservoir depth at the entire The Geysers can be considered first-order homogeneous. The stress regime is mostly normal faulting, while the central part is slightly transtensional. However, when looking at the stress field orientation in finer detail, second-order changes of the stress field orientation might appear. As an additional test, the spatio-temporal distribution of stress field orientation at the reservoir depth was investigated. The methodology was analogous to that reported in Chapter 3.4.2, but separating the focal mechanisms into different snapshots containing time periods of two years. These results show that the areas dominated by strike-slip stress regime are decreasing over the analyzed six years, while the areas displaying normal faulting are increasing (Fig. 6.2). Therefore, this observation also supports the interpretation that the long-term production from the reservoir decreases the horizontal stresses and promotes normal faulting at reservoir depth.

One of the most relevant results obtained in the frame of the here presented work is the observation of significant local temporal changes of the stress field orientation directly correlated to peak injections in the northwestern part of The Geysers geothermal field. From hydro-mechanical models it was somehow expected that the orientation of the principal stresses in a reservoir may vary during peak injections (e.g. Day-Lewis, 2008). However, such stress rotations during high injection rates had never been observed. The most important implication from this observation is that stress inversion from focal mechanisms of (induced) seismicity can be effectively used as a proxy to monitor stress changes in geo-reservoirs during reservoir treatment in general and undergoing fluid injection in particular. However, stress field orientation changes due to fluid injection may not be detectable in all case studies, given that a sufficient quantity of well-observed seismic events is needed during each injection stage to properly constrain the inversion. This requires usually an extensive local seismic network of surface (and if possible borehole) stations providing sufficient coverage of seismic sources.

The reported changes in the stress field orientation during peak injections were initially attributed to either reactivation of different pre-existing fractures or to potential tensile opening of cracks during peak-injections in the direction of S_{HMax}. Since seismic moment tensors for this particular seismicity catalog have not been calculated, the hypothesis of a significant non-DC component cannot be tested. However, results on moment tensors in larger-magnitude events show that non-DC components do play an important role in the source process of induced seismicity at The Geysers geothermal field (Guilhem et al., 2014). In the case that the non-DC components of the seismic events were non-negligible also for the smaller events, they may indicate local changes in the orientation of the P and T axes, and hence, the estimated stress field orientation. The modification of the P and T axes is expected to be small and most likely will not have a substantial impact on the stress field orientation, but further studies need to be performed to assess this effect.

To better understand the causes of the stress rotations during peak-injections, a comprehensive seismological and geomechanical (‘seismomechanical’) analysis was performed. Various properties of the seismicity within the individual stages of two injection cycles (before/during/after peak-injections) were investigated separately. It was finally concluded that the observed stress rotations were caused by the transient pore pressure increase during peak-injections resulting in decreasing the effective normal stress according to Terzaghi’s Law (Eq. 1.6). At the same time, two other poroelastic effects are superimposed: 1) The magnitude of the horizontal stresses increase proportionally to pore pressure as

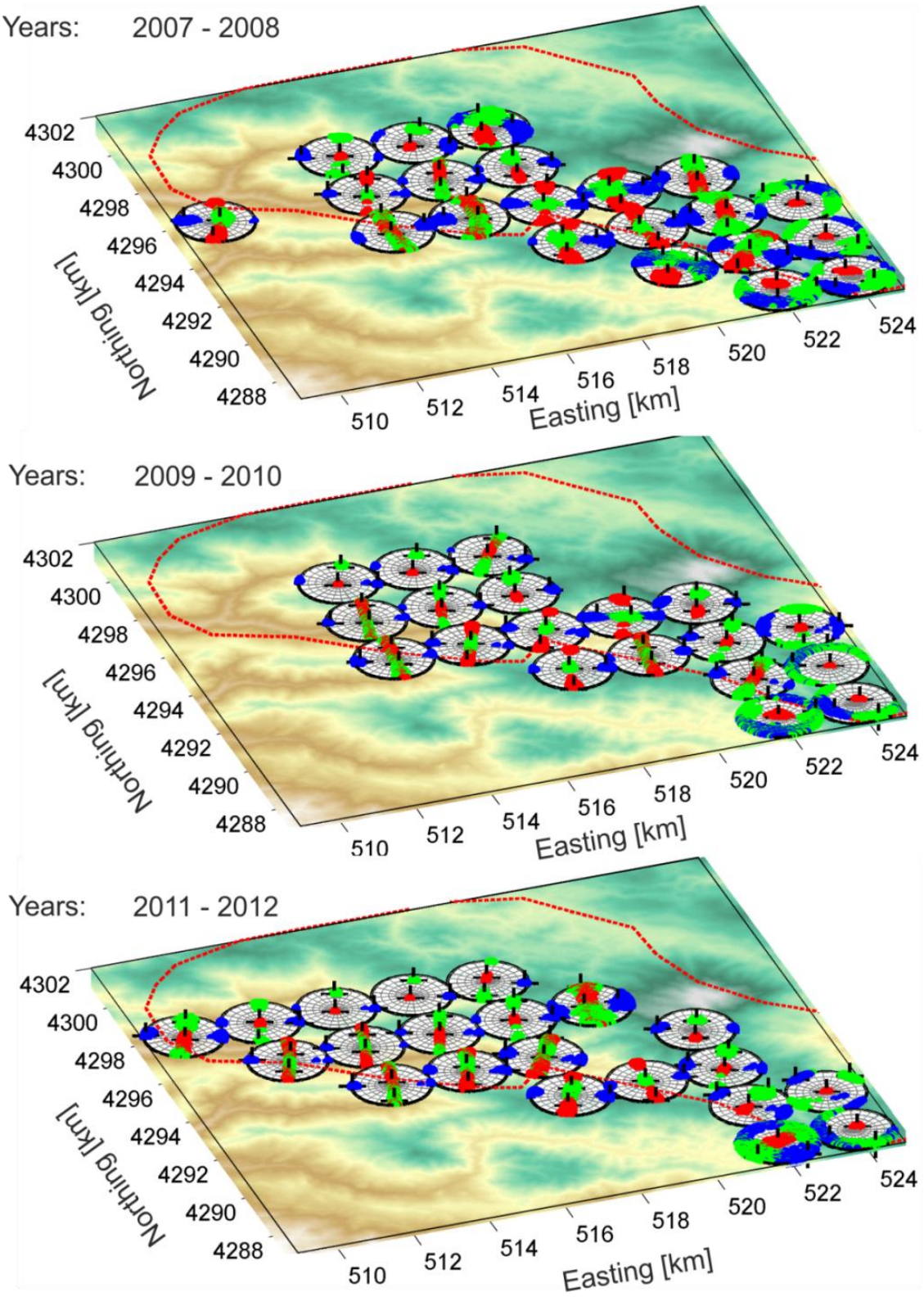

Figure 6.2 2-D distribution of the stress field orientations at The Geysers performed at reservoir depth (2-3 km) covering time periods of two years. From top to bottom: years 2007-2008, 2009-2010 and 2011-2012, respectively. The colored map represents the topography of The Geysers area. Red: σ_1. Green: σ_2, Blue: σ_3.

described by Eq. 1.11, 2) The relative distribution of radial/tangential stresses from the injection well with respect to the orientation of the horizontal stresses results in increasing the differential stress along the direction of S_{HMax} (Schoenball et al., 2010). These effects modify differently each principal effective stress. As a result, the new stress tensor will have different eigenvalues and eigenvectors than the initial one, creating a rotation of the stress field. Once that the volume of fluid injected decreases and the pore pressure returns to previous values, a similar state of stress is restored.

This study also reported changes in other seismological and geomechanical parameters. It was observed that during peak injections, the relative number of strike-slip and thrust faulting events increased as well as the average distance of the seismicity from the injection point. Also, the seismicity tended to align with the direction of S_{HMax}, suggesting the potential increase in differential stress within this orientation during peak injections. Additionally, temporal changes in the *b* value and in the relative stress magnitudes were observed. The observed changes led to the hypothesis that the contribution of the different physical mechanisms responsible for inducing the seismicity is non-stable, but in contrast it shows clear variations between different stages of the injection cycle. Particularly, it was proposed in this study that before and after peak-injections, thermal fracturing could be playing the most relevant role given the elevated reservoir temperature (≈240°C) and the relatively-high seismicity rate. However, during the peak injections, poroelastic effects associated with the pore pressure increase should not be neglected. The proposed model for the occurrence of seismicity at the selected site in the northwestern part of the field is very relevant given that, although it has been proposed with synthetic-numerical models (Rutqvist et al., 2013; Jeanne et al., 2014), it had not been observed from the seismicity of a geothermal field. Other studies have analyzed the seismic response from fluid injection/production. Particularly at the Salton Sea geothermal field, special attention was given to the long-term implications of the geothermal activities (Brodsky and Lajoie, 2013). To knowledge, no studies are yet available analyzing the short-term seismic response of a fluid injection focusing on the different injection stages (before/during/after peak injections).

However, some limitations must be accounted for when applying this model to The Geysers as a whole or to other geothermal sites. First, the injection at the analyzed site is continuous in time with seasonal variations and no shut-in is included. In this respect, the proposed induced seismicity mechanisms can be representative for other long-term fluid-injection projects, as for example the Salton Sea in Southern California (Brodsky and Lajoie, 2013), the Cooper Basin in Australia (Baisch et al., 2009) , Berlín in El Salvador (Majer et al., 2007; Kwiatek et al., 2014a) or in general any other project excluding the shut-in phase (for example Soultz-sous-Forêts, France or Basel, Switzerland). Second, for the analyzed spatio-temporal frame at The Geysers geothermal field the steam production was negligible. While for this study rejecting the production was correct, this might not be in general representative for geothermal sites subjected to long-term exploitation, as for example considering the processes at the entire The Geysers. However, the model might be able to reproduce correctly the processes occurring during the stimulation phase of a geothermal reservoir. Further analysis might be performed to include the production balance to other case studies where it might play a significant role (see Chapter 6.2). Third, note that the thermal fracturing considered that the heat is mainly propagating by conduction, which is usually valid for geothermal projects with relatively low porosity. If the main mechanism for heat transmission is advection, other additional constrains might have to be taken into account.

Lastly, the knowledge on the complete stress tensor and the pore pressure is essential to perform a safe drilling and optimized exploitation. Despite the large history of well-drilling

at The Geysers geothermal area, no data from leak-off tests is publicly available. For this reason, first-order estimation for the complete stress tensor before and during peak-injections at The Geysers has been here provided using focal mechanisms of the induced seismicity, density logs and further assumptions based on a critically stressed Earth crust. In this case, the most important parameter contributing to the overall uncertainty is the relative stress magnitude (R value). In addition, normal faulting regime was assumed regardless of the injection stage, while in reality during peak-injections the stress regime changed slightly to oblique. Last but not least, the estimation only takes into account the lithostatic weight and the poroelastic contributions on the stress field, while neither the tectonic stresses nor the thermal stresses are systematically included (see Chapter 6.2). Nevertheless, the estimations provided here are important since they are based on reasonable assumptions, no other better method for calculating the stress field from real data is available and they can be useful for a comprehensive seismological and geomechanical analysis.

6.2 Outlook for future related studies

The different studies developed through this dissertation form the base for addressing several other relevant topics that also could be further investigated. These are expected to have a significant potential and impact to achieve a better understanding of processes occurring in geological reservoirs. The most relevant ones are the followings:

Stress tensor inversion adding the pore pressure as an input parameter

As pointed out previously, the linear stress inversion approach developed by Michael, (1984) and later extended by Hardebeck and Michael, (2006) and by Martínez-Garzón et al., (in press) holds the hypothesis that the mean stresses are significantly larger than the deviatoric stresses. This is implicitly assumed with the hypothesis that the magnitude of the shear traction is equal to one and similar from fault to fault ($|\vec{\tau}|=1$). In other words, if the pore pressure is high, the validity of these stress inversion methods might be questioned. Given the raising importance of fluid-injection experiments involving high pore pressures, this issue needs to be treated. Therefore, an improved stress inversion method might consider parameterizing the previous condition in terms of the pore pressure to make the stress inversion method pore-pressure independent.

Influence of non-DC components on the stress inversion

While there are a whole variety of stress inversion methods using different techniques, all of them are based on the hypothesis of the DC source as earthquake mechanism. However, several studies have shown that seismicity might display non-negligible non-DC components, as for example during fluid injection (Ross et al., 1999), seismicity from pull-apart basins (Stierle et al., 2014) or during shear-compaction laboratory experiments (Kwiatek et al., 2014b). The non-DC components may vary the orientation of the P and T axes, which are in fact the input for the stress inversion. Therefore, it would be useful to investigate the influence of non-DC components on the stress inversion and the resulting stress field orientation. This could be checked for example creating synthetic sets of moment tensors with different amount

of non-DC component and observing the perturbation from the original DC source. In case that the effect of the non-DC would be significant enough, different approaches for including the non-DC sources into the inversion scheme could be tested.

Long-term evolution of the seismic response at NW The Geysers geothermal field

The seismic analyses presented in Chapter 5 focus on a seismicity cluster at The Geysers geothermal field and were estimated from data covering a five-year time period. For the time being, only the short-term response to peak fluid-injections has been interpreted in detail, but the obtained results revealed long-term evolution of seismic parameters that have not yet been analyzed. The seismic parameters calculated here as well as other additional quantities will be used to trace the long term evolution of this particular part of NW-The Geysers. The most interesting aspects of this study are the geomechanical behavior of the reservoir after numerous injection cycles, the effects of introducing a second well in the vicinity and spreading the volume of fluid injected in the reservoir through two wells and the temporal evolution of the principal stress magnitudes with time.

Improving the estimation of the state of stress

Given its extreme importance in fundamental research as well as in applied geosciences, the estimation of the complete stress tensor at depth is a challenge that has been addressed in many case studies. Different approaches have been tested using borehole breakouts, leak-off tests or focal mechanisms of seismicity. As indicated previously, the current estimation of the state of stress has some limitations in agreement with the state-of the art knowledge on the topic. One of the ways to improve the estimation of the state of stress (the principal stress magnitudes) would be to include detailed estimation of the pore pressure with space and time. When available, direct measurements could be used. When lacking of direct measurements, spatio-temporal pore pressure characterization might be achieved by applying pore pressure propagation models (Shapiro et al., 2003; Rothert and Shapiro, 2007) or by using indirect estimators such as the V_p/V_s ratios (Moreno et al., 2014), spatial distribution of stress drops (Goertz-Allmann et al., 2011), or by focal mechanism tomography (Terakawa et al., 2010). Additionally, one important step would be to investigate different approaches to incorporate the tectonic stresses as well as the thermal stresses into the stress magnitude calculation.

Temporal changes in the stress field orientation related to the occurrence of LME

Several studies from tectonic natural seismicity have shown that the occurrence of a great earthquake has a temporal influence in the stress field orientation of the surrounding area (e.g. Bohnhoff et al., 2006; Hardebeck, 2012; Yoshida et al., 2012; Ickrath et al., 2014). However, to date it has not been investigated whether this phenomenon also occurs at reservoir scale. Given the abundant amount of micro-seismicity available at reservoir scale it might be worth to check whether a similar effect occurs also after the occurrence of LMEs at the reservoir scale. This application might also provide a good opportunity to compare the differences or similarities between natural and induced seismicity.

Appendix A

High-resolution reservoir characterization using induced seismicity and state of the art waveform processing techniques[5]

Grzegorz Kwiatek, Marco Bohnhoff, Patricia Martínez-Garzón, Fatih Bulut, Georg Dresen

[5] Published in *First Break* as: Kwiatek G., Bohnhoff, M., Martínez-Garzón, P., Bulut, F., Dresen G. (2013). High-resolution reservoir characterization using induced seismicity and state of the art waveform processing techniques. *First break*, 31, 7, pp 81-88.

Summary

In this study we present applications of waveform processing techniques that are well-established in fundamental seismology to investigate physical processes acting during stimulation of geothermal reservoirs. The analysis of hundreds of induced seismic events related to stimulation at the Berlín geothermal field is used as a case study stressing that double-difference relocation and spectral ratio methods significantly improve the precision of hypocenter locations and source parameters. The refined parameters allow a detailed analysis of spatio-temporal evolution of the seismicity related to fluid injection previously not visible due to limited resolution. Applying the stress inversion technique to focal mechanisms of induced seismic events related to stimulation at The Geysers geothermal field we observe significant rotations of the stress field orientation directly related to flow rates during fluid treatment. Moreover, this stress rotation is reversible documenting that stress inversion might be used as an additional proxy to monitor reservoirs during and after stimulation.

A.1 Introduction

Passive seismic monitoring (PSM) is a well-established but still widely underestimated technique to characterize processes occurring in any type of geo-reservoir (geothermal, hydrocarbon, CO_2 storage and unconventional gas). Despite the great potential of the method, state-of-the art seismological techniques applied to natural seismic events have not yet been widely applied in geo-reservoir monitoring (Bohnhoff et al., 2010a). There are numerous studies using PSM and various processing techniques to characterize and understand physical processes governing induced seismicity in different types of geo-reservoirs (Majer et al., 2007; Bohnhoff and Zoback, 2010; Kwiatek et al., 2010, 2014a; Evans et al., 2012; Goertz-Allmann et al., 2013; Martínez-Garzón et al., 2013; Albaric et al., 2014). Their overall purpose is to passively monitor if not mitigate the seismic hazard related to the occurrence of induced seismicity (IS) and to develop strategies for safe and efficient reservoir stimulation and exploitation.

In this study we present the application of three state-of-the-art algorithms, namely the Double-Difference (hypoDD) re-location technique, the Spectral Ratio (SR) technique and the Stress Inversion (SI) method in analyzing IS generated by fluid injection and steam production at The Geysers and Berlín geothermal fields in California and El Salvador, respectively. We show how hypoDD significantly improves the precision of hypocenters allowing imaging the fluid path and propagation in response to multiple injections with unprecedented detail. In addition, the application of the SR technique provides refined source parameters that can later be used to interpret the subtle interactions between pressure perturbations, fluid flow and fracture (re-)activation within the reservoir. Finally, we show how the SI technique can contribute towards monitoring geomechanical processes occurring in the reservoir in response to short-term injection and long-term production activities.

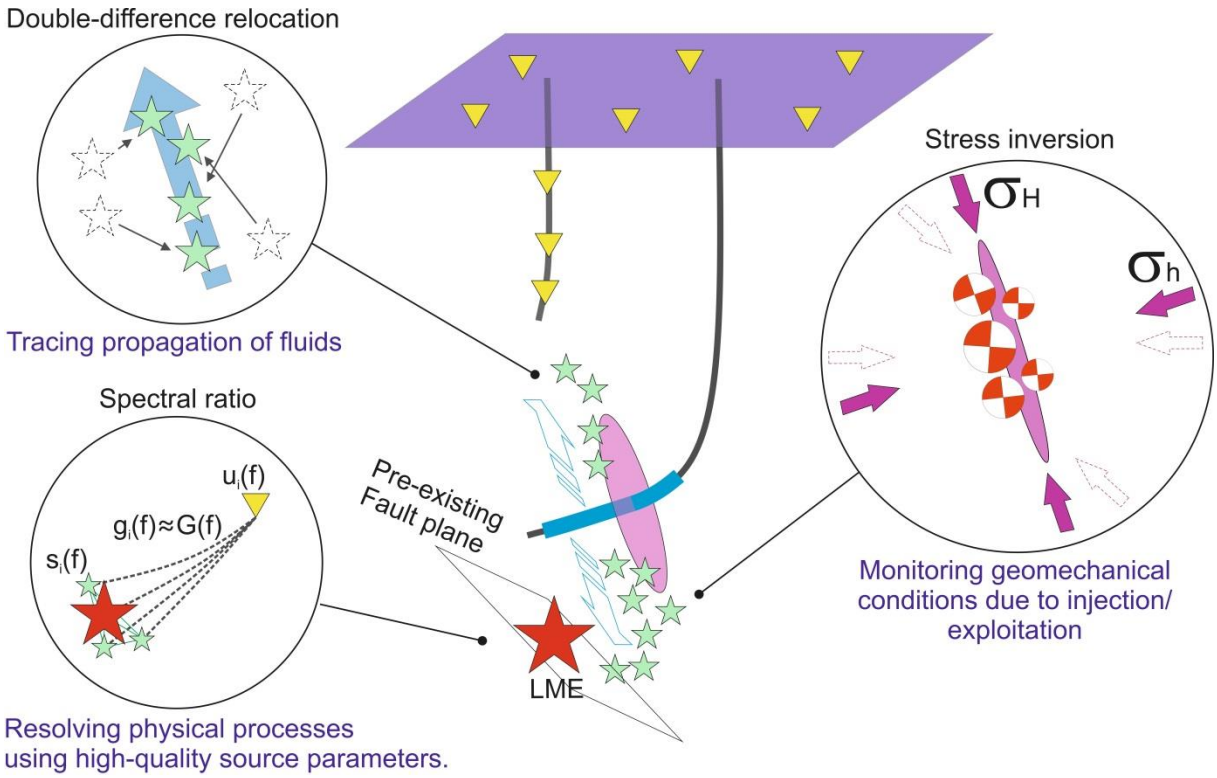

Figure A.1 Schematic presentation of the three methods applied in the study.

A.2 Methods

A.2.1 Double-difference re-location

The double-difference (DD) relative re-location technique (hypoDD) (Waldhauser and Ellsworth, 2000) uses differential travel times of body waves to improve the hypocenter location accuracy (Fig. A.1). The differential travel times are determined for station-specific P and S wave arrivals of closely-spaced pairs of events. This allows suppressing poorly known velocity models in and around the reservoir, since the differential travel times are not sensitive to the path effects between the sources and receivers. Eliminating path effects allows improving hypocenter precision by a factor of typically more than 10 compared to absolute locations thereby achieving a much finer internal resolution of the seismicity clusters. Additionally, the waveform cross-correlation techniques may be used to revise the relative arrival times and provide even more precise hypocenter (re-)locations.

A.2.2 Spectral ratio method

The spectral ratio method (SR) is again a relative technique that can be used to significantly decrease the uncertainties of seismic source parameters such as the seismic moment as a measure for the energy released during an induced earthquake, corner frequency as a measure for its fault size and static stress drop or apparent stress for assessing the damaging potential of a seismic event. Consequently, the refined source parameters may provide additional information on processes induced by human activity but usually not detected in standard analysis. Recently, it has been suggested that the SR-refined static stress drops of IS may serve as a proxy for modeling the pore pressure perturbations related to fluid injections (Goertz-Allmann et al., 2011; Kwiatek et al., 2014).

The SR method also takes advantage of the similar source-receiver travel paths between the seismic events within the same cluster. Assuming that the seismogram of event *i* recorded at a sensor *k* is a convolution of seismic source $\Omega_i(f)$, path $G_{ik}(f)$, site $S_k(f)$ and sensor $T_k(f)$ effects:

$$u_i(f) = \Omega_i(f) G_{ik}(f) S_k(f) T_k(f) \qquad [A.1]$$

a *spectral ratio* between suitable pairs of seismic events from the same cluster may be formed fulfilling certain criteria (for details, see e.g. Kwiatek et al., 2011). Forming a spectral ratio between two events $u_i(f) \Big/ u_j(f)$ results in cancelling of the site, sensor, and propagation effects ($G_{ik}(f) \approx G_{jk}(f)$) once the distance between pairs of earthquakes is much smaller than the distance to the sensor. Many spectral ratios may be formed between events contained in a spatial seismicity cluster. The bulk inversion for source parameters, typically seismic moment and corner frequency, of all events can be performed using Monte-Carlo techniques resulting in very precise source parameters due to suppressed path and sensor-related effects.

A.2.3 Stress inversion

The crustal stress field orientation can be determined directly from borehole data (borehole breakouts, drilling induced fractures, in-situ stress measurements), but also indirectly by inverting earthquake focal mechanisms by applying a stress inversion (SI). The latter has proven to be a robust and effective technique to study fault mechanics or spatiotemporal rotations of stress axes in response to large earthquakes along plate boundaries. At the reservoir scale, the direction of the principal stress axes provides important information for planning the stimulation operations. Another important application of SI concerns seismic hazard assessment. For example, knowledge of stress orientations allows estimating the fault re-activation potential from reservoir stimulation (Moeck et al., 2009). Finally, the changes in the stress tensor orientation may be a proxy to determine geomechanical processes occurring in the reservoir on the short-term (massive fluid injection) or on the long-term (reservoir depletion). Various SI schemes have been developed to determine the orientation of the stress field from focal mechanisms (e.g. Michael, 1987; Rivera and Cisternas, 1990). However, SI has not yet been extensively applied to seismicity induced in geo-reservoirs. A few existing studies focus on detecting variations of the stress with depth, possibly providing insights in potential stress changes within the reservoir (Oppenheimer, 1986; Bohnhoff et al., 2004).

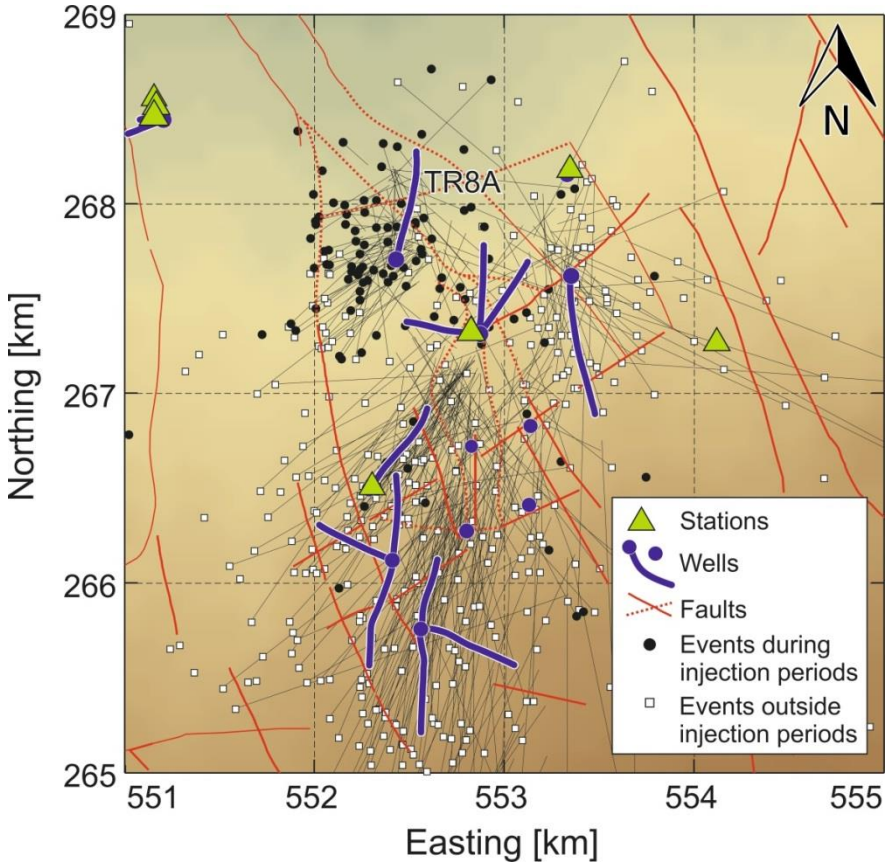

Figure A.2 BGF: Spatial distribution of 581 seismic events recorded between Oct-2002 and Jan-2004 (locations provided by BGF operator). Thin gray lines display shifts in earthquake locations towards the center of the BGF due to the application of DD relocation technique (cf. Fig. A.4).

A.3 Data

We applied the techniques described above in characterizing IS and geomechanical processes at two geothermal reservoirs, the Berlín Geothermal Field (BGF) in El Salvador and The Geysers (TG) in California. While these are selected case studies we believe that these methods can be applied to any data set of IS with a reasonably good quality of the recorded waveforms obtained from a sufficient monitoring network.

BGF is located at the northern flank of the Cerro Tecapa volcano. The power plant produced 54 M_W (as of 2006) from eight production wells with the fluid being extracted at a temperature of 183°C and disposed via re-injection through a total of ten wells (Bommer et al., 2006). The seismic and production/injection data provided by the BGF operator covers three stimulations (each lasting between 18 and 21 days) performed between Jun-2003 and Jan-2004 in the injection well TR8A located in the northern part of the main production zone (Fig. A.2) (Kwiatek et al., 2014). The stimulations aimed at increasing the permeability around the well and extending the production zone further to the north. The local seismic network composed of 13 borehole sensors was installed to monitor the evolution of the microseismicity and therefore the potential expansion of the reservoir. The original industrial hypocenter catalogue contained 581 events with magnitudes ranging from -0.5 to 3.7 recorded

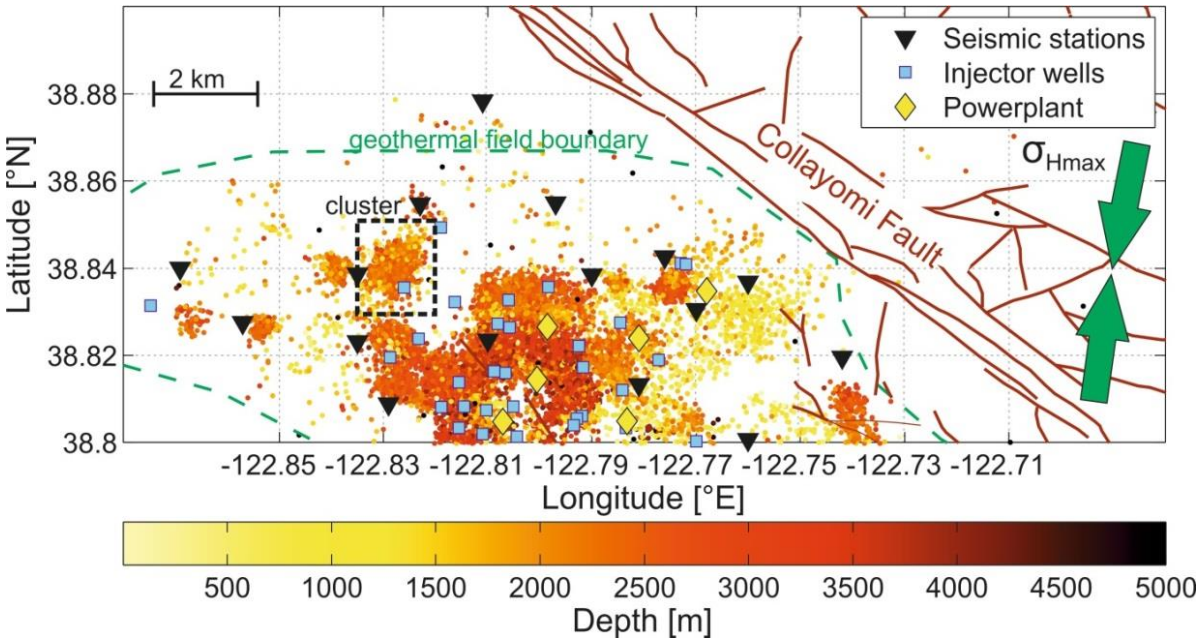

Figure A.3 TG: Spatial distribution of the seismicity recorded between Sep-2007 and Jul-2012 in the north-western part of TG. The dashed rectangle shows a cluster containing 742 earthquakes used to perform the SI.

between Oct-2002 and Feb-2004 (Fig. A.2). Only 134 events framing the stimulation campaigns in the well TR8A had been analyzed in terms of the spatial and temporal evolution and source parameters using DD and SR methods.

TG is the largest geothermal field in the world in terms of steam production, with 1517 M_W active installed capacity and average production of 955 M_W (DiPippo, 2008). It has also the largest existing dataset of IS consisting of more than 500,000 located microseismic events since the beginning of operation in the 1960s. Since 2007, the installed local seismic network was operated by the Lawrence Berkeley National Laboratory. The network consists of 31 short period 3-component geophones recording more than 3000 events with magnitudes $M \geq 1$ annually. The occurrence of seismic events is directly related to the injection of water into the reservoir and vapor production. We selected a subset of seismic data induced by injection campaigns performed between Oct-2007 and Jun-2012 in two wells located in the northern part of the reservoir (Fig. A.3). A total of 742 earthquake focal mechanisms with magnitudes ranging from 1.0 to 3.1 were analyzed aiming at investigating potential changes in the stress field related to injection using two different SI methods (Martínez-Garzón et al., 2013).

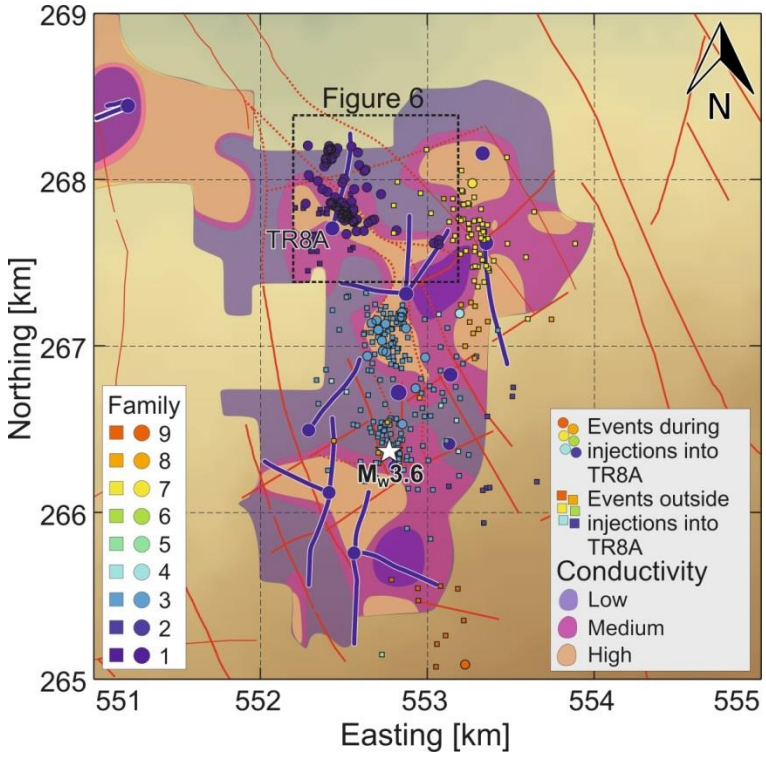

Figure A.4 BGF: Spatial distribution of 393 events relocated with DD technique. The accumulation of events in the highly permeable zones and along the faults is clearly visible.

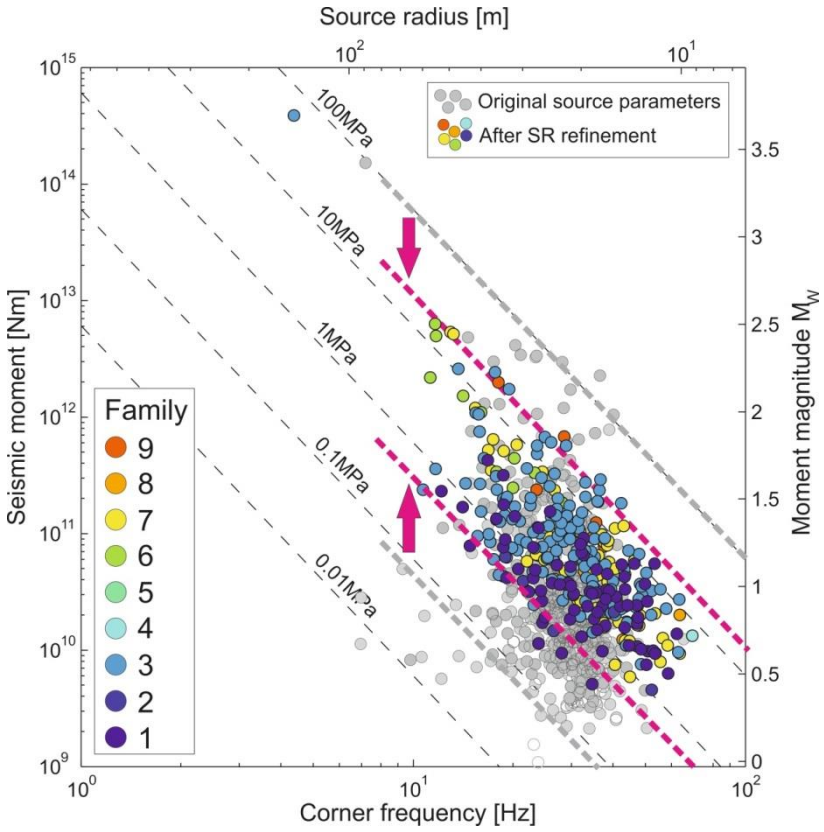

Figure A.5 BGF: Comparison of original (grayed circles) and SR-refined source parameters (color-coded circles reflecting the family number). A decrease in the scatter of static stress drops is observed (purple dashed lines and arrows) after application of SR technique.

A.4 Discussion

The original seismicity catalog from BGF reflects the typical location quality for absolute hypocenter locations at these monitoring conditions (Fig. A.2). The hypocenter distribution does not allow identifying any specific spatio-temporal pattern related to the multiple injections into the well TR8A. Instead the events form a scattered cloud of seismicity around the injection well. This is well-explained by using a simplified isotropic model and standard quality phase arrival picks. Therefore, to improve the quality of the initial dataset we applied the DD re-location algorithm along with refined P and S wave arrival times derived from waveform cross-correlation and using the 1D-velocity model available for BGF (Rivas, 2000). The average precision of the absolute locations was typically 150 m (previously >300 m). Applying re-location then resulted in lowering the average relative hypocentral location misfit of a total of 393 events down to ~10 m, which is in the range of the source size. Fig. A.4 displays the substantial improvement in the hypocenter locations now allowing for a detailed analysis of spatio-temporal behavior of the seismicity and its relation to fluid injections into well TR8A. In a second step, events were divided into nine families based on waveform similarity obtained from waveform cross-correlation. The source parameters of events belonging to the same family were then recalculated and refined using the SR technique (see Kwiatek et al., 2011 for details). The results of the refinement are presented in Fig. A.5. It is clearly seen that the original source parameters are significantly affected by high attenuation observed in the investigated area. No events with higher corner frequencies (f>60 Hz) are observed despite a broad recording bandwidth of the sensors up to 1500 Hz and a high signal-to-noise ratio. Initial stress drop values covered a broad range exceeding 3 orders of magnitude reflecting rather strong uncertainties in estimated source parameters. However, the SR method effectively cancelled path effects resulting in a significant improvement of source parameters estimation.

Both DD and SR methods provided significantly refined hypocenter locations and source parameters. This allowed investigating the interactions between fluid injections into TR8A and the observed patterns of induced microseismicity. This in-depth analysis could not have been performed given the initial dataset due to its insufficient quality.

To summarize our observations (cf. Fig. A.6):

1. We found seismic activity displaying clear spatial and temporal patterns that could be easily related to the injections into the well TR8A. The migration of seismicity away from the injection point is observed for injections 1+2 ([1] in Fig. A.6) while the injection rate is increasing. Migration of events continues until shut-in of the well. The clustering of seismicity at the injection well is found at greater depth during injection 3 ([2] in Fig. A.6).
2. The locations of migrating seismic events are related to the existing fault system F1. The DD-relocated hypocenters systematically align along different faults mapped at the surface or imaged at depth (Santos and Rivas, 1999). Events with larger magnitudes typically occur right after the shut-in of the well concentrating in undamaged parts of the fault system, a well-known phenomenon from various previous studies of seismicity induced by massive fluid injection. ([3] in Fig.A.6).
3. Continuing stimulation episodes require increased injection rate levels (and thus increased reservoir pressure) to induce seismic activity in previously active volumes which is interpreted to reflect a crustal memory (“Kaiser”) effect (Kaiser, 1953) first observed during laboratory studies in the 1960s.

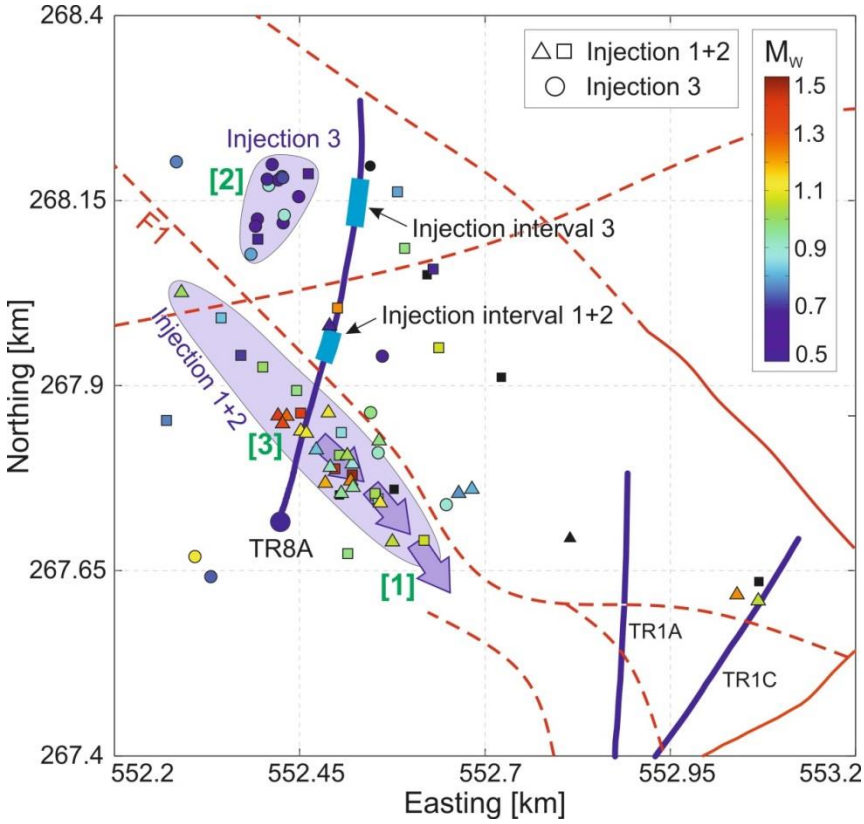

Fig. A.6 BGF: A detailed map view of the area of TR8A injector well. Spatial and temporal changes of seismicity in response to multiple injections are visible (see text for details).

4. We observe that static stress drop values increase with distance from the injection point, possibly related to pore pressure perturbations introduced by stimulation of the respective part of the reservoir.
5. We find that seismic activity concentrates in highly conductive parts of the reservoir. However, a larger magnitude event M_W 3.6 (Bommer et al., 2006) rather occurred in an area of a gradient in conductivity with the aftershock sequence being located in an area of low electrical conductivity (cf. Fig. A.4).

SI was applied to 742 earthquake focal mechanisms from the TG geothermal field (Fig. A.3) that occurred at depths ranging between 2000-3000 m in response to five years of ongoing injections performed in two wells (Martínez-Garzón et al., 2013). The seismicity data includes a sufficiently high number of focal mechanisms which allows investigating potential changes of stress field orientation in response to changes in flow rate. The selected time interval covered two injection campaigns performed between Oct-2007 and Jun-2012. Creating moving windows of 55 events, we performed a stress inversion of focal mechanism using a modified version of the SATSI software package (Hardebeck and Michael, 2006). In addition we performed a bootstrap resampling uncertainty assessment.

The results summarized in Fig. A.7 clearly show a statistically significant systematic rotation of the principal stress axes during periods of massive fluid injection at the 95% confidence level. This suggest that variations in the stress tensor orientation might serve as a proxy for detecting and monitoring changes in the stress state of geo-reservoirs directly related to fluid injection, which is observed directly for the first time. While this process is reversible we also notice the decrease in stress rotation with repeated injections. The rotations

of the stress tensor are interpreted in terms of re-activation of pre-existing local faults and fractures well-oriented according to regional stress field orientation. Alternatively, the results might as well suggest that the massive fluid injection aiming at increasing the permeability of the reservoir (Enhanced Geothermal System) allowed for the creation and opening of small fractures oriented in the direction of maximum horizontal stress.

A.5 Conclusions

Applying state-of-the-art seismological approaches to geo-reservoir characterization has a huge potential. In this study we presented applications of seismological techniques rarely used in reservoir characterization allowing a better understanding of injection related processes occurring in geo-reservoirs. In particular we find that high-precision relative DD re-locations are of fundamental importance for detecting and investigating fluid paths and progressing pressure perturbations. We show how additional information on physical processes, previously not visible due to high uncertainties, may be obtained from source parameters refined using the SR technique. Finally, it is well known that development of geo-reservoirs is significantly affected by the stress state in the earth crust. We presented the stress inversion technique using focal mechanism of earthquakes and notice that SI may be an efficient tool to determine the crustal stress field changes at depth due to field operations.

High precision hypocenter determination, spectral ratio refinement of source parameters as well as the stress tensor inversion can substantially improve the understanding of physical processes occurring in any type of geo-reservoir. The proposed methods can be applied if appropriate microseismic monitoring is performed and if the data quality and quantity is sufficient, but they also may be used to re-investigate already collected data previously processed with conventional methods.

Acknowledgments

We acknowledge provision of seismic and hydraulic data by Shell Ltd. (S. Oates), NORSAR (V. Oye, J. Albaric, D. Kühn), J. Bommer, G. Siddiqi, North California Earthquake Data Centre, Dept. of Conservation. CA and Calpine LTD. Funding of the studies presented in this paper were granted by the Helmholtz-Alberta Initiative (HAI), Helmholtz Foundation (Young Investigators Group) and the FP7 EU-GEISER project

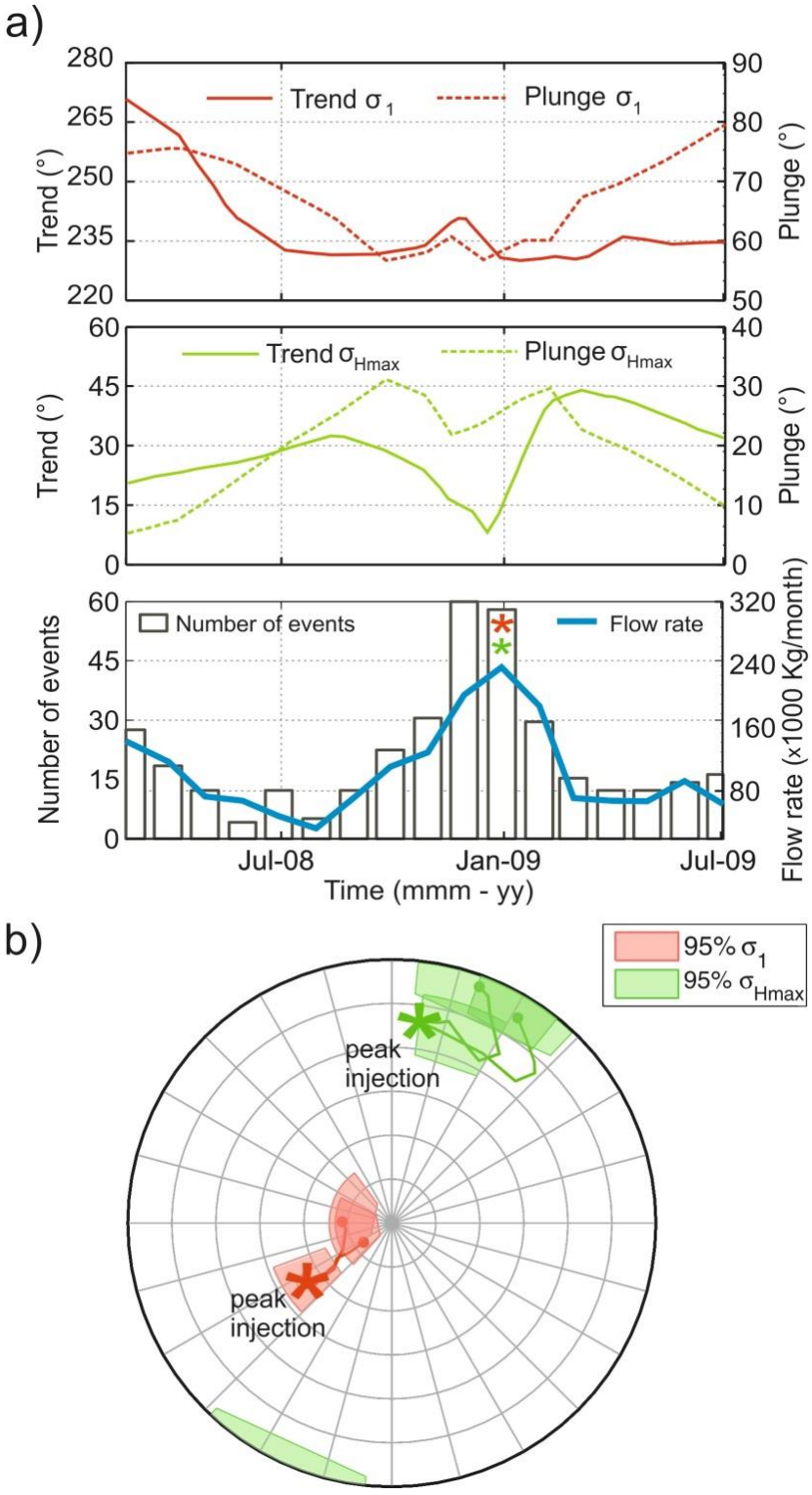

Figure A.7 TG: Example of the relation found between peak injection and a temporal variation of the stress field orientation. a): Changes in σ_1 and σ_{HMax} together with flow rate and number of recorded events. b): variation in stress axes orientation over time.

References

Abercrombie, R. E. (1995). Earthquake source scaling relationships from -1 to 5 M_L using seismograms recorded at 2.5-km depth, *J Geophys Res* **100**, 24015–24036.

Abers, G. A., and J. W. Gephart (2001). Direct inversion of earthquake first motions for both the stress tensor and focal mechanisms and application to southern California, *J. Geophys. Res. Solid Earth* **106**, no. B11, 26523–26540, doi 10.1029/2001JB000437.

Aki, K., and P. G. Richards (2002). *Quantitative Seismology: Theory and Methods*, University Science Books, Herndon, VA 20172.

Albaric, J., V. Oye, N. Langet, M. Hasting, I. Lecomte, K. Iranpour, M. Messeiller, and P. Reid (2014). Monitoring of induced seismicity during the first geothermal reservoir stimulation at Paralana, Australia, *Geothermics* doi: 10.1016/j.geothermics.2013.10.013.

Allis, R. G. (1982). Mechanism of induced seismicity at the Geysers Geothermal Reservoir, California, *Geophys. Res. Lett.* **9**, no. 6, 629–632, doi 10.1029/GL009i006p00629.

Altmann, J. B., B. I. R. Müller, T. M. Müller, O. Heidbach, M. R. P. Tingay, and A. Weißhardt (2014). Pore pressure stress coupling in 3D and consequences for reservoir stress states and fault reactivation, *Geothermics* doi 10.1016/j.geothermics.2014.01.004.

Anderson, E. M. (1951). *The dynamics of faulting and dyke formation with applications to Britain*, Hafner Pub. Co., Houston, Texas.

Angelier, J. (1984). Tectonic analysis of fault slip data sets, *J. Geophys. Res. Solid Earth* **89**, no. B7, 5835–5848, doi 10.1029/JB089iB07p05835.

Arnold, R., and J. Townend (2007). A Bayesian approach to estimating tectonic stress from seismological data, *Geophys. J. Int.* **170**, no. 3, 1336–1356, doi 10.1111/j.1365-246X.2007.03485.x.

Bachmann, C. E., S. Wiemer, J. Woessner, and S. Hainzl (2011). Statistical analysis of the induced Basel 2006 earthquake sequence: introducing a probability-based monitoring approach for Enhanced Geothermal Systems, *Geophys. J. Int.* **186**, no. 2, 793–807, doi 10.1111/j.1365-246X.2011.05068.x.

Bachmann, C. E., S. Wiemer, B. P. Goertz-Allmann, and J. Woessner (2012). Influence of pore-pressure on the event-size distribution of induced earthquakes, *Geophys. Res. Lett.* **39**, no. 9, n/a–n/a, doi 10.1029/2012GL051480.

Bachu, S. (2002). Sequestration of CO2 in geologic media in response to climate change: road map for site selection using the transform of the geological space into the CO2 phase space, *Energy Conserv. Manag.* **43**, 277–289.

Baisch, S., and H.-P. Harjes (2003). A model for fluid-injection-induced seismicity at the KTB, Germany, *Geophys. J. Int.* **152**, no. 1, 160–170, doi 10.1046/j.1365-246X.2003.01837.x.

Baisch, S., and R. Vörös (2010). Reservoir induced seismicity: Where, when, why and how strong?, in *Proceedings World Geothermal Congress*, Bali, Indonesia.

Baisch, S., M. Bohnhoff, L. Ceranna, Y. Tu, and H.-P. Harjes (2002). Probing the Crust to 9-km Depth: Fluid-Injection Experiments and Induced Seismicity at the KTB Superdeep Drilling Hole, Germany, *Bull. Seismol. Soc. Am.* **92**, no. 6, 2369–2380, doi 10.1785/0120010236.

Baisch, S., R. Weidler, R. Vörös, D. Wyborn, and L. de Graaf (2006). Induced Seismicity during the Stimulation of a Geothermal hfr Reservoir in the Cooper Basin, Australia, *Bull. Seismol. Soc. Am.* **96**, no. 6, 2242–2256, doi 10.1785/0120050255.

Baisch, S., R. Vörös, R. Weidler, and D. Wyborn (2009). Investigation of Fault Mechanisms during Geothermal Reservoir Stimulation Experiments in the Cooper Basin, Australia, *Bull. Seismol. Soc. Am.* **99**, no. 1, 148–158, doi 10.1785/0120080055.

Baisch, S., R. Vörös, E. Rothert, H. Stang, R. Jung, and R. Schellschmidt (2010). A numerical model for fluid injection induced seismicity at Soultz-sous-Forêts, *Int. J. Rock Mech. Min. Sci.* **47**, no. 3, 405–413, doi 10.1016/j.ijrmms.2009.10.001.

Baria, R. et al. (2004). Microseismic monitoring of the world's largest potential HDR reservoir, in *Proceedings of the 29th Workshop on Geothermal Reservoir Engineering*, Stanford University, Stanford, USA.

Barker, B. J., M. S. Gulati, M. A. Bryan, and K. L. Reidel (1992). Geysers reservoir performance, *Monograhp Geysers Geotherm. Field Spec. Rep. No 17* , no. Geothermal Research Council, 167 – 178.

Baumgartner, J., A. Gerard, R. Baria, T. Jung, T. Tran-Vieta, t. Gandyn, L. Aquilina, and J. Garnish (1998). Circulating the HDR reservoir rock at Soultz: Maintaining production and injection flow in complete balance.

Boatwright, J. (1978). Detailed spectral analysis of two small New York State earthquakes, *Bull Seism. Soc Am* **68**, 1131–1177.

Boatwright, J., and D. M. Boore (1982). Analysis of the ground accelerations radiated by the 1980 Livermore Valley earthquakes for directivity and dynamic source characteristics, *Bull Seism. Soc Am* **72**, no. 6A, 1843–1865.

Bohnhoff, M., and M. D. Zoback (2010). Oscillation of fluid-filled cracks triggered by degassing of CO2 due to leakage along wellbores, *J. Geophys. Res. Solid Earth* **115**, no. B11, B11305, doi 10.1029/2010JB000848.

Bohnhoff, M., S. Baisch, and H.-P. Harjes (2004). Fault mechanisms of induced seismicity at the superdeep German Continental Deep Drilling Program (KTB) borehole and their relation to fault structure and stress field, *J. Geophys. Res. Solid Earth* **109**, no. B2, n/a–n/a, doi 10.1029/2003JB002528.

Bohnhoff, M., H. Grosser, and G. Dresen (2006). Strain partitioning and stress rotation at the North Anatolian fault zone from aftershock focal mechanisms of the 1999 Izmit M_W= 7.4 earthquake, *Geophys. J. Int.* **166**, no. 1, 373–385, doi 10.1111/j.1365-246X.2006.03027.x.

Bohnhoff, M., G. Dresen, W. L. Ellsworth, and H. Ito (2010a). Passive Seismic Monitoring of Natural and Induced Earthquakes: Case Studies, Future Directions and Socio-Economic Relevance, in *New Frontiers in Integrated Solid Earth Sciences*, edited by S. Cloetingh and J. Negendank, pp. 261–285, Springer Science+Businesss Media B.V. 2009.

Bohnhoff, M., M. D. Zoback, L. Chiaramonte, J. L. Gerst, and N. Gupta (2010b). Seismic detection of CO2 leakage along monitoring wellbores, *Int. J. Greenh. Gas Control* **4**, no. 4, 687–697, doi 10.1016/j.ijggc.2010.01.009.

Bommer, J. J., S.Oates, J. M. Cepeda, C. Lindholm, J. Bird, R. Torres, G. Marroquin, and J. Rivas (2006). Control of hazard due to seismicity induced by a hot fractured rock geothermal project, *Eng Geol.* **83**, no. 4, 287–306, doi 10.1016/j.enggeo.2005.11.002.

Bott, M. H. . P. (1959). The mechanics of oblique slip faulting, *Geol Mag* **96**, 109–117.

Boyle, K., and M. Zoback (2011). Stress and fracture orientation in the NorthWest Geysers geothermal field, *Proc. Thirty-Eight Workshop Geotherm. Reserv. Eng. Stanf. Univ. Stanf. Calif.*

Brodsky, E. E., and L. J. Lajoie (2013). Anthropogenic Seismicity Rates and Operational Parameters at the Salton Sea Geothermal Field, *Science* **341**, no. 6145, 543–546, doi 10.1126/science.1239213.

Brophy, P., M. J. Lippmann, P. F. Dobson, and B. Poux (2010). *The Geysers geothermal field; Update 1990-2010*, Geothermal Resources Council, Special report.

Brown, K. M., B. Bekins, B. Clennell, D. Dewhurst, and G. Westbrook (1994). Heterogeneous hydrofracture development and accretionary fault dynamics, *Geology* **22**, no. 3, 259–262, doi 10.1130/0091-7613(1994)

Bulut, F., M. Bohnhoff, M. Aktar, and G. Dresen (2007). Characterization of aftershock-fault plane orientations of the 1999 İzmit (Turkey) earthquake using high-resolution aftershock locations, *Geophys. Res. Lett.* **34**, no. L20306, doi 10.1029/2007GL031154.

Byerlee, J. (1978). Friction of rocks, *Pure Appl. Geophys.* **116**, no. 4-5, 615–626, doi 10.1007/BF00876528.

Calo, M., C. Dorbath, and M. Frogneux (2014). Injection tests at the EGS reservoir of Soultz-sous-Forêts. Seismic response of the GPK4 stimulations, *Geothermics* doi 10.1016/j.geothermics.2013.10.007

Cesca, S., F. Grigoli, S. Heimann, A. González, E. Buforn, S. Maghsoudi, E. Blanch, and T. Dahm ((subm.)). The September-October 2013 seismic sequence offshore Spain: A case of seismicity triggered by gas injection?, *Geophys J Int*.

Cocco, M., and A. Rovelli (1989). Evidence for the variation of stress drop between normal and thrust faulting earthquakes in Italy, *J. Geophys. Res. Solid Earth* **94**, no. B7, 9399–9416, doi 10.1029/JB094iB07p09399.

Cornet, F. H., T. Bérard, and S. Bourouis (2007). How close to failure is a granite rock mass at a 5 km depth?, *Int. J. Rock Mech. Min. Sci.* **44**, no. 1, 47–66, doi 10.1016/j.ijrmms.2006.04.008.

Coueslan, M. L. (2007). Processing and interpretation of time-lapse vertical seismic profile data from the Penn West CO2 Monitoring Project, *M Sc Thesis Univ. Calg.*

Cuenot, N., J. Charléty, L. Dorbath, and H. Haessler (2006). Faulting mechanisms and stress regime at the European HDR site of Soultz-sous-Forêts, France, *Geothermics* **35**, no. 5–6, 561–575, doi 10.1016/j.geothermics.2006.11.007.

Das, I., and M. D. Zoback (2011). Long-period, long-duration seismic events during hydraulic fracture stimulation of a shale gas reservoir, *Lead. Edge* **30**, no. 7, 778–786, doi 10.1190/1.3609093.

DeCourten, F. (2008). Geology of Northern California, [online] Available from: http://www.cengage.com/custom/regional_geology.bak/data/DeCourten_0495763829_LowRes_New.pdf

Deichmann, N., and D. Giardini (2009). Earthquakes Induced by the Stimulation of an Enhanced Geothermal System below Basel (Switzerland), *Seismol. Res. Lett.* **80**, no. 5, 784–798, doi 10.1785/gssrl.80.5.784.

DiPippo, R. (2008). Geothermal power plants principles, applications, case studies and environmental impact, [online] Available from: http://www.engineeringvillage.com/controller/servlet/OpenURL?genre=book&isbn=9780750686204

Dost, B., and H. K. Haak (2007). Natural and induced seismicity, *Geol. Neth. Ed. ThE Wong DAJ Batjes J Jager R. Neth. Acad. Arts Sci.* 223–239.

Eaton, D. W., M. van der Baan, J. B. Tary, B. Birkelo, and S. Cutten (2013). Low- frequency tremor signals from a Hydraulic Fracture Treatment in Northeast British Columbia, Canada, in *Proceedings of 4th EAGE Passive Seismic Workshop*, Amsterdam, The Netherlands.

Eberhart-Phillips, D., and D. H. Oppenheimer (1984). Induced seismicity in The Geysers Geothermal Area, California, *J. Geophys. Res. Solid Earth* **89**, no. B2, 1191–1207, doi 10.1029/JB089iB02p01191.

Edwards, B., and J. Douglas (2013). Magnitude scaling of induced earthquakes, *Geothermics* doi 10.1016/j.geothermics.2013.09.012

Efron, B., and R. Tibshirani (1986). Bootstrap Methods for Standard Errors, Confidence Intervals, and Other Measures of Statistical Accuracy, *Stat. Sci.* **1**, no. 1, 54–75, doi 10.1214/ss/1177013815.

Ellsworth, W. L. (2013). Injection-Induced Earthquakes, *Science* **341**, no. 6142, 1225942, doi 10.1126/science.1225942.

Eshelby, J. D. (1957). The Determination of the Elastic Field of an Ellipsoidal Inclusion, and Related Problems, *Proc. R. Soc. Lond. Ser. Math. Phys. Sci.* **241**, no. 1226, 376–396, doi 10.1098/rspa.1957.0133.

Evans, K. F., A. Zappone, T. Kraft, N. Deichmann, and F. Moia (2012). A survey of the induced seismic responses to fluid injection in geothermal and CO2 reservoirs in Europe, *Geothermics* **41**, 30–54, doi 10.1016/j.geothermics.2011.08.002.

Feng, Q., and J. M. Lees (1998). Microseismicity, stress, and fracture in the Coso geothermal field, California, *Tectonophysics* **289**, no. 1–3, 221–238, doi 10.1016/S0040-1951(97)00317-X.

Foulger, G. R., C. C. Grant, A. Ross, and B. R. Julian (1997). Industrially induced changes in Earth structure at the Geysers Geothermal Area, California, *Geophys. Res. Lett.* **24**, no. 2, 135–137, doi 10.1029/96GL03152.

Frohlich, C. (1991). Display and quantitative assesment of distributions of earthquake focal mechanisms, *Geophys J Int* **144**, 300–308.

García, J., M. Walters, J. Beall, C. Hartline, A. Pingol, S. Pistone, and M. Wright (2012). Overview of the north-western Geysers EGS demonstration project, *Proc. Thirty-Seventh Workshop Geotherm. Reserv. Eng. Stanf. Univ. Stanf. Calif. SGP-TR-194*.

Gaucher, E., and T. Kohl (2014). Are the seismogenic responses of the Soultz and the Groß Schönebeck enhanced geothermal fields understood? *74th annual meeting of the German Geophysical Society (DGG)*, Karlsruhe, 2014.

Gephart, J. W. (1990). Stress and the direction of slip on fault planes, *Tectonics* **9**, no. 4, 845–858, doi 10.1029/TC009i004p00845.

Gephart, J. W., and D. W. Forsyth (1984). An improved method for determining the regional stress tensor using earthquake focal mechanism data: Application to the San Fernando Earthquake Sequence, *J. Geophys. Res. Solid Earth* **89**, no. B11, 9305–9320, doi 10.1029/JB089iB11p09305.

Ghassemi, A. (2012). A Review of Some Rock Mechanics Issues in Geothermal Reservoir Development, *Geotech. Geol. Eng.* **30**, no. 3, 647–664, doi 10.1007/s10706-012-9508-3.

Goertz-Allmann, B., V. Oye, K. Iranpour, D. Küen, E. Aker, and B. Bohloli (2013). Microseismic monitoring of a CO2 Injection: the case study at In Salah, Algeria, in *Proceedings of 4th EAGE Passive Seismic Workshop, Amsterdam, The Netherlands*.

Goertz-Allmann, B. P., A. Goertz, and S. Wiemer (2011). Stress drop variations of induced earthquakes at the Basel geothermal site, *Geophys Res Lett* **38**, no. 9, L09308, doi 10.1029/2011GL047498.

Görgün, E., M. Bohnhoff, F. Bulut, and G. Dresen (2010). Seismotectonic setting of the Karadere–Düzce branch of the North Anatolian Fault Zone between the 1999 Izmit and Düzce ruptures from analysis of Izmit aftershock focal mechanisms, *Tectonophysics* **482**, no. 1–4, 170–181, doi 10.1016/j.tecto.2009.07.012.

Gritto, R., and S. P. Jarpe (2014). Temporal variations of Vp/Vs-ratio at The Geysers geothermal field, USA, *Geothermics* 1–8, doi 10.1016/j.geothermics.2014.01.012.

Grob, M., and M. van der Baan (2011). Inferring in-situ stress changes by statistical analysis of microseismic event characteristics, *Lead. Edge* **30**, no. 11, 1296–1301, doi 10.1190/1.3663403.

Guilhem, A., L. Hutchings, D. S. Dreger, and L. R. Johnson (2014). Moment tensor inversions of $M \sim 3$ earthquakes in the Geysers geothermal fields, California, *J. Geophys. Res. Solid Earth* 2013JB010271, doi 10.1002/2013JB010271.

Gunasekera, R. C., G. R. Foulger, and B. R. Julian (2003). Reservoir depletion at The Geysers geothermal area, California, shown by four-dimensional seismic tomography, *J. Geophys. Res. Solid Earth* **108**, no. B3, n/a–n/a, doi 10.1029/2001JB000638.

Gunther, B. (2008). Pembina Cardium Summary Report, *(Internal Report)*

Hanks, T. C., and H. Kanamori (1979). A moment magnitude scale, *J Geophys Res* **84**, 2348–2350.

Hardebeck, J. L. (2012). Coseismic and postseismic stress rotations due to great subduction zone earthquakes, *Geophys. Res. Lett.* **39**, no. 21, n/a–n/a, doi 10.1029/2012GL053438.

Hardebeck, J. L., and E. Hauksson (1999). Role of Fluids in Faulting Inferred from Stress Field Signatures, *Science* **285**, no. 5425, 236–239, doi 10.1126/science.285.5425.236.

Hardebeck, J. L., and E. Hauksson (2001). Stress Orientations Obtained from Earthquake Focal Mechanisms: What Are Appropriate Uncertainty Estimates?, *Bull. Seismol. Soc. Am.* **91**, no. 2, 250–262, doi 10.1785/0120000032.

Hardebeck, J. L., and A. J. Michael (2004). Stress orientations at intermediate angles to the San Andreas Fault, California, *J. Geophys. Res. Solid Earth* **109**, no. B11303, doi 10.1029/2004JB003239. [online] Available from: http://onlinelibrary.wiley.com/doi/10.1029/2004JB003239/abstract (Accessed 13 June 2013)

Hardebeck, J. L., and A. J. Michael (2006). Damped regional-scale stress inversions: Methodology and examples for southern California and the Coalinga aftershock sequence, *J. Geophys. Res. Solid Earth* **111**, no. B11, B11310, doi 10.1029/2005JB004144.

Hardebeck, J. L., and P. M. Shearer (2002). A New Method for Determining First-Motion Focal Mechanisms, *Bull. Seismol. Soc. Am.* **92**, no. 6, 2264–2276, doi 10.1785/0120010200.

Hasegawa (2011). Nearly complete stress drop in the 2011 M_w 9.0 off the Pacific coast of Tohoku Earthquake, *Earth Planets Space* **63**, no. 7, 703–707, doi 10.5047/eps.2011.06.007.

Heidbach, O., M. Tingay, and F. Wenzel (2010). Frontiers in Stress Research, *Tectonophysics* **482**, no. 1–4, 1–2, doi 10.1016/j.tecto.2009.11.009.

Hitchon, B. (2009). *Pembina Cardium CO2 Monitoring Pilot. A CO2-EOR Project, Alberta, Canada*, Geoscience Publishing, Alberta, Canada.

Holub, K., P. Konečný Jr., and J. Knejzlík (2009). Investigation of the mechanical and physical properties of greywacke specimens, *Int. J. Rock Mech. Min. Sci.* **46**, no. 1, 188–193, doi 10.1016/j.ijrmms.2008.02.011.

Hulen, J. B., J. C. Quick, and J. N. Moore (1997a). Converging evidence for fluid overpressures at peak temperatures in the pre-vapor dominated Geysers Hydrothermal system, in *Geothermal Reseources Council Transactions*, vol. 21, pp. 623–628.

Hulen, J. B., M. T. Heizler, J. A. Stimac, J. N. Moore, and J. C. Quick (1997b). New constraints on the timing and magmatism, volcanism and the onset of the vapor dominated conditions at The Geysers steam field, California, pp. 75– 82, Stanford University, Stanford, USA.

Hummel, N., and S. A. Shapiro (2012). Microseismic estimates of hydraulic diffusivity in case of non-linear fluid-rock interaction, *Geophys. J. Int.* **188**, no. 3, 1441–1453, doi 10.1111/j.1365-246X.2011.05346.x.

Ickrath, M., M. Bohnhoff, F. Bulut, and G. Dresen (2014). Stress rotation and recovery in conjunction with the 1999 Izmit M_W 7.4 earthquake, *Geophys. J. Int.* **196**, no. 2, 951–956, doi 10.1093/gji/ggt409.

IPCC (2007). Intergovernmental Panel on Climate Change (IPCC), in *Mitigation of Climate Change*. [online] Available from: http:www.ipcc.ch/ipccreports/ar4-wg3.htm

Jaeger, J., and N. G. Cook (1971). *Fundamentals of Rock Mechanics*.

Jeanne, P., J. Rutqvist, D. Vasco, J. Garcia, P. F. Dobson, M. Walters, C. Hartline, and A. Borgia (2014). A 3D hydrogeological and geomechanical model of an Enhanced Geothermal System at The Geysers, California, *Geothermics* **51**, 240–252, doi 10.1016/j.geothermics.2014.01.013.

Kaiser, J. (1953). Kenntnisse und Folgerungen aus der Messung von Geräuschen bei Zugbeanspruchung von metallischen Werkstoffen, *Arch. Für Isenhütten-Wesen* **24**, 43–45.

Kato, A. et al. (2011). Anomalous depth dependency of the stress field in the 2007 Noto Hanto, Japan, earthquake: Potential involvement of a deep fluid reservoir, *Geophys. Res. Lett.* **38**, no. 6, L06306, doi 10.1029/2010GL046413.

Klein, F. (2002). User's guide to HYPOINVERSE-2000, a Fortran Program to Solve for Earthquake Locations and Magnitudes, *Open File Rep.* [online] Available from: NCEDC, http://www.ncedc.org/ftp/pub/doc/ ncsn/shadow2000.pdf

Klein, F. W. (2006). Y2000 shadow format and NCSN data codes, [online] Available from: NCEDC, http://www.ncedc.org/ftp/pub/doc/ncsn/shadow2000.pdf

Krause, F. F., H. N. Collins, D. A. Nelson, S. D. Machemer, and P. R. French (1987). Multiscale Anatomy of a Reservoir: Geological Characterization of Pembina-Cardium Pool, West-Central Alberta, Canada, *Am. Assoc. Pet. Geol.* **71**, no. 10, 1233–1260.

Krause, F. F., K. B. Deutsch, S. D. Joiner, J. E. Barclay, R. L. Hall, and L. V. Hills (1994). Cretaceous Cardium Formation of the Western Canada Sedimentary Basin., *GD Mossop Shetsen Compil. Geol. Atlas West. Can. Sediment. Basin 375-385 Can. Soc. Pet. Geol. Alta. Res. Counc.*

Kwiatek, G., M. Bohnhoff, G. Dresen, A. Schulze, T. Schulte, G. Zimmermann, and E. Huenges (2010). Microseismicity Induced During Fluid-Injection: A Case Study from the Geothermal Site at Gross Schoenebeck, North German Basin, *Acta Geophys* **58**, no. 6, 995–1020, doi 10.2478/s11600-010-0032-7.

Kwiatek, G., K. Plenkers, and G. Dresen (2011). Source Parameters of Picoseismicity Recorded at Mponeng Deep Gold Mine, South Africa: Implications for Scaling Relations, *Bull Seism. Soc Am* **101**, no. 6, 2592–2608, doi 10.1785/0120110094.

Kwiatek, G., M. Bohnhoff, P. Martínez-Garzón, F. Bulut, and G. Dresen (2013). High resolution reservoir characterization using induced seismicity and state of the art waveform processing techniques, *First Break* **31**, no. 7, 81–88.

Kwiatek, G., F. Bulut, M. Bohnhoff, and G. Dresen (2014a). High-resolution analysis of seismicity induced at Berlín geothermal field, El Salvador, *Geothermics* doi 10.1016/j.geothermics.2013.09.008. [online] Available from: http://www.sciencedirect.com/science/article/pii/S0375650513000825 (Accessed 29 January 2014)

Kwiatek, G., T. W. Goebel, and G. Dresen (submitted). Seismic moment tensor and b-value variations over succesive seismic cycles in laboratory stick-slip experiments, *Geophys Res Lett*.

Lavrov, A. (2003). The Kaiser effect in rocks: principles and stress estimation techniques, *Int. J. Rock Mech. Min. Sci.* **40**, no. 2, 151–171, doi 10.1016/S1365-1609(02)00138-7.

Lei, X., S. Ma, W. Chen, C. Pang, J. Zeng, and B. Jiang (2013). A detailed view of the injection-induced seismicity in a natural gas reservoir in Zigong, southwestern Sichuan Basin, China, *J. Geophys. Res. Solid Earth* **118**, no. 8, 4296–4311, doi 10.1002/jgrb.50310.

Day-Lewis, A. D. F. (2008). Characterization and modeling of in-situ stress heterogeneity, PhD Dissertation, Stanford University, Menlo Park.

Lorenz, J. C., L. W. Teufel, and N. R. Warpinski (1991). Regional Fractures I: A Mechanism for the Formation of Regional Fractures at Depth in Flat-Lying Reservoirs (1), *AAPG Bull.* **75**, no. 11, 1714–1737.

Lund, B., and J. Townend (2007). Calculating horizontal stress orientations with full or partial knowledge of the tectonic stress tensor, *Geophys. J. Int.* **170**, no. 3, 1328–1335, doi 10.1111/j.1365-246X.2007.03468.x.

Madariaga, R. (1976). Dynamics of an expanding circular fault, *Bull Seism. Soc Am* **66**, 639–666.

Majer, E. L., and J. E. Peterson (2007). The impact of injection on seismicity at The Geysers, California Geothermal Field, *Int. J. Rock Mech. Min. Sci.* **44**, no. 8, 1079–1090, doi 10.1016/j.ijrmms.2007.07.023.

Majer, E. L., R. Baria, M. Stark, S. Oates, J. Bommer, B. Smith, and H. Asanuma (2007). Induced seismicity associated with Enhanced Geothermal Systems, *Geothermics* **36**, no. 3, 185–222, doi 10.1016/j.geothermics.2007.03.003.

Majer, E. L., J. Nelson, A. Robertson-Tait, J. Savy, and A. Wong (2012). Protocol for addressing induced seismicity associated with Enhanced Geothermal Systems, *US Dep. Energy*.

Martens, S., T. Kempka, A. Liebscher, S. Lüth, F. Möller, A. Myrttinen, B. Norden, C. Schmidt-Hattenberger, M. Zimmer, and M. Kühn (2012). Europe's longest-operating on-shore CO2 storage site at Ketzin, Germany: a progress report after three years of injection, *Environ. Earth Sci.* **67**, no. 2, 323–334, doi 10.1007/s12665-012-1672-5.

Martínez-Garzón, P., G. Kwiatek, M. Ickrath, and P. Bohnhoff (in press). MSATSI: A MATLAB© package for stress inversion combining solid classic methodology, a new simplified user-handling and a visualization tool, *Seism. Res Lett*.

Martínez-Garzón, P., M. Bohnhoff, G. Kwiatek, and G. Dresen (2013). Stress tensor changes related to fluid injection at The Geysers geothermal field, California, *Geophys. Res. Lett.* **40**, 2596–2691, doi 10.1002/grl.50438.

McGarr, A. (2014). Maximum magnitude earthquakes induced by fluid injection, *J. Geophys. Res. Solid Earth* n/a–n/a, doi 10.1002/2013JB010597.

McGarr, A., and J. B. Fletcher (2002). Mapping Apparent Stress and Energy Radiation over Fault Zones of Major Earthquakes, *Bull. Seismol. Soc. Am.* **92**, no. 5, 1633–1646, doi 10.1785/0120010129.

McKenzie, D. P. (1969). The relation between fault plane solutions for earthquakes and the directions of the principal stresses, *Bull. Seismol. Soc. Am.* **59**, no. 2, 591–601.

Menke, W. (1989). *Geophysical Data Analysis: Discrete Inverse Theory*, Academic Press, San Diego, USA.

Michael, A. J. (1984). Determination of stress from slip data: Faults and folds, *J. Geophys. Res. Solid Earth* **89**, no. B13, 11517–11526, doi 10.1029/JB089iB13p11517.

Michael, A. J. (1987). Use of focal mechanisms to determine stress: A control study, *J. Geophys. Res. Solid Earth* **92**, no. B1, 357–368, doi 10.1029/JB092iB01p00357.

Moeck, I., G. Kwiatek, and G. Zimmermann (2009). Slip tendency analysis, fault reactivation potential and induced seismicity in a deep geothermal reservoir, *J Struct Geol* **31**, no. 10, 1174–1182, doi 10.1016/j.jsg.2009.06.012.

Moore, J. N., M. C. Adams, and A. J. Anderson (2000). The fluid inclusion and mineralogical record of the transition from liquid to vapor-dominated conditions in The Geysers geothermal system, *Econ Geol* **95**.

Moreno, M., C. Haberland, O. Oncken, A. Rietbrock, S. Angiboust, and O. Heidbach (2014). Locking of the Chile subduction zone controlled by fluid pressure before the 2010 earthquake, *Nat. Geosci.* **7**, no. 4, 292–296, doi 10.1038/ngeo2102.

Mossop, A., and P. Segall (1997). Subsidence at The Geysers Geothermal Field, N. California from a comparison of GPS and leveling surveys, *Geophys Res Lett* **24**, no. 14, 1839–1842, doi 10.1029/97GL51792.

Nur, A., and J. D. Byerlee (1971). An exact effective stress law for elastic deformation of rock with fluids, *J. Geophys. Res.* **76**, no. 26, 6414–6419, doi 10.1029/JB076i026p06414.

Oppenheimer, D. H. (1986). Extensional tectonics at The Geysers Geothermal Area, California, *J. Geophys. Res. Solid Earth* **91**, no. B11, 11463–11476, doi 10.1029/JB091iB11p11463.

Örgülü, G. (2011). Seismicity and source parameters for small-scale earthquakes along the splays of the North Anatolian Fault (NAF) in the Marmara Sea, *Geophys. J. Int.* **184**, no. 1, 385–404, doi 10.1111/j.1365-246X.2010.04844.x.

Oye, V. (2012). Monitoring of the Salah CO2 storage site (Krechba) using microseismic data analysis, *3rd EAGE CO2 Geol. Storage Workshop Expand. Abstr. Eur. Assoc. Geosci. Eng. Houten Neth.*

Parotidis, M., S. A. Shapiro, and E. Rothert (2004). Back front of seismicity induced after termination of borehole fluid injection, *Geophys. Res. Lett.* **31**, no. 2, doi 10.1029/2003GL018987.

Percival, D. B., and A. T. Walden (1993). *Spectral Analysis for Physical Applications: Multitaper and Conventional Univariate Techniques*, Cambridge University Press.

Plenefisch, T., and K.-P. Bonjer (1997). The stress field in the Rhine Graben area inferred from earthquake focal mechanisms and estimation of frictional parameters, *Tectonophysics* **275**, no. 1–3, 71–97, doi 10.1016/S0040-1951(97)00016-4.

Provost, A.-S., and H. Houston (2003). Stress orientations in northern and central California: Evidence for the evolution of frictional strength along the San Andreas plate boundary system, *J. Geophys. Res. Solid Earth* **108**, no. 2175, B3, doi 10.1029/2001JB001123.

Reasemberg, P., and D. Oppenheimer (1985). FPFIT,FPPLOT and FPPAGE: Fortran computer programs for calculating and displaying earthquake fault-plane solutions, *U.S. Geol. Surv. Open-file Rep.* 85–739.

Rivas, J. A. (2000). Seismic monitoring and its application as an exploration tool in Berlín geothermal field, El Salvador, *UNU Fellow Rep.* **17**, 355–384.

Rivera, L., and A. Cisternas (1990). Stress tensor and fault plane solutions for a population of earthquakes, *Bull. Seismol. Soc. Am.* **80**, no. 3, 600–614.

Ross, A., G. R. Foulger, and B. R. Julian (1999). Source processes of industrially-induced earthquakes at The Geysers geothermal area, California, *GEOPHYSICS* **64**, no. 6, 1877–1889, doi 10.1190/1.1444694.

Rothert, E., and S. A. Shapiro (2007). Statistics of fracture strength and fluid-induced microseismicity, *J. Geophys. Res. Solid Earth* **112**, no. B4, B04309, doi 10.1029/2005JB003959.

Ruthledge, J. T., W. S. Phillips, A. Roff, A. N. Albright, T. Hamilton-Smith, S. Jones, and K. Kimmich (1994). Subsurface fracture mapping using microearthquakes detected during primary oil production, in *Soc. Of Pet. Eng.*, p. paper SPE 28384, Clinton County, Kentucky.

Rutqvist, J., P. F. Dobson, J. Garcia, C. Hartline, P. Jeanne, C. M. Oldenburg, D. W. Vasco, and M. Walters (2013). The Northwest Geysers EGS Demonstration Project, California: Pre-stimulation Modeling and Interpretation of the Stimulation, *Math. Geosci.* 1–27, doi 10.1007/s11004-013-9493-y.

Santos, P. A., and J. A. Rivas (1999). Geophysical methods applied in the detection of faults in the Berlín geothermal field, in *Presented at the Geophysical Seminar, IPGH-CIG (MOP), El Salvador*.

Sasaki, S., and H. Kaieda (2002). Determination of Stress State from Focal Mechanisms of Microseismic Events Induced During Hydraulic Injection at the Hijiori Hot Dry Rock Site, *Pure Appl. Geophys.* **159**, no. 1-3, 489–516, doi 10.1007/PL00001262.

Schoenball, M., T. M. Müller, B. I. R. Müller, and O. Heidbach (2010). Fluid-induced microseismicity in pre-stressed rock masses, *Geophys. J. Int.* **180**, no. 2, 813–819, doi 10.1111/j.1365-246X.2009.04443.x.

Schoenball, M., C. Baujard, T. Kohl, and L. Dorbath (2012). The role of triggering by static stress transfer during geothermal reservoir stimulation, *J. Geophys. Res. Solid Earth* **117**, no. B9, n/a–n/a, doi 10.1029/2012JB009304.

Schorlemmer, D., S. Wiemer, and M. Wyss (2005). Variations in earthquake-size distribution across different stress regimes, *Nature* **437**, no. 7058, 539–542, doi 10.1038/nature04094.

Schrag, D. P. (2007). Preparing to Capture Carbon, *Science* **315**, no. 5813, 812–813, doi 10.1126/science.1137632.

Segall, P., and S. D. Fitzgerald (1998). A note on induced stress changes in hydrocarbon and geothermal reservoirs, *Tectonophysics* **289**, no. 1–3, 117–128, doi 10.1016/S0040-1951(97)00311-9.

Segall, P., J.-R. Grasso, and A. Mossop (1994). Poroelastic stressing and induced seismicity near the Lacq gas field, southwestern France, *J. Geophys. Res. Solid Earth* **99**, no. B8, 15423–15438, doi 10.1029/94JB00989.

Shapiro, S. A. (2008). *Microseismicity: A Tool for Reservoir Characterization*, EAGE Publications.

Shapiro, S. A., P. Audigane, and J.-J. Royer (1999). Large-scale in situ permeability tensor of rocks from induced microseismicity, *Geophys. J. Int.* **137**, no. 1, 207–213, doi 10.1046/j.1365-246x.1999.00781.x.

Shapiro, S. A., E. Rothert, V. Rath, and J. Rindschwentner (2002). Characterization of fluid transport properties of reservoirs using induced microseismicity, *Geophysics* **67**, no. 1, 212–220, doi 10.1190/1.1451597.

Shapiro, S. A., R. Patzig, E. Rothert, and J. Rindschwentner (2003). Triggering of Seismicity by Pore-pressure Perturbations: Permeability-related Signatures of the Phenomenon, *Pure Appl. Geophys.* **160**, no. 5-6, 1051–1066, doi 10.1007/PL00012560.

Shapiro, S. A., C. Dinske, and J. Kummerow (2007). Probability of a given-magnitude earthquake induced by a fluid injection, *Geophys. Res. Lett.* **34**, no. 22, doi 10.1029/2007GL031615.

Shapiro, S. A., O. S. Krüger, C. Dinske, and C. Langenbruch (2011). Magnitudes of induced earthquakes and geometric scales of fluid-stimulated rock volumes, *GEOPHYSICS* **76**, no. 6, WC55–WC63, doi 10.1190/geo2010-0349.1.

Sharma, N., V. Convertito, N. Maercklin, and A. Zollo (2013). Ground-Motion Prediction Equations for The Geysers Geothermal Area based on Induced Seismicity Records, *Bull. Seismol. Soc. Am.* **103**, no. 1, 117–130, doi 10.1785/0120120138.

Soltanzadeh, H., and C. D. Hawkes (2008). Semi-analytical models for stress change and fault reactivation induced by reservoir production and injection, *J. Pet. Sci. Eng.* **60**, no. 2, 71–85, doi 10.1016/j.petrol.2007.05.006.

Stephens, G., and B. Voight (1982). Hydraulic fracturing theory for conditions of thermal stress, *Int. J. Rock Mech. Min. Sci. Geomech. Abstr.* **19**, no. 6, 279–284, doi 10.1016/0148-9062(82)91364-X.

Stierle, E., V. Vavryčuk, J. Šílený, and M. Bohnhoff (2014). Resolution of non-double-couple components in the seismic moment tensor using regional networks—I: a synthetic case study, *Geophys. J. Int.* **196**, no. 3, 1869–1877, doi 10.1093/gji/ggt502.

Terakawa, T., A. Zoporowski, B. Galvan, and S. A. Miller (2010). High-pressure fluid at hypocentral depths in the L'Aquila region inferred from earthquake focal mechanisms, *Geology* **38**, no. 11, 995–998, doi 10.1130/G31457.1.

Terakawa, T., S. A. Miller, and N. Deichmann (2012). High fluid pressure and triggered earthquakes in the enhanced geothermal system in Basel, Switzerland, *J. Geophys. Res.* **117**, no. B7, doi 10.1029/2011JB008980

Terzaghi, K. (1923). *Soil Mechanics in Engineering Practice*, John Wiley & Sons.

Teufel, L. W., and D. W. Rhett (1991). Geomechanical Evidence for Shear Failure of Chalk During Production of the Ekofisk Field, Society of Petroleum Engineers. [online] Available from: https://www.onepetro.org/conference-paper/SPE-22755-MS (Accessed 18 April 2014)

Townend, J., and M. Zoback (2001). Implications of earthquake focal mechanisms for the frictional strength of the San Andreas fault system, *Geol. Soc. Lond. Spec. Publ.* **186**, 13–21, doi 10.1144/GSL.SP.2001.186.01.02.

Townend, J., and M. D. Zoback (2004). Regional tectonic stress near the San Andreas fault in central and southern California, *Geophys. Res. Lett.* **31**, no. L15S11, doi 10.1029/2003GL018918.

Tuncay, E., and R. Ulusay (2008). Relation between Kaiser effect levels and pre-stresses applied in the laboratory, *Int. J. Rock Mech. Min. Sci.* **45**, no. 4, 524–537, doi 10.1016/j.ijrmms.2007.07.013.

Vasco, D. W., J. Rutqvist, A. Ferretti, A. Rucci, F. Bellotti, P. Dobson, C. Oldenburg, J. Garcia, M. Walters, and C. Hartline (2013). Monitoring deformation at the Geysers Geothermal Field, California using C-band and X-band interferometric synthetic aperture radar, *Geophys. Res. Lett.* **40**, no. 11, 2567–2572, doi 10.1002/grl.50314.

Verdon, J. P., J.-M. Kendall, D. J. White, D. A. Angus, Q. J. Fisher, and T. Urbancic (2010). Passive seismic monitoring of carbon dioxide storage at Weyburn, *Lead. Edge* **29**, no. 2, 200–206, doi 10.1190/1.3304825.

Verdon, J. P., J.-M. Kendall, A. L. Stork, R. A. Chadwick, D. J. White, and R. C. Bissell (2013). Comparison of geomechanical deformation induced by megatonne-scale CO2 storage at Sleipner, Weyburn, and In Salah, *Proc. Natl. Acad. Sci.* doi 10.1073/pnas.1302156110.

Waldhauser, F., and W. L. Ellsworth (2000). A Double-Difference Earthquake Location Algorithm: Method and Application to the Northern Hayward Fault, California, *Bull. Seismol. Soc. Am.* **90**, no. 6, 1353–1368, doi 10.1785/0120000006.

Wallace, R. E. (1951). Geometry of Shearing Stress and Relation to Faulting, *J. Geol.* **59**, no. 2, 118–130.

Wang, H. T., X. F. Xian, G. Z. Yin, and J. Xu (2000). A new method of determining geostresses by the acoustic emission Kaiser effect, *Int. J. Rock Mech. Min. Sci.* **37**, no. 3, 543–547, doi 10.1016/S1365-1609(99)00081-7.

Wiemer, S., and M. Wyss (2000). Minimum magnitude of completeness in earthquake catalogs: Examples from Alaska, the Western United States & Japan, *Bull Seism. Soc Am* **90**, 859–869.

Williamson, K. H. (1990). Reservoir stimulation at The Geysers geothermal field, *Proc. Fifteenth Workshop Geotherm. Reserv. Eng. Stanf. Univ. Stanf. Calif.*

Xu, P. (2004). Determination of regional stress tensors from fault-slip data, *Geophys. J. Int.* **157**, no. 3, 1316–1330, doi 10.1111/j.1365-246X.2004.02271.x.

Yoshida, K., A. Hasegawa, T. Okada, T. Iinuma, Y. Ito, and Y. Asano (2012). Stress before and after the 2011 great Tohoku-oki earthquake and induced earthquakes in inland areas of eastern Japan, *Geophys. Res. Lett.* **39**, no. L03302, doi 10.1029/2011GL049729.

Zambrano- Narvaez, G., and R. J. Chalaturnyk (2007). Design and Deployment of an Integrated Instrumentation System in a Monitoring Well at the Penn West CO2-EOR Pilot, Alberta, Canada", Boston, MA.

Zambrano-Narvaez, G., and R. Chalaturnyk (2011). Case study of the cementing phase of an observation well at the Pembina Cardium CO2 monitoring pilot, Alberta, Canada, *Int. J. Greenh. Gas Control* **5**, no. 4, 841–849, doi 10.1016/j.ijggc.2010.12.003.

Zimmer, M., P. Pilz, and J. Erzinger (2011). Long-term surface carbon dioxide flux monitoring at the Ketzin carbon dioxide storage test site, *Environ. Geosci.* **18**, no. 2, 119–130, doi 10.1306/eg.11181010017.

Zoback, M. D. (2007). *Reservoir geomechanics*, Cambridge University Press, Cambridge.

Zoback, M. D., and S. M. Gorelick (2012). Earthquake triggering and large-scale geologic storage of carbon dioxide, *Proc. Natl. Acad. Sci.* 201202473, doi 10.1073/pnas.1202473109.

Zoback, M. L. (1992). First- and second-order patterns of stress in the lithosphere: The World Stress Map Project, *J. Geophys. Res. Solid Earth* **97**, no. B8, 11703–11728, doi 10.1029/92JB00132.

List of Publications

Monographs:

- **P. Martínez-Garzón** (2011). "Deformaciones dinámicas originadas por sismos en presas: Caso de la presa de Itoiz (Navarra)". MSc Thesis (in Spanish).

Published Papers:

- **Martínez-Garzón, P.**, M. Bohnhoff, G. Kwiatek, and G. Dresen (2013). Stress tensor changes related to fluid injection at The Geysers geothermal field, California, *Geophys. Res. Lett.* 40, 2596–2601, doi 10.1002/grl.50438.
- G. Kwiatek, M. Bohnhoff, **P. Martínez-Garzón**, F. Bulut and G. Dresen (2013). High resolution reservoir characterization using induced seismicity and state of the art waveform processing techniques. *First Break, volume 31, July 2013.*
- **Martínez-Garzón, P.**, M. Bohnhoff, G. Kwiatek, G. Zambrano-Narváez, R. Chalaturnyk (2013). Microseismic monitoring of CO_2 injection at the Penn West EOR Pilot, Canada: Implications for detection of wellbore leakage. *Sensors*.
- **Martínez-Garzón, P.**, G. Kwiatek, M. Ickrath, M. Bohnhoff (2014). MSATSI: A MATLAB package for stress inversion combining solid classic methodology, a new simplified user-handling and a visualization tool. *Seism. Res Lett*., 85,4, doi: 10.1785/0220130189. Software package available to download at www.gfz-potsdam.de/msatsi.

Submitted papers:

- Santoyo M.A., **P. Martínez-Garzón**, A. García-Jerez and F. Luzón. Surface Dynamic Deformation Estimates From Seismicity Near the Itoiz Reservoir, Northern Spain. (submitted to *Pure and Applied Geophysics*).

Papers in preparation:

- **Martínez-Garzón, P.**, G. Kwiatek, M. Bohnhoff. H. Sone, G. Dresen and C. Hartline. Spatiotemporal changes, faulting regimes and source parameters of induced seismicity: A case study from The Geysers geothermal field (in prep. for Journal of Geophysical Research).

Conference proceedings/ Extended abstracts:

- M. A. Santoyo, M. A., **P. Martínez-Garzón**, A. García-Jerez, F. Luzón; M. Herraiz (2011). "Dynamic deformations from seismicity near the Itoiz Reservoir, Northern Spain". *Extended abstract*, 4th IASPEI/IAEE International Symposium. esg4.eri.ucsb.edu/sites/esg4.eri.ucsb.edu/files/2.17%20Santoyo%20et%20al.pdf

- M. Bohnhoff, G. Kwiatek, **P. Martínez-Garzón** and G. Dresen (2013). "Microseismic Monitoring of Reservoir Stimulation: Case Studies and Implications for improved Geomechanical Characterization". EAGE Workshop, 2013.

•

List of figures

Chapter 1 – General introduction..... 1

1.1 Sketch illustrating different types of fluid-injection activities..... 2
1.2 Conceptual sketch of an EGS and a CO_2 storage site..... 6
1.3 Example of Double-Difference relocation of a seismicity cluster..... 10
1.4 Example of focal mechanisms calculated using first motion polarities..... 10
1.5 Examples of stress tensor inversion results using different software..... 11
1.6 Representation of the traction vectors acting in the different planes..... 12
1.7 Faulting regimes according to Anderson (1951)..... 13
1.8 Representation in the Mohr circle of the effect of the pore pressure increase.. 15
1.9 Schematic view of a reservoir subjected to long term production..... 17
1.10 Core sample photos from the analyzed case studies..... 23

Chapter 2 - Microseismic monitoring of CO_2 injection at the Penn West EOR Pilot: Implications for detection of wellbore leakage..... 24

1.1 Location of the monitoring, injector and producer wells..... 27
1.2 Seismograms and spectrograms recorded for different geophones..... 29
1.3 Average noise levels and seismic recordings at each sensor..... 32
1.4 Pressure measured by the sensors inside the observation well..... 33
1.5 Example of waveform analyzed using STA/LTA..... 34
1.6 Number of detections of each type detected by the STA/LTA..... 35
1.7 Examples of signals with high similarity to LPLD events..... 37

Chapter 3 - MSATSI: A MATLAB© package for stress inversion combining solid classic methodology, a new simplified user-handling and a visualization tool..... 40

Chapter 4 - Stress tensor changes related to fluid injection at The Geysers Geothermal Field, California..... 60

4.1 Spatial distribution of seismic events at The Geysers (M > 1)..... 63
4.2 Average stress field orientation for each depth interval..... 65
4.3 Stress field changes related to fluid injection..... 69

Chapter 5 - Spatiotemporal changes, faulting regimes and source-parameters of induced seismicity: A case study from The Geysers geothermal field..... 71

5.1 Map view of the seismicity at the NW The Geysers geothermal field 74
5.2 Map view of the relocated seismicity from the analyzed seismicity cluster..... 81
5.3 Map view of the focal mechanisms of the 100 strike-slip seismic events 82
5.4 Spatial distribution of the seismicity during different injection stages 83
5.5 Ternary diagrams (Frohlich, 1991) for each injection stage 84
5.6 Temporal evolution of flow rates and seismic observables (Part I)..... 85
5.7 Temporal evolution of flow rates and seismic observables (Part II) 86
5.8 Schematic diagram of thermal fracturing and pore pressure increase 90
5.9 Variation of the principal stresses on the Mohr circle 96

Chapter 6 – Summary of results and conclusions 97

6.1 Main heading of the MSATSI website..... 98
6.2 Surface distribution of the stress field orientations at reservoir depth (TG).... 100

Appendix A – High-resolution reservoir characterization using induced seismicity and state of the art waveform processing techniques 104

A.1 Schematic presentation of the three methods applied in the study 106
A.2 Spatial distribution of seismicity at Berlín Geothermal Field..... 108
A.3 Spatial distribution of seismicity at The Geysers Geothermal Field..... 109
A.4 Relocated seismicity at Berlín Geothermal Field 110
A.5 Calculation of source parameters at BGF 110
A.6 Spatio-temporal seismicity features at BGF 112
A.7 Stress rotations found at The Geysers geothermal field..... 114

List of tables

Chapter 1 – General introduction.....1

1.1 Main seismological techniques applied within different chapters 8
1.2 Relative position of principal stresses for each faulting style.....13
1.3 Fluid-injection projects where the maximum observed magnitude event occurred during or after the shut-in of the well 21

Chapter 2 - Microseismic monitoring of CO_2 injection at the Penn West EOR Pilot: Implications for detection of wellbore leakage 24

2.1 Summary of geophone status 31

Chapter 3 - MSATSI: A MATLAB© package for stress inversion combining solid classic methodology, a new simplified user-handling and a visualization tool 40

Chapter 4 - Stress tensor changes related to fluid injection at The Geysers Geothermal Field, California.....60

Chapter 5 - Spatiotemporal changes, faulting regimes and source-parameters of induced seismicity: A case study from The Geysers geothermal field 71

5.1 Time intervals and n° of events in each stage of the analyzed cycles.....78
5.2 Number of strike-slip and thrust events during the different injection stages ...82
5.3 Average distance from the injection point for each stage and cycle.....83

Chapter 6 – Summary of results and conclusions 97

Appendix A – High-resolution reservoir characterization using induced seismicity and state of the art waveform processing techniques 104

Acknowledgments

This dissertation has been possible only because the help of many persons:

Thank you to my Supervisor Marco Bohnhoff for providing me continuous support and help, for being always open to new initiatives and willing to discuss, no matter how busy he would be and for giving me his confidence to develop myself in science. Thank you to my Jedi and Friend Grzegorz Kwiatek. Letters are small to express how grateful I am to you, and how happy I am to learn from you and work together. This is only the beginning of a long story! Thank you very much to Georg Dresen, his enthusiasm on certain topics is really contagious and it can be really inspiring and motivating. Thanks for providing such a great feedback and good ideas. Thank you to Hiroki Sone for being always willing to correct my geomechanical flaws and endless discussions on different issues, I feel always wiser after talking to you.

Thank you to my permanent-office mate, neighbor and super friend Digdem Acarel, for having such a good and smooth working time, as well as so much fun from time to time ;). Thanks for sharing with me these marvelous chocolate reservoirs. Thanks to Elma and the rest of my PhD colleagues Bita-Bubbles, Christopher (translator!), Eva, Michele and Tina for different good moments along these years. Thank you to Hagen to make me not be afraid of the nights at GFZ ☺.

Thanks to Connie Schmidt-Hattenberger and Arnd Heumann to keep up with the HAI project. Great thanks to the 'Kids': Florian and Magda. It was really fun to share our HAI experiences together (and the Rockies, and the moments in the Alberta Lab, the conferences, etc…). Thank you to Alma Ornes, Gonzalo Zambrano, Nathan Deisman and Rick Chalaturnyk for making my time at UofA profitable and very good fun. Thank you to Mirko van der Baan for allowing me to join his interesting seismological meetings during my time at UofA.

Thank you to Roland Gritto, David Oppenheimer and more recently, Craig Hartline for their assistance and explanations while working with The Geysers data: it really made the work much easier and much more interesting. Thanks to all the different persons I have met during the conferences and slowly we became colleagues to have good discussions - and even sometimes friends that you are really happy to see again somewhere in the world.

Thanks to Miguel Angel Santoyo for encouraging me to apply to GFZ, and to Michel Herraiz for countless visits to his office for discussions way beyond seismology and the magnetic field.

To the most important after all, The Family: Creo que tengo la mejor familia del mundo, os adoro: Mama, Papa, Bely, Cuqui, Julia, Gonzi, Lela, Kaki, Ito, Piz, Bea, Macu, Nene y Mateo, muchas gracias a todos. Para Niall por caminar siempre conmigo y ser mi espíritu aventurero. Para Mame y Pape, que me van a faltar siempre.